

## ABSTRACT

Title of Document: SELF-ORGANIZATION IN FULLERENE  
THIN FILMS ON METAL SURFACES

Qian Shao, Doctor of Philosophy, 2014

Directed By: Professor Janice E. Reutt-Robey  
Department of Chemistry and Biochemistry

Since the 1985 discovery of  $C_{60}$ , fullerenes have emerged as key nanoelectronic components and promising biomedical probes. Understanding how to direct-and switch-the packing arrangements of fullerenes and their chemical derivatives at interfaces is important for advanced applications. In this thesis work, we explore structural motifs that can be achieved in films of the fullerene derivatives, phenyl- $C_{61}$ -butyric-acid methyl ester ( $C_{60}$ -PCBM) and phenyl- $C_{71}$ -butyric-acid methyl ester ( $C_{70}$ -PCBM), and metal phthalocyanines (ZnPc and tetranitro-ZnPc(TN-ZnPc)), at neat and chemically-modified Au (111) and Ag (111) substrates. On low-index metals, we observe how molecular ordering in  $C_{60}$ -PCBM and  $C_{70}$ -PCBM monolayers is frustrated by anisotropic fullerene-fullerene interactions. Transition to crystalline (2D hexagonal) fullerene arrangements is highly activated and dependent on local density. Molecular electrostatics provides a useful tool to rationalize

observed packing arrangements in PCBM films and the barriers for nanocrystallization. Additionally, we describe how molecular electrostatics drive vertical phase separation in binary PCBM-ZnPc mixtures. Finally, we report a primary study of supramolecule deposition, structures and stabilization on Ag (111).

SELF-ORGANIZATION IN FULLERENE THIN FILMS ON METAL SURFACES

by

Qian Shao

Dissertation submitted to the Faculty of the Graduate School of the  
University of Maryland, College Park, in partial fulfillment  
of the requirements for the degree of  
Doctor of Philosophy

2014

Advisory Committee:

Professor Janice E. Reutt-Robey, Chair

Professor Theodore L. Einstein, Dean's Representative

Professor Christopher Jarzynski

Professor Sang Bok Lee

Professor Yu-Huang Wang

© Copyright by

Qian Shao

2014



## Acknowledgements

First and foremost, I would like to thank my advisor, Prof. Janice Reutt-Robey. Her instruction, encouragement and super support during my graduate study gave me great impetus to carry out my research. Her availability and willingness to discuss any problem, idea, and result are greatly appreciated. It is a great pleasure to be her student.

I would like to thank Dr. Levan Tskipuri for all the help in maintaining my instruments and for sharing his expertise on STM measurements. I am thankful to my friends and coworkers at the University of Maryland: Dr. Yinying Wei, Dr. Wei Jin, Dr. Veda Bharath, Dr. Yilin Wang, Mr. Wentao Song, Mr. Jonathan Larson, and Ms. Miriam Cezza.

I am grateful to my committee members, Prof. Theodore L. Einstein, Prof. Christopher Jarzynski, Prof. Sang Bok Lee and Prof. Yu-Huang Wang for their helps to make me finish my graduate study in University of Maryland.

Last, but not least, I want to thank my parents, Kongfa Shao and Yuling Chai for their understanding, support, and love through my life, my husband, Jianbao Tao, whose consideration, encouragement, and devotion accompany me all the time.

# Table of Contents

Acknowledgements.....	ii
Table of Contents.....	iii
List of Tables .....	vi
List of Figures.....	vii
Abbreviations.....	xiii
Chapter 1: Introduction.....	1
1.1 Motivation.....	1
1.2 Organic Semiconductor Materials .....	10
1.2.1 Our model system.....	10
1.2.2 Functionalized fullerenes.....	11
1.2.3 Crystal habits of fullerenes .....	12
1.3 Thesis Outline .....	14
Chapter 2: Introduction to Instruments and Experimental Procedures.....	16
2.1 Scanning Tunneling Microscope (STM) .....	16
2.1.1 Background of STM .....	16
2.1.2 Basic principles of tunneling .....	17
2.1.3 STM operations .....	23
2.2 Experimental Setup.....	24
2.2.1 Our UHV-STM system.....	24
2.2.2 Substrate Au (111) and Ag (111) preparation .....	26
2.2.3 Tip preparation for STM.....	28
2.2.4 Liquid aerosol molecular deposition .....	29

Chapter 3: Single Component Self-Assembly on Metal Surfaces .....	35
3.1 Solvent-Assisted Growth of Metal Phthalocyanine Thin Films on Au (111) .	35
3.1.1 Introduction.....	35
3.1.2 Experimental methods .....	36
3.1.3 Results and discussion .....	37
3.1.4 Summary.....	43
3.2 Molecular ordering in C <sub>60</sub> -PCBM thin films .....	44
3.2.1 Introduction.....	44
3.2.2 Methods .....	46
3.2.3 Results.....	47
3.2.4 Discussion.....	52
3.2.5 Summary.....	60
Chapter 4: Vertical Phase Separation in Bilayer C <sub>60</sub> -PCBM: ZnPc Films .....	62
4.1 Introduction.....	63
4.2 Methods .....	65
4.3 Results and Discussion .....	66
4.4 Summary.....	76
Chapter 5: 2D Hexagonal Motifs and Layered Stacking in C <sub>70</sub> -PCBM Films on Au	
(111).....	78
5.1 Introduction.....	78
5.2 Experimental Methods.....	82
5.3 Results and Discussion .....	83
5.4 Conclusion .....	92

Chapter 6: Supramolecules-CHCl <sub>3</sub> Assembly on Ag (111): Structure & Stability ..	94
6.1 Introduction.....	94
6.2 Experimental Methods.....	98
6.3 Results and Discussion .....	99
6.4 Conclusion .....	109
Chapter 7: Summary and Outlook.....	111
Appendix.....	117
Reference.....	123

## List of Tables

<b>Table 3.1</b> Solutions utilized for aerosol deposition.....	38
<b>Table 4.1</b> Energetic interactions in the PCBM, ZnPc, and Au (111) system.....	64
<b>Table 5.1</b> Favored fullerene monolayer structures on (111)-oriented coinage metal surfaces: structural parameters.....	82

## List of Figures

<b>Figure 1.1</b> Functional operation of an organic solar cell: (a) Schematic illustration of gradient heterojunction, which offers high interfacial areas for exciton unbinding and efficient charge transfer pathways to electrodes. (b) Processes of photocurrent production from incident light.....	3
<b>Figure 1.2</b> Schematic illustrations of typical atomistic processes occurring during atomic film growth.....	8
<b>Figure 1.3</b> Crystal habits of fullerene C <sub>60</sub> , C <sub>70</sub> and functionalized fullerenes C <sub>60</sub> -PCBM, C <sub>70</sub> -PCBM. 1. 3D fcc crystal structure of C <sub>60</sub> . 2. C <sub>60</sub> 2D hexagonal monolayer film prepared by physical vapor deposition and a model of 2D hexagonal structure ( <i>J Vac Sci Technol B</i> , <b>12</b> , 1942 (1994)). 3. 3D co-crystal structure of C <sub>60</sub> -PCBM with chlorobenzene ( <i>Chem Commun</i> , 2116-2118 (2003)). 4. Neat (solvent free) C <sub>60</sub> -PCBM crystallites, grown from solution on a solid support through evaporative control ( <i>Phys Chem Chem Phys</i> , <b>12</b> , 4473-80 (2010))......	13
<b>Figure 2.1</b> (a) One dimensional potential step with a barrier height of $V_0$ and corresponding wavefunction for a traveling electron impinging on the barrier with $E_k = V_0/2$ (b) in quantum mechanics.....	18
<b>Figure 2.2</b> (a) One-dimensional rectangular barrier potential of height $V_0$ and width $a$ and corresponding electron wavefunction for an incident electron with a kinetic energy $E_k = V_0/2$ (b).....	19
<b>Figure 2.3</b> Schematic of STM one-dimensional tunneling junction.....	20
<b>Figure 2.4</b> Illustration of an ideal STM tip (at top) which narrows down to an atomically sharp point. The tunneling current region is determined by proximate (exponential dependence on distance). The sample to be imaged is shown at the bottom.....	21
<b>Figure 2.5</b> Schematic of electronic band alignment for a sample-tip tunneling junction. The grey area represents electron filled states (occupied level) and the white area represents empty states, ready to accept electrons (unoccupied level). By application of a bias voltage $V_{\text{bias}}$ , $E_f$ of the sample is modified. Arrows showed direction of electron flow between tip and sample.....	22
<b>Figure 2.6</b> UHV-STM analysis system with fast entry loadlock used in this thesis research. ....	26
<b>Figure 2.7</b> Representative STM images of atomically clean Au (111), revealing the characteristic herringbone reconstruction, 35 × 35 nm (a). Ag (111), step bunch at the upper right indicates a step pinning site due to a local impurity (out of view) (b).....	28

**Figure 2.8** Schematic of tip end before and after corresponding polishing: (a) cut end; (b) tapered end; (c) atomically sharp end.....29

**Figure 2.9** Schematic of aerosol molecular-beam deposition source.....31

**Figure 2.10** The UV-VIS absorption spectrum of a PCBM film deposited on a SiO<sub>2</sub> substrate through 500 pulses of the aerosol free jet source (0.5 μmol/mL CHCl<sub>3</sub>). The characteristic PCBM absorption band at 330 nm is used to calculate source flux.....33

**Figure 3.1** Impact of aerosol solvent on patterning of MPc islands on Au (111) (0.4 ML coverage). UHV-STM images of as deposited films. Left: TN-ZnPc/Au(111) from (a) acetone and (b) dichlorobenzene; right: ZnPc/Au(111) from (c) acetone and (d) toluene (0.25 ML); (e) molecular models of TN-ZnPc and ZnPc.....39

**Figure 3.2** Monolayer TN-ZnPc films deposited on Au (111) from acetone microaerosols. UHV-STM images of films as deposited on room temperature substrates (a) and following a 10 min 200 °C anneal (b); (c,d) corresponding height distribution histograms of as deposited (c) and thermally annealed (d) films; (e) molecularly resolved domain of TN-ZnPc film.....41

**Figure 3.3** Monolayer ZnPc film deposited on Au (111) from chloroform microaerosols. (a) UHV-STM image of film deposited on room temperature substrate followed by a 10 min 180 °C anneal; (b) molecularly resolved image of ZnPc film; (c) corresponding height distribution histogram of thermally annealed film.....43

**Figure 3.4** UHV-STM images of submonolayer PCBM film deposited from microaerosol solvents on Au(111) at 27 °C: (a) 0.1 ML PCBM/chloroform; (b) 0.5 ML PCBM/chloroform; (c) 0.15 ML PCBM/dichlorobenzene; (d) 0.5 ML PCBM/dichlorobenzene.....48

**Figure 3.5** 0.1 ML PCBM films deposited on Au (111) from chloroform microaerosols. UHV-STM images of PCBM islands following (a) flash anneal to 180 °C and (b) 15 min 160 °C anneal. Line profile indicates residual solvent (0.2 nm height) inside such PCBM island (not shown in (a, b)) with 0.6 nm asperities; (c, d) 15 min anneal at 185 °C shown with two magnification.....49

**Figure 3.6** Submonolayer PCBM films deposited on Au (111) from chloroform microaerosols. UHV-STM images shown with two magnification: (a, b) 0.4 ML film after a 20 min 230 °C anneal; (c, d) 0.8 ML film after a 15 min 130 °C anneal. Arrows indicate doublerow structures.....52

**Figure 3.7** Density-dependent structures in PCBM monolayer films: (a, b) Lower density (0.86 molecules/nm<sup>2</sup>) PCBM monolayer after 10 min 200 °C anneal. Magnified image shows disordered structure. (c) Higher density (1 molecules/nm<sup>2</sup>) PCBM film shows coexisting phases. (d) Ordered 2D hexagonal structure domain with insert packing model. (e) Large scale PCBM monolayer with 2D hexagonal

domains. (f) fast Fourier transform pattern of 2D hexagonal structure of the same film domain yields the 0.98 nm unit cell.....54

**Figure 3.8** UHV-STM images of PCBM film deposited on Au(111) from chloroform microaerosols: (a) as-deposited on room temperature substrate, (b) followed by a 10 min 180 °C anneal, (c, d) double-row molecular structures observed in surface regions near the PCBM particle. Initial PCBM particulate height is greatly reduced.56

**Figure 3.9** “Processing phase diagram” depicts accessible PCBM structures from chloroform microaerosols as a function of surface coverage and anneal temperature.....56

**Figure 3.10** Energies of PCBM dimers in a “standing-up” orientation (left) and a “lying-down” orientation (right), computed by DFT as a function of intermolecular distance. Diamonds represent calculated values. Solid black line depicts an energy barrier for reorientation from a lying-down to a standing-up structure. Shaded region shows available thermal energy under experimental conditions.....58

**Figure 4.1** Binary PCBM + ZnPc film codeposited from equimolar microaerosol chloroform solvent onto Au (111): (a) UHV-STM image,  $120 \times 120 \text{ nm}^2$ . (b) Corresponding height histogram with an arrow denoting fwhm = 0.15 nm. The asymmetric histogram contains two modes, corresponding to the dark and light regions of the STM image. (c) Schematic illustration of as deposited film structure. Height variations are attributed to solvent-covered gold regions and to solute aggregates.....67

**Figure 4.2** STM images of binary films following stepwise annealing: (a) 80 °C anneal for 20 min. (b) 100 °C anneal for 20 min. (c) Height histogram of film a shows an increased spread in height distribution relative to unannealed films. (d) Height histogram of further annealed film b reveals three modes (See Appendix B for mode analysis).....68

**Figure 4.3** STM images of binary film after thermal anneal (270 °C, 20 min) revealing phase separation is shown: (a) bilayer film with first layer ZnPc (dark) and second layer PCBM (bright spherical protrusions), (b) first layer ZnPc image with molecular resolution, (c) large-scale STM image of binary film. PCBM molecules are brighter regions, and exposed ZnPc monolayer is darker regions.....70

**Figure 4.4** Sequentially deposited monolayer ZnPc on monolayer PCBM/Au (111) films from microaerosol chloroform solvent. STM images show (a) as-deposited film morphology and (b) film morphology after a 20 min, 260 °C anneal.....72

**Figure 4.5** Electrostatic energy computed for two different dimer stackings: (a) Molecular moments; red arrows depict dipoles. (b) PCBM/ZnPc/Au arrangement. (c) ZnPc/PCBM/Au arrangement. Yellow represents Au (the bright line is the Au (111)



mirror plane). Image dipoles are shown as gray arrows. PCBM/ZnPc/Au (111) stacking favored by 0.16 eV (= 3.7 kcal/mol) over ZnPc/PCBM/Au (111) stacking..74

**Figure 4.6** Impact of local PCBM density ( $\rho$ ) on PCBM displacement to second layer: (a)  $\rho_{\text{low}}$ , where PCBM is displaced to second layer. (b)  $\rho_{\text{high}}$ , PCBM nucleate to form 2D hexagonal island (inset) in contact with Au(111), which cannot be displaced to the second layer.....76

**Figure 5.1** (a) The  $(2\sqrt{3} \times 2\sqrt{3})$  R30° structure of C<sub>60</sub> on metal-(111) surface. (b) The  $(\sqrt{13} \times \sqrt{13})$  R ± 13.9° structure of C<sub>70</sub> on metal-(111) surface<sup>1</sup>. Nearest neighbor distance (NND) is shown on right with different molecular orientations....82

**Figure 5.2** Monolayer PCBM film directly deposited from microaerosol chloroform solvent onto room-temperature Au (111). (a) UHV-STM image, 150 nm × 150 nm. (b) Magnified region reveals aggregates islands and dim inter-island regions. (c) Line profile taken from the blue line in (b) shows the 0.20 nm apparent height of the PCBM aggregates relative to the dim regions.....84

**Figure 5.3** Images of monolayer (1 MLE) C<sub>70</sub>-PCBM film following 180°C annealing for 20 min, acquired by UHV-STM: (a) Film morphology illustrates variable PCBM density, with coexistence of small clusters and larger islands. (b) Magnified region of lower PCBM density demonstrates the irregular features of PCBM aggregates. (c) Magnified image of larger PCBM island reveals the higher local PCBM density and lack of apparent ordering.....85

**Figure 5.4** UHV-STM images of high density C<sub>70</sub>-PCBM monolayer regime: (a) Large scale film morphology after a 210°C 30min anneal, 2D hexagonal domains occurs. (b) Scaled image of the ordered 2D hexagonal domain. 2D hexagonal packing molecule and unit cell is marked with red color, and orientational defect and 2D quasi-hexagonal unit is marked with green color as shown.(c) Histogram of film a, reveals monolayer hexagonal packing molecules with FWHM = 0.15 nm. (d) FFT of image b, NND is measured as  $1.16 \pm 0.05$  nm.....87

**Figure 5.5** STM images of multilayer C<sub>70</sub>-PCBM films after 210 °C anneal for 30 min: (a) Both double-row structure and 2D hexagonal ordering can be found in the multilayer film. (b) Scaled image of a two layer area from image (a). The second layer has a shift in registration compared with the first layer molecules. (c) Height histogram of film (b) has two significant modes with FWHM = 0.1 nm for both and a height difference between two layers measured as 0.2 nm.....89

**Figure 5.6** Registration between first and second layer C<sub>70</sub>-PCBM: (a) STM images of partial bilayer C<sub>70</sub>-PCBM film from Figure 5.5b. Red circles marked first layer molecules (lower terrace) and green circles correspond to second layer molecule (upper terraces). (b) Lattices of first (red) and second (green) 2D hexagonal layers. Second layer molecules occupy two-fold bridge sites on first layer lattice.....90

**Figure 5.7** Schematic Model of Crystalline PCBM Bilayers: (a) PCBM dimer, that is the building block of the bilayer, joined by hydrogen bond between the two ester groups. The fullerene cage space is 1.78 nm based upon DFT calculations<sup>2</sup>. (b) Top view of the Bilayer PCBM structure, shows the fullerene cage exposed to the vacuum. (Cut functional groups for image clarity) (c) Side view, taken across the black line in b, depicts the hydrogen bonds and registration shift.....91

**Figure 6.1** Crystal structure of solid chloroform.....96

**Figure 6.2** Supramolecular ionic polymer used for the present study: The anion  $C_{186}H_{244}B_3IrN_6O_{12}^{3-}$  (blue) (counterion  $Me_2NH_2^+$ ) and the cation  $IrN_6C_{30}H_{24}^{3+}$  (olive) (counterion  $PF_6^-$ ) assemble into the linear supramolecular structures shown as above. This assembly is facilitated by the "twin bowls" shape of the anion unit.....98

**Figure 6.3** Topography of chloroform film on Ag (111) following microaerosol deposition on the room temperature substrate. (a) STM image shows a bi-layer structure, with irregular island voids. (b) Topographic profile across the vacancy island (blue line in (a)) reveals the 0.15 nm island depth.....100

**Figure 6.4** Trilayer of chloroform on Ag (111). (a) Large scale of STM image shows island structure. (b) Magnified monolayer region shows regions with ordering. (c) Line profile of ordered 2D hexagonal  $CHCl_3$  monolayer region (green line) reveals the nearest neighbor separation to be is 0.88 nm, suggesting a (3 x 3) chloroform adlayer.....101

**Figure 6.5** STM images of as deposited  $C_{186}H_{244}B_3IrN_6O_{12}^{-3}$  (twin bowls) and  $IrN_6C_{30}H_{24}^{+3}$  molecules, 0.084 mM in chloroform, 0.6 monolayer coverage on Ag (111). (a) Large scale of solute-induced triangular and rectangular structures. (b) Magnification of solute-induced islands reveals details of supramolecular solute packing. Darker region between islands corresponds to monolayer chloroform and possible counterions in direct contact to Ag (111).....104

**Figure 6.6** Molecular-resolved STM images of deposited  $C_{186}H_{244}B_3IrN_6O_{12}^{-3}$  (twin bowls) and  $IrN_6C_{30}H_{24}^{+3}$  supramolecules, 0.084 mM in chloroform, 0.6 monolayer solute coverage on Ag (111). (a) Internal structure of solute-induced triangular island. Expanded chains structure is shown in (b). (b) – (d) Unit cell dimensions of the supramolecular solute features are measured as  $a = 0.83$  nm and  $b = 1.67$  nm,  $\theta = 60^\circ$  by topographic line profiles. (e) – (h) Molecularly-resolved images of the darker monolayer regions. The lattice constants of the square  $CHCl_3$  unit cell are measured as 0.58 nm.....105

**Figure 6.7** Molecular model of  $CHCl_3$  ordering, depicting a c(4 x 2) adlayer on Ag (111).....106

**Figure 6.8** Schematic illustration of domain structures in solute-stabilized  $\text{CHCl}_3$  film: Striated yellow islands (A) are assemblies of twin bowls chain, with assemblies of differing chain lengths yielding triangular domains and assemblies of same-length chains yielding rectangular domains; Violet region (B) corresponds to the  $c(4 \times 2)$   $\text{CHCl}_3$  adlayer. Pink represents the domain-boundary region which is not molecularly resolved.....108

## Abbreviations

2-D	two dimensional
3-D	three dimensional
AFM	atomic force microscopy
C <sub>60</sub> -PCBM	phenyl-C <sub>61</sub> -butyric acid methyl ester
D	Debye
DFT	density functional theory
eV	electron volts
hcp	hexagonal close packed
HOMO	highest occupied molecular orbital
HOPG	highly ordered pyrolytic graphite
ITO	indium tin oxide
LEED	low energy electron diffraction
LUMO	lowest unoccupied molecular orbital
ML	monolayer
MPc	metal phthalocyanine
NND	nearest neighbor distance
OLED	organic light-emitting diode
OPV	organic photovoltaic
STM	scanning tunneling microscopy
TPD	temperature programmed desorption
UHV	ultrahigh vacuum
ZnPc	zinc phthalocyanine

# Chapter 1 Introduction

## 1.1 Motivation

Solar energy is an inexhaustible and environmentally friendly fuel source. In the past 15 years, solar energy use has expanded approximately 20 percent per year, and major markets for solar cells have been established in Japan, Germany, and the United States. However, high-power solar technologies are very expensive and require a lot of land area in order to collect the sun's energy at useful rates. For some applications, organic solar cells have attracted interest as alternatives to conventional silicon solar cells and as one innovative means to address the issue of low efficiency-to-cost ratio. Solar cells made with new organic materials, such as the fullerenes and their chemical derivatives, in combination with the electron donor polymer P3HT, have achieved reported power conversion efficiencies (PCE) from 3% to 6%<sup>3,4,5,6,7,8</sup> during the last ten years. More recently, the efficiency of organic/polymeric organic photovoltaic devices has been further increased to 8-10% (2011-2012)<sup>9,10,11</sup>. These improvements have come about through the utilization of refined organic component materials, improved device architectures and improved fabrication methods. Further research on organic solar cells is needed, however, before they can see more widespread utilization. Key issues must be addressed: OPV cell cost is still high, largely due to the costly manufacturing processes; efficiency needs to be improved to approach the theoretical limit of 29%<sup>12</sup>; lifetime is insufficient, particularly in comparison to their inorganic counterparts; physical model of device operation need to be tested and further developed. My thesis work presented herein involves

structural investigations of select organic photovoltaic (OPV) materials by surface science technologies.

When the first polymer-based solar cells were made, the active layer was only composed of a single-component material. For such single-component devices, the power conversion efficiency was ~1%. A major breakthrough for organic solar cell devices was achieved by generating an active layer composed of both electron donor and electron acceptor materials. The interface of the donor-acceptor materials is the heterojunction. Actual device structures are based upon the so-called “bulk heterojunction” consisting of a large number of internal heterojunctions that arise in the organic film matrix. The PCE of an OPV cell is highly dependent on this donor-acceptor bulk heterojunction geometry, which greatly impacts charge separation, recombination and charge transport at sub -100 nm length scales. Controlling the chemical morphology of the “bulk heterojunction” is believed to offer significant opportunities for improving the properties of organic solar cells. Equally important is to establish a detailed understanding of the relationship between chemical morphology and electronic properties at the nanoscale. These relationships provided fundamental insight into the physical operation of organic solar cells. Important structural features of the organic layers that must be explored and refined include (1) the impact of polymorphism (different molecular packing), (2) domain alignment, (3) domain size, and (4) the extent and direction of phase separation, and its dependence on sample processing conditions. Such structural variations are important because changes in heterojunction morphologies will impact the electronic and charge-transport properties. With the increased use of chemically functionalized fullerenes in

organic solar cells, considerably more structural variations may be anticipated in these active layer materials.

The organic film geometry believed optimal for device performance is illustrated in Figure 1.1. This gradient structure with interdigitated donor – acceptor domains provides a large donor-acceptor interfacial area, while providing efficient charge transport paths for the holes and electrons to reach the anode and cathode, respectively. Understanding how to realize such geometries is one of the goals of this research. The basic processes for photocurrent production are illustrated in Figure 1.1:

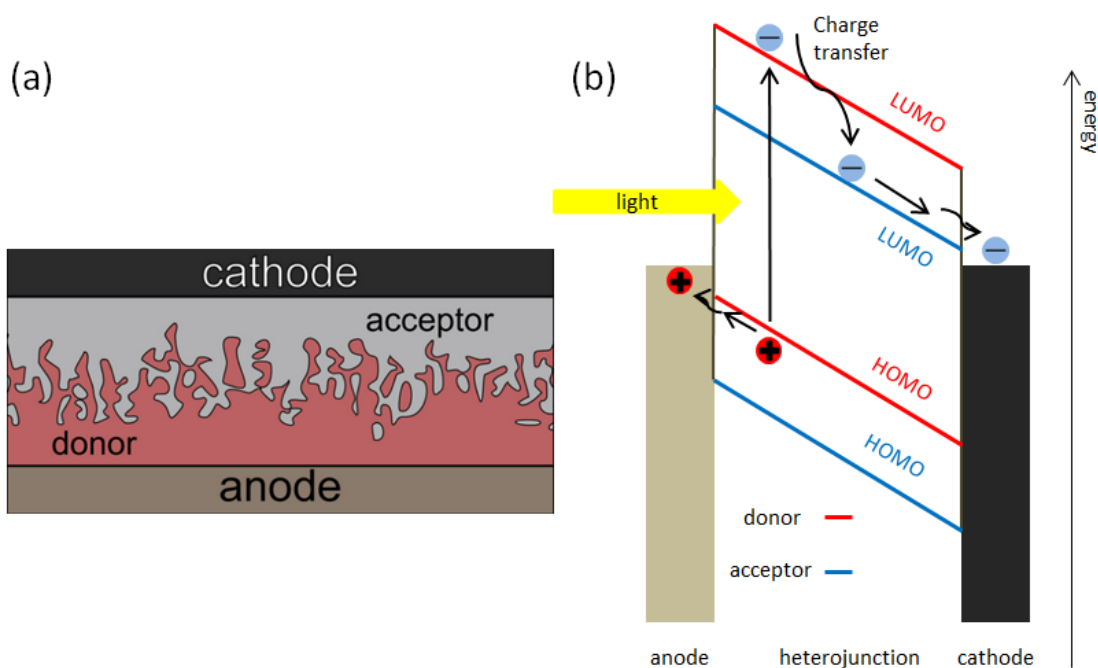


**Figure 1.1** Functional operation of an organic solar cell: (a) Schematic illustration of gradient heterojunction, which offers high interfacial areas for exciton unbinding and efficient charge transfer pathways to electrodes. (b) Processes of photocurrent production from incident light.

When donor molecules absorb light, excitons (electron-hole pairs) with strong binding energies ranging (0.1 to 0.2 eV)<sup>13</sup> are first created. In current OPV cells,

based upon two organic components, the heterojunction serves to dissociate these strongly bound excitons by the offset between the HOMO of the donor material and LUMO of the acceptor material. After exciton dissociation at the donor-acceptor interface, the resulting electron will transfer to the acceptor material, and the hole will transfer to the donor material. The role of the “bulk heterojunction” is twofold: (1) to maximize the donor-acceptor interfacial area, thereby increasing charge production. (2) to prevent exciton recombination and limit re-emission. In organic materials, excitons have a diffusion length on the order of 10 -15 nm<sup>13-14,15,16</sup>. If an exciton is created, an interface needs to be within about 10-15 nm or the exciton will simply recombine. These structural issues encourage the use of macroscopic bulk heterojunction which contains many interfaces. The actual charge path in a bulk heterojunction is as follows: The charge carriers are generated by photoinduced electron transfer from the LUMO of the electron donor to the LUMO of the electron acceptor. For efficient charge generation, the exciton in the blend has to reach an acceptor interface before recombination; therefore, the magnitude of the optimal phase separation is determined by the exciton diffusion length. For efficient photovoltaic devices, however, the created charge carriers need to be transported to the corresponding electrodes within their respective lifetimes, which depend on the charge carrier mobility of the materials. And finally, they are injected into the electrodes through organic - metal interfaces, creating an electrical current in the external circuit. According to this schematic mechanism, the organic-organic and the organic-metal interfaces are of tremendous importance because they determine the efficiencies of the successive steps of charge generation, transport, recombination,



injection, and extraction. Currently, the following approaches are pursued for optimizing OPV efficiency: First, the energy levels of HOMO and LUMO of donor-acceptor materials are aligned for effective exciton dissociation. The optical absorption of the donor materials used in solar cell devices should be within the solar spectrum regime. Second, the molecular morphologies along these interfaces should be optimized for efficient charge transfer. The ideal structure would be interdigitized donor-acceptor domains, which optimize the donor-acceptor interfacial areas and provide efficient charge transfer paths to the electrodes, as illustrated in Fig. 1.1. The dimension of donor-acceptor domains should be in the range of the exciton diffusion length (10~15 nm). The orientation between the donor-acceptor molecules should be optimized to facilitate charge transport. This is known as the orientational dependence of charge transport<sup>17</sup>.

This thesis project is seeking to test critical assumptions on the types of heterostructures that can be created and address questions such as: What are the lengthscales of donor-acceptor domains? Is it possible to control the interface structures? Which material contacts which electrode? Does the molecular density of the donor and acceptor material matter? How would it impact the HOMO/LUMO level? Does orientation matter in interface formation – and how does it impact charge separation? Can it be reliably controlled? For the kinds of materials that have emerged as the most efficient organic solar cell materials – fullerene derivatives and organic oligomers – what are the intrinsic molecular features (shape, functional groups, polarity) that might impact all of the above?

Many of the ideas that have guided the development of the bulk –heterostructure concept come from the world of engineering, where chemical effects are not carefully considered. However, in order to reduce the cost of solar cells and make them green, organic solar cells are generally fabricated by liquid deposition. Therefore, functionalization is needed to increase solubility and enable manufacturing. Understanding the impact of functional groups on materials architectures is thus of critical importance.

The main goal of this thesis is to investigate the fundamentals of molecular – metal interface formation, nanocrystallization and phase separation in molecular materials, hugely important but difficult to investigate on the nanoscale. These studies require a methodology that involves the integration of precise film growth methods (preferably from a liquid source) coupled with a structural tool that offers molecular resolution imaging. In principle, UHV-STM and non-contact-AFM offer such resolution, but in practice they are more readily performed on crystalline planar materials. In the present thesis, I will push the boundary on the application of UHV-STM to molecular organic materials from the monolayer – to multilayer regime. Through *in situ* growth with a novel aerosol deposition source, I will create precisely controlled film thicknesses and stable tunneling junctions. I use this methodology to explore the molecular-level mechanisms of how interfaces form, domains form, and materials undergo donor-acceptor phase separation. Moreover, I will obtain initial insights into how the solvent, the agent to transport the functional organic solute to the surface, impacts structure evolution of the deposited films.

All experiments conducted in this thesis are on model donor-acceptor systems. The model donors are Zinc phthalocyanine (ZnPc) and its functionalized derivative Zinc tetranitrophthalocyanine (TN-ZnPc). The model acceptors are the fullerene derivatives [6,6]-phenyl-C<sub>61</sub>-butyric acid methyl ester (C<sub>60</sub>-PCBM) and [6,6]-phenyl-C<sub>71</sub>-butyric acid methyl ester (C<sub>70</sub>-PCBM). Detailed motivation for these model systems will be described in section 1.2.1. Crystalline and well-defined growth substrates are needed to enable molecular-resolution studies by STM. Here we choose (111)-oriented single crystals of gold as well as silver to serve as model electrodes. Silver is utilized in solar cell applications, and is thus technologically relevant, and comparisons between the silver and gold electrodes allow investigation of the role of the growth substrate.

To gain insight and anticipate how interfaces form and structure evolves in our model PCBM and ZnPc systems, I briefly summarize film nucleation and growth mechanisms developed largely for atomic systems. This framework will provide a starting point for understanding structure evolution in my molecular films.

Nucleation and growth of an *atomic* film occurs through the following possible processes: 1. Desorption, in which an impinging atom may be directly reflected from the surface or an adsorbed atom may detach from the substrate (or substrate islands) and enter the gas phase. 2. Deposition, the atom may be reflected but then hits another incoming atom and redirected to the substrate. 3. Adsorption, the atom can weakly stick (e.g. bond through van der Waals interactions), known as physisorption, or may find a place to bond strongly to surface atoms, known as chemisorption. 3. Diffusion, adsorbed atoms can diffuse in a 2-D random walk manner on a flat terrace or along

the step edges. Cross-step diffusion is also possible, but less probable due to higher diffusion barriers at the step edge. 4. Nucleation, the atom can attach to an existing island edge or combine with other adsorbed atoms to nucleate a new island. Generally speaking, diffusing atoms eventually find energetically preferred sites which are of higher coordination, such as sites at the step- or island- edge or surface vacancy sites. Moreover, heterogeneous nucleation at irregularities like steps edges and vacancies of the substrate is most favored. Figure 1.2 summarizes all the above mechanisms for an incoming atom:

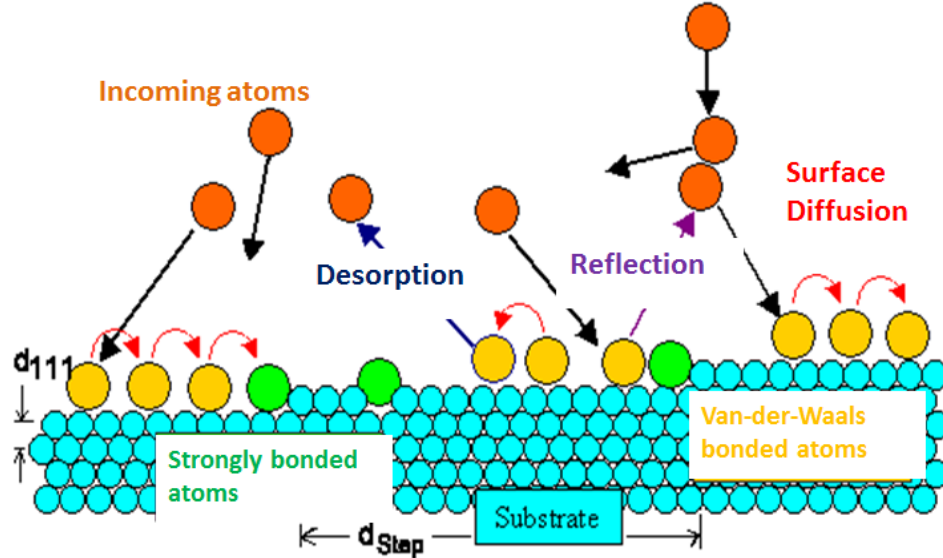


**Figure 1.2** Schematic illustrations of typical atomistic processes occurring during atomic film growth.

In this figure, atoms will become fixed if they find highly attractive positions, and the sticking coefficient depends on many parameters. The most important parameters are deposition rate  $F$ , substrate temperature  $T$  and the binding energy  $E$  between adsorbate atoms and substrate atoms. The process by which atoms (or in our case *molecules*) deposited on substrates evolve towards nanoscale structures is inherently a

non-equilibrium phenomenon<sup>18</sup>. Final surface morphology is determined, in large part, by the competitive result of these different atomistic processes. Ever since the invention of atomic level resolution imaging techniques such as STM and due to computational advances, atomic scale information of growth mechanisms has become more readily available. In practice, thin film growth is generally controlled by the competition between thermodynamics and kinetics (usually controlled by flux  $F$ ). Surface diffusion is a thermally activated process and film growth is described as a kinetic process. When the adsorbate diffuses from one stable adsorption site to another, it needs to overcome a diffusion barrier. The average distance it traveled before meeting another adsorbate is determined by the ratio of diffusivity ( $D$ ) and flux rate ( $F$ ), either for nucleation of a new aggregate or attachment to a formed island. When thermodynamics dominates the film growth process, known as quasi-equilibrium growth, the adsorbate has enough time to explore the potential surface to reach a minimum energy configuration. On the other hand, when kinetics dominates the growth process, the adsorbate will adopt metastable crystal structures. A high  $D/F$  ratio is typically preferred in epitaxial growth since growth under slow thermodynamic control generally translates to long-range ordered structures. For practical (experimental) reasons, and to facilitate study of kinetic factors, low temperature experiments with a low  $D/F$  ratio are conducted.

The molecular systems investigated in this thesis have anisotropic shapes and inter-molecular interactions that make film growth much more complex than atomic film growth. Polymorphism (multiple phases) are more common, interfaces generally don't grow layer by layer, and crystallization is generally more problematic. I will present

studies on single-component films to explore these effects. Additionally, for binary films (such as the donor-acceptor OPV systems), I will show a thermally driven interface rearrangement. Local density has a critical impact on binary film structure evolution, and a spontaneous vertical phase separation is favored by electrostatic energy.

## **1.2 Organic Semiconductor Materials**

### **1.2.1. Our model system**

In this thesis work, we mainly focus on fullerene derivatives, C<sub>60</sub>-PCBM and C<sub>70</sub>-PCBM, and metal phthalocyanine (MPc) molecules. We will explore molecular adsorption, ordering and displacement at coinage metal surfaces Au (111) and Ag (111).

Metal phthalocyanines (MPc) are a typical family of fully  $\pi$ -conjugated macrocyclic molecules with high thermal stability and versatile functionalities. As a widely used family member, ZnPc is used in OPV cells as an electron donor material, and it is reported that the ZnPc/C<sub>60</sub> heterojunctions offer a VOC (open circuit voltage) of 0.54 V<sup>19</sup>. For bulk heterojunction devices, the VOC should be linearly related to the frontier orbital energy offsets between the HOMO of the donor and the LUMO of the acceptor<sup>20,21,22,23,24</sup>. Thus, the surface structural organization of ZnPc with photoactive molecular species, such as fullerenes, is of great interest. As a practical matter, ZnPc has limited utility, due to its limited optical absorption match to the solar spectrum (Naphthalocyanine being better). However it is highly suitable as a model system.

Fullerenes, C<sub>60</sub> and C<sub>70</sub>, are also well known and widely studied electron acceptor materials<sup>25,26</sup> in semiconductor solar cell and OPV devices. Relative to C<sub>60</sub>, C<sub>70</sub>, the

second most abundant fullerene, has been reported to yield a 20% increase in efficiency in OPV device performance<sup>27</sup>. Charge transfer between C<sub>70</sub> and other electron donor materials is also greater than C<sub>60</sub><sup>28,27</sup>. All these properties motivate studies and comparison of C<sub>60</sub> and C<sub>70</sub> thin films as model systems of semiconductor polymer solar cell materials.

### 1.2.2 Functionalized fullerenes

Although fullerenes have significant advantages as electron accepting materials, however, they possess environmental disadvantages. Fullerenes, such as C<sub>60</sub> and C<sub>70</sub>, are hydrophobic. Consequently, fullerene molecules clump together in water, forming aggregates of thousands of molecules. These aggregates are reported to be toxic to microorganisms and even fish. Also, the solubility issue prevents fullerenes from low-cost liquid deposition procedures in solar cell industry. Functionalized fullerenes provide a means to address these solubility and toxicity issues. Following the first preparation of C<sub>60</sub> and C<sub>70</sub>, intense efforts were devoted to the synthesis of functionalized fullerenes<sup>29,30,31</sup>. Functionalized fullerene molecules not only inherit great chemical and physical properties from their parents, but also have increased solubilities in a variety organic solvents and decreased toxicity in the environment. Moreover, functionalized fullerenes have been reported to have very appealing photo-, electro-chemical, physical and biological properties, and promising applications in various areas. For example, Phenyl-C61-butyric acid methyl ester (C<sub>60</sub>-PCBM) and 1',1'',4',4'' Tetrahydro-di[1,4] methanonaphthaleno [1,2:2',3',56,60:2'',3''] [5,6] fullerene-C<sub>60</sub> are superior acceptors for high-performance polymer solar cells<sup>32</sup> and photo-detectors; Fullerenols can be used as antioxidants and biopharmaceuticals.

Most derivatives are methanofullerenes, the most versatile and widely studied class of fullerene adducts made by chemical addition reactions (like Diels-Alder reactions). The guidelines to design new fullerene acceptors for OPVs involve optimization of the following aspects: 1. Type of fullerene core, e.g. C<sub>60</sub> or C<sub>70</sub>. 2. Sort by functional group, e.g. phenyl butyric acid methyl ester, indene, or silylmethane. 3. Number of addend(s), e.g. Mono-, Bis- or Tri-. 4. Regioisomer of fullerene adduct. 5. Stereoisomer of the fullerene adduct with different spatial orientation of the addend(s). Despite these synthetic efforts<sup>29,33</sup>, C<sub>70</sub>-PCBM remains the most efficient solar cell fullerene component. The greatest strides in improving OPV performance appear to be in controlling the structure of the C<sub>70</sub>-PCBM (and donor) domains, and the interfaces between the organic and electron materials<sup>34</sup>.

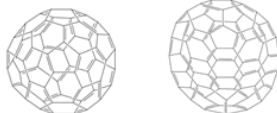
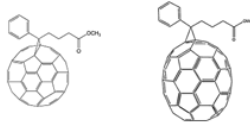
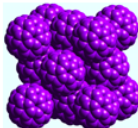
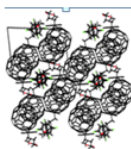
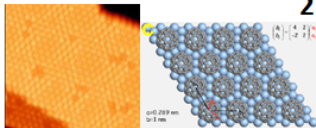
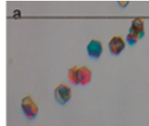
In this thesis work, we select C<sub>60</sub>-PCBM, and C<sub>70</sub>-PCBM as our model systems. As efficient fullerene acceptors used in organic solar cells, PCBM has some key features: The LUMO level of C<sub>60</sub>-PCBM is -3.91 eV<sup>35</sup>. In combine with the polymer P3HT, the VOC (Open-Circuit Voltage) is 0.54 V<sup>36</sup>. It has high electron mobility. It has µg/L solubility in a variety of organic solvents. It does not absorb solar radiation and therefore does not compete with the “donor” component.

### **1.2.3 Crystal habits of fullerenes**

In order to understand how nanostructure evolves in fullerene films, we first review the bulk crystal habits of fullerenes. Researchers have examined the crystallization of fullerene molecules for decades, as shown in Figure 1.3. Fullerenes C<sub>60</sub> and C<sub>70</sub> have well known 3D bulk fcc crystal structures, containing freely rotating molecules. Monolayers of C<sub>60</sub> and C<sub>70</sub> readily form highly ordered 2D hexagonal packing



structures in vapor deposited films. However, for functionalized fullerenes C<sub>60</sub>-PCBM and C<sub>70</sub>-PCBM, the crystal habits are very different from their parents. From solution they tend toward co-crystal formation with the solvent molecules like chlorobenzene or chloroform<sup>37</sup>. Neat solvent-free crystals of C<sub>60</sub>-PCBM have recently been formed, utilizing a crystal-pulling method with very slow solvent evaporation<sup>38</sup>. In this thesis, the crystallization of C<sub>60</sub>-PCBM and C<sub>70</sub>-PCBM thin films using liquid aerosol deposition method will be investigated. We will show how the thin films evolve into ordered packing arrangements depending upon local molecular density. The 2D hexagonal monolayer phases are produced and characterized, indicating the accessibility of new growth phases by  $\mu$ -aerosol deposition.

Neat Fullerenes (C <sub>60</sub> and C <sub>70</sub> )		Functionalized Fullerenes(C <sub>60</sub> -PCBM,C <sub>70</sub> -PCBM)			
					
3D fcc crystal free rotatable		1	3D co-crystal (chlorobenzene)		3
hcp monolayer		2	C <sub>60</sub> -PCBM crystallization(solvent free)		4

**Figure 1.3** Crystal habits of fullerene C<sub>60</sub>, C<sub>70</sub> and functionalized fullerenes C<sub>60</sub>-PCBM, C<sub>70</sub>-PCBM. 1. 3D fcc crystal structure of C<sub>60</sub>. 2. C<sub>60</sub> 2D hexagonal monolayer film prepared by physical vapor deposition and a model of 2D hexagonal structure (*J Vac Sci Technol B*, **12**, 1942 (1994)). 3. 3D co-crystal structure of C<sub>60</sub>-PCBM with chlorobenzene (*Chem Commun*, 2116-2118 (2003)). 4. Neat (solvent free) C<sub>60</sub>-PCBM crystallites, grown from solution on a solid support through evaporative control (*Phys Chem Chem Phys*, **12**, 4473-80 (2010)).

### 1.3 Thesis Outline

The outline of this thesis is as follows:

In Chapter 2, the experimental procedures and instrumentations are described. A brief introduction to STM and the UHV system used in this thesis work are presented. The molecular deposition system and sample, tip preparation procedures are further described.

In Chapter 3, single component film structures for C<sub>60</sub>-PCBM and ZnPc are described and discussed as follows: 1. ZnPc film growth, with a focus on the solvent assisted- growth mechanics. 2. C<sub>60</sub>-PCBM polymorphism in monolayer films, in which three distinct crystalline phases may be generated through control of thermal energy and density.

Chapter 4 concerns the binary system of the fullerene C<sub>60</sub>-PCBM and ZnPc on the Au (111) substrate. We show how a distinct vertical phase separation occurs, independent of the film deposition sequence, indicating a thermodynamically favored structure. We show that electrostatic energy differences provide a driving force for this vertical separation mechanism and explore the influence of molecular density on vertical displacement.

C<sub>70</sub>-PCBM thin-film structures will be studied in Chapter 5 from the monolayer to multilayer regime by UHV-STM, with critical comparison to C<sub>60</sub>-PCBM structures. Bilayer films show registration through hydrogen bonding, and functional groups play key roles in multilayer formation.

Finally, we present studies of solvent layers and organization on growth substrates in Chapter 6. For this effort, we examine the unexpected solidification and stability of

solvent layers on the Ag (111) substrate under ultrahigh vacuum conditions. We examine the impact of solute supramolecules, notably ionic polymers, on chloroform adlayer structures and describe the organization mechanisms.

A summary and suggestions for future work are presented in Chapter 7.

## **Chapter 2 Introduction to Instruments and Experimental Procedures**

In Chapter 2, instrumental methods and detailed experimental procedures are reported. First, a brief introduction to Scanning Tunneling Microscopy (STM), the main imaging method used in this thesis work, is presented in section 2.1. Section 2.2 describes the detailed experiment procedures as follows: 2.2.1: The UHV-STM system; 2.2.2: Substrate (Au (111) and Ag (111)) preparation; 2.2.3: Tunneling Tip preparation for STM; 2.2.4: Pulsed micro aerosol molecular beam source for molecular deposition.

### **2.1 Scanning Tunneling Microscope (STM)**

#### **2.1.1 Background of STM**

Ever since its invention (Binnig and Rohrer, IBM-Zurich laboratories, 1981) the STM has become a core tool of nanoscale imaging and electronic structure probing of surfaces. It is the first of its general class of scanning probe microscopies (SPM), which opened up the wonders of revealing atomically-detailed images of structure in real space for scientists. It is also a powerful tool for creating and manipulating nanostructures one atom at a time. Although people call it a microscope, scanning tunneling microscope (STM), does not work like optical microscopes. It images the surface of conducting materials using electrons, and provides contrast through the physical mechanism of “tunneling”, and has a field of view determined by the motion of the STM tip. In addition to atomic level resolution imaging, the STM tunnel junction can also perform spectroscopy, known as Scanning Tunneling Spectroscopy

(STS), providing insight into the local density of states (LDOS) of material surfaces through the current-voltage (I-V) relation.

### **2.1.2 Basic principles of tunneling**

The quantum tunneling effect, which describes the ability of an electron to tunnel through a vacuum barrier from one electrode to another, is well studied in many textbooks such as: Introduction to Quantum Mechanics (Griffiths, section 8-2, pp. 320-325) and Quantum Physics of Atoms, Molecules, Solids, Nuclei and Particles (Eisberg and Resnick, pp. 199-209). With experimental observations of electron tunneling, the classical perception of nature was challenged to a great degree.

Particles with small masses such as electrons can be described also as waves. The tunneling effect is one of the phenomena that particles exhibit that arises from the wave character of matter. To illustrate with a simple model, first consider the one-dimensional finite potential step problem (Fig. 2.1). Assume an electron travels along the x-axis from a region with potential energy  $V = 0$  to a region with potential energy  $V = V_0$  (finite barrier potential). In classical mechanics, if the kinetic energy  $E_k$  of this particle is smaller than the barrier height  $V_0$ , the particle wave will be totally reflected from the barrier; in other words, the particle can only be found in the  $V = 0$  region. However, unlike classical particles, in quantum mechanics, the particle wave will not be totally reflected from the barrier when  $E_k < V_0$ . Because of the wave-like property, electrons can “penetrate” potential barriers and have a probability of occupying the classically “forbidden region” (where  $V = V_0$ ). In this classically forbidden region, the particle wavefunction decays to zero exponentially over a distance determined by  $V_0$  and  $E_k$ . Figure 2.1 shows schematic illustration of this case:

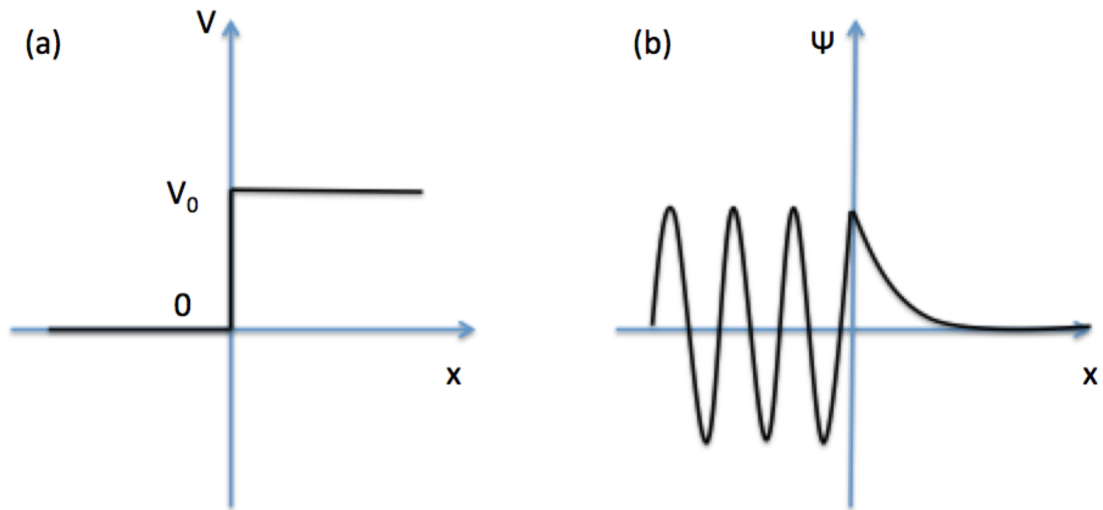


**Figure 2.1** (a) One dimensional potential step with a barrier height of  $V_0$  and corresponding wavefunction for a traveling electron impinging on the barrier with  $E_k = V_0/2$  (b) in quantum mechanics.

A model that more closely resembles the operation of the STM involves a one-dimensional rectangular potential barrier, as shown in Figure 2.2. Note that in the case of a rectangular barrier, the particle wave does not decay to zero when it reaches the other side of the potential barrier, but retains a nonzero probability amplitude  $T$  (known as the transmission coefficient) on the other side of the barrier. This phenomenon is known as transmissive tunneling:

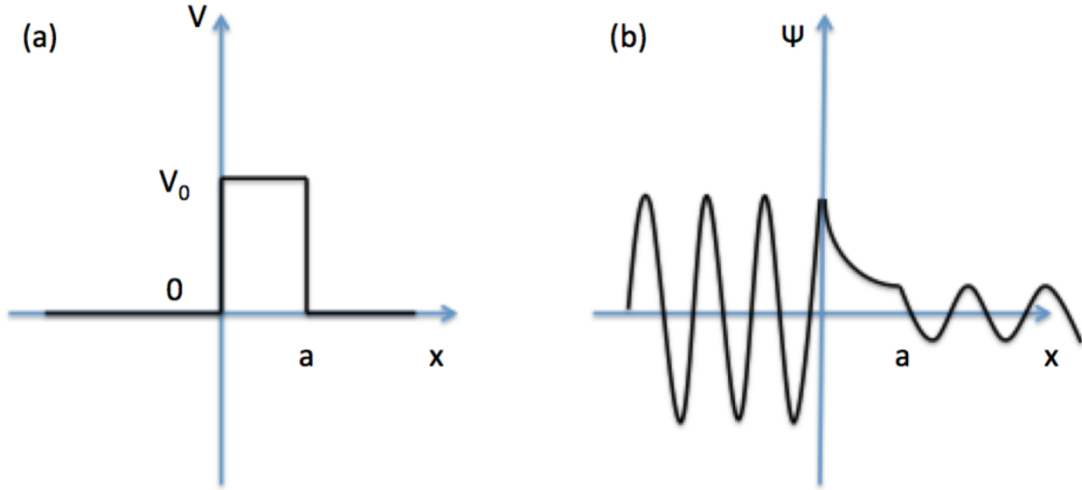


**Figure 2.2** (a) One-dimensional rectangular barrier potential of height  $V_0$  and width  $a$  and corresponding electron wavefunction for an incident electron with a kinetic energy  $E_k = V_0/2$  (b).

The transmission coefficient can be determined by Schrödinger equation and boundary condition equations as:

$$T \cong \exp(-2ka) \quad \text{Eq.2.1}$$

Here  $k$  is determined by the particle's kinetic energy  $E$  and the barrier potential  $V_0$

by:

$$k = \sqrt{\frac{2m(V_0 - E)}{\hbar^2}} \quad \text{Eq.2.2}$$

Thus, when a particle approaches the barrier from the left, it has a probability of either being reflected from the barrier front surface or being transmitted to the right ( $T$ ), and the relationship between reflection coefficient ( $R$ ) and transmission coefficient ( $T$ ) is  $R+T=1$ .

The basic principle of STM operation is based on the case of the rectangular potential barrier. Because of the tunneling effect, the electrons within an electrical conductor (such as metal or suitably prepared semiconductor) are in states well described by free particle wavefunctions. Electrons are not totally confined within the

conductor material, and electron density does not drop to zero at the material surface. Instead, the electron wavefunctions decay over a distance of a few nanometers outside the surface. As a result, when one brings two conductors (such as the STM tip and sample) very close to each other (within a fraction of nm) so that they are separated by a potential barrier (such as the vacuum gap or a barrier due to an insulating film), electrons can flow between the two conductors by tunneling. In other words, the tunneling wave of the sample electrons  $\Psi_s$  and the STM tip electrons  $\Psi_t$  overlap in the gap, as shown schematically in Fig. 2.3. Thus, if an electrical circuit is completed between the two conductors, this electrons flow can be sustained and measured as an electrical current. The magnitude of this electrical current  $I$  is highly sensitive to the separation barrier, with an exponential dependence on distance  $a$ .

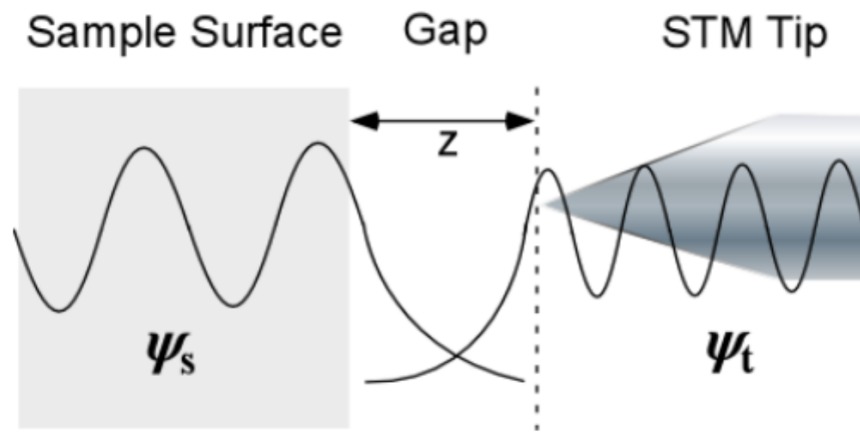


**Figure 2.3** Schematic of STM one-dimensional tunneling junction.

In STM, a very sharp metal tip, such as tungsten or platinum, scans above a conductive sample surface. These tip materials are chosen because of chemical and mechanical stability, and the ease of producing sharpened tips terminated with very sharp protrusions consisting of few atoms. A schematic illustration of an STM tip in tunneling distance to a conductor substrate is shown in Fig. 2.4.



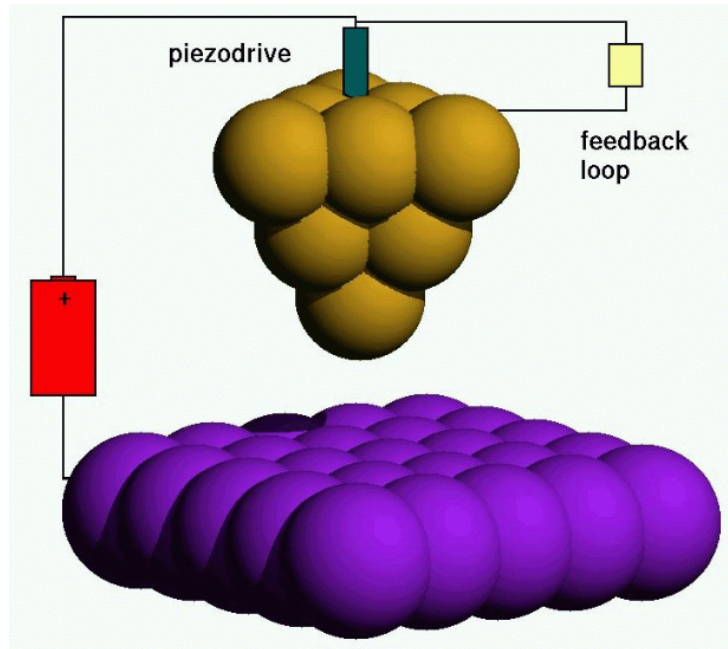


**Figure 2.4** Illustration of an ideal STM tip (at top) which narrows down to an atomically sharp point. The tunneling current region is determined by proximate (exponential dependence on distance). The sample to be imaged is shown at the bottom.

We reasonably assume that just the one (or cluster) of atoms that terminate the tunneling tip contributes the vast majority of the tunneling current because the additional distance between the sample and the other tip atoms leads to an enormous reduction in their tunneling currents due to the strong exponential drop-off of tunneling current with distance.

The specific geometry of the tip-sample junction is neglected in simple STM theory, and tunneling is modeled as a one-dimensional system as described above. In actuality, STM tunneling is more complicated than the simple one-dimensional barrier potential case as follows. First, in order to keep the tunneling current flowing, an electrical “bias” voltage must be applied between the tip and sample. The applied bias voltage depends mainly on the workfunctions of tip and sample materials. This creates, in turn, a bias electric field across the gap between tip and sample. This

electric field modifies the potential energy the electron experiences above the Fermi level ( $F_f$ ), as shown schematically in Figure 2.5. Second, the potential energies of the electrons in the tip and the sample vary according to the different workfunctions of different conductors. Third the local density of states (LDOS) of the tip and sample within the energy interval allowed for tunneling needs to be considered. The interval corresponds to the energy range where the occupied states of the sample and the unoccupied states of the tip are overlapping (for positive bias, vice versa for negative bias) (Fig 2.5).

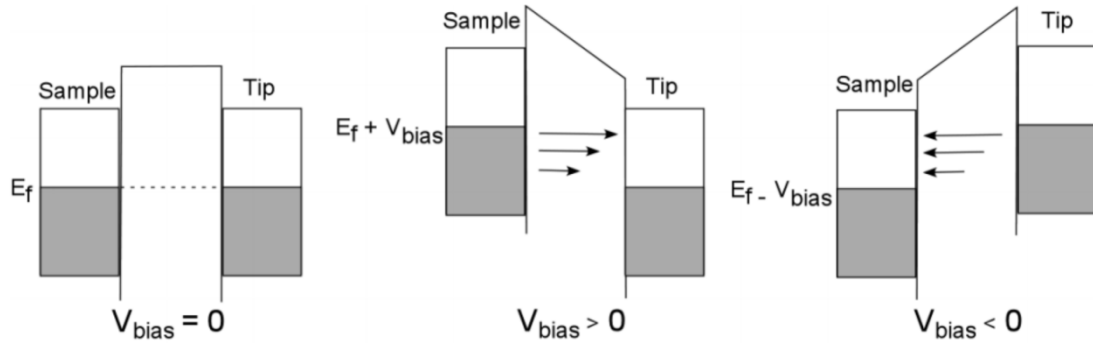


**Figure 2.5** Schematic of electronic band alignment for a sample-tip tunneling junction. The grey area represents electron filled states (occupied level) and the white area represents empty states, ready to accept electrons (unoccupied level). By application of a bias voltage  $V_{bias}$ ,  $E_f$  of the sample is modified. Arrows showed direction of electron flow between tip and sample.

Based on the discussion above, instead of a constant potential barrier, a sloping potential energy barrier results upon application of the bias voltage with:

$$V(x) = W - e\epsilon a \quad \text{Eq.2.3}$$

where  $e$  is electric charge,  $W$  is the work function for one of the metals,  $a$  is the distance across the gap, and  $\epsilon$  is the electric field from the applied bias voltage. The resulting STM transmission coefficient  $T$  is proportional to the tunneling current,  $I$ , and may be determined as:

$$T \cong \exp \left( -2 \int dx \sqrt{\frac{2m}{\hbar^2} (V(x) - E)} \right) \quad \text{Eq.2.4}$$

This STM transmission coefficient is the integral of the transmission coefficient over the local density of states of the tip and the sample. Note that this detailed relation retains a tip-sample tunneling current vs. distance relation that varies approximately exponentially.

### 2.1.3 STM operations

In real STM operation, piezoelectric materials are used to control the tip's motions. These piezoelectric materials vary their dimensions depending on the applied voltage. For example, one polarity of voltage can shorten the piezoelectric material, while the opposite polarity expands the material. By varying the applied voltage of the piezoelectric, the position of the STM tip thus can be finely controlled both in-plane with the sample (the x-y plane) and in the tip-sample direction (z).

The distance z between tip and sample, which strongly impacts the magnitude of the tunneling current, can provide detailed surface information as discussed above. To measure this distance, STM is typically performed by setting a constant height or a constant tunneling current. The two corresponding operation modes are known as constant height mode and constant current mode. In the first mode, while the tip is scanning horizontally over the surface along the x-y direction, the height of the tip is fixed over the *average* surface plane, and the local tip-sample distance thus varies with the sample's atomic-level structures. Variations in the local tip-sample distance are sensed as changes in the tunneling current. The tunneling current  $I_t$  is thus mapped as a function of x and y, where high current corresponds to a raised area of the surface (smaller tip-sample distance) and low current corresponds to a valley area of the

surface (larger tip-sample distance). Thus, STM can image the topography with atomic-level precision (if the tip is atomically sharp). However, this mode has a drawback when imaging rough surfaces: when scanning a rough surface with feature heights comparable to the tip-sample distance, the tip may crash into the feature, leading to tip damage (and loss of resolution). The alternative constant current mode addresses this problem, and is the preferred mode of imaging in this thesis. In this mode, we first fix the feedback current as a constant value (known as the reference current). In this case, when the tip approaches a protrusion on the sample surface, the tunneling current increases and the feedback circuit responds by retracting the tip, restoring the tunneling current to the reference value. In contrast, when the tip approaches a depression on the sample surface, the tunneling current decreases, and the feedback circuit lowers the tip until the tunneling current returns to the reference value. The position of the tip  $z$  is recorded to map the surfaces' topography as  $z(x, y)$ .

Two methods are used to create surface images. Typically colors are used to represent either current (Constant Height Mode) or height (Constant Current Mode).

## **2.2. Experimental Setup**

### **2.2.1 Our UHV-STM system**

Ultra-high vacuum, known as the vacuum regime characterized by pressures lower than  $1 \times 10^{-9}$  Torr, is indispensable in surface science. UHV enables atomic level studies, as molecules at ambient have collisional frequencies with the surface on the order of  $Z = 10^7$  collisions/nm<sup>2</sup>s, resulting in the formation of a monolayer in just  $10^{-6}$  s. Consequently a vacuum pressure of  $10^{-10}$  Torr will reduce the timescale for formation of a monolayer from  $10^{-6}$  s (at atmospheric pressure) to  $10^4$  s. This enables detailed

studies on reactive surfaces for a period of 3 - 4 hours. In the case of the less reactive surfaces studied in this thesis, surfaces can be prepared and studied under UHV for a period of up to 3 days.

The UHV analysis system used for this research consists of two separately pumped chambers, a main vacuum chamber and loadlock, which may be vacuum - isolated by a gate-valve, as shown in Fig 2.6. The main UHV chamber contains tools for sample analysis (STM, Low Energy Electron Diffraction (LEED), and Auger Electron Spectroscopy (AES)), gas dosers and knudsen evaporation cells, a mass spectrometer for gas analysis and a sample manipulator. The loadlock is a small ante-chamber which can be used for rapid exchange of tips and samples, as well as for materials deposition. Freshly prepared metal substrates are first loaded into the loadlock through an entry port. Film deposition can be performed in the loadlock using either a molecular beam aerosol deposition source, or by an evaporation cell. Preliminary substrate-preparation processes such as cleaning and annealing and sample analysis (typically by STM) are performed *in situ* in the main UHV chamber by transfer of samples through the gate-valve, utilizing a magnetic transfer device. A base pressure better than  $1.2 \times 10^{-9}$  Torr in the UHV chamber is maintained for all characterizations by STM in this thesis.

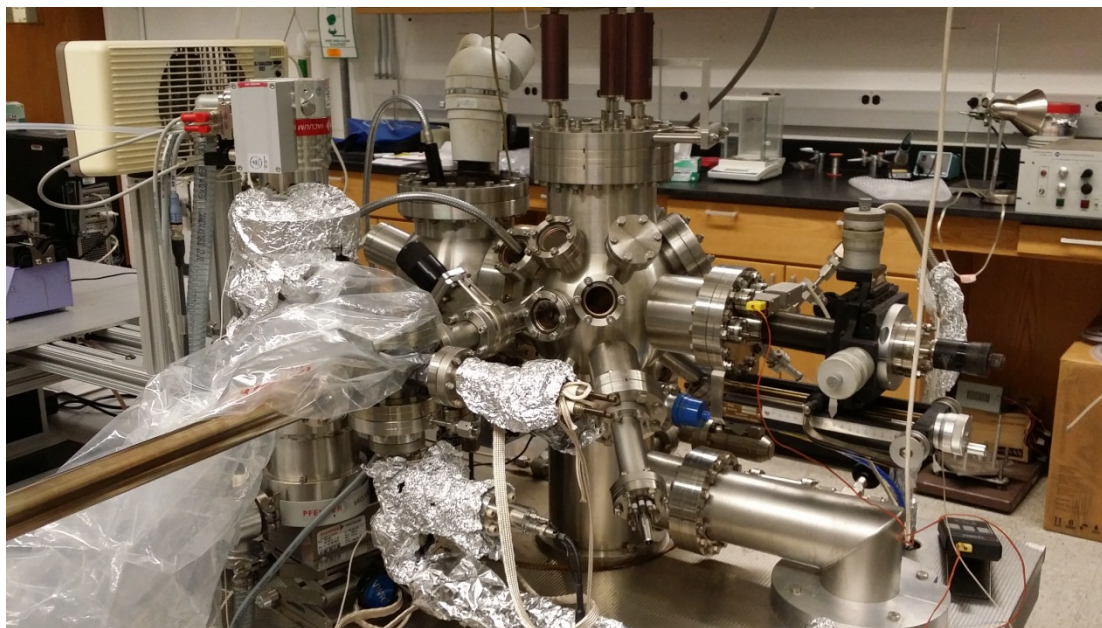


**Figure 2.6** UHV-STM analysis system with fast entry loadlock used in this thesis research.

### **2.2.2 Substrate Au (111) and Ag (111) preparation**

In this thesis, we use single crystalline coinage metal substrates, Au (111) and Ag (111), which have been cut, polished and oriented to an accuracy of  $0.25^\circ$ , as substrates for molecular film growth. The reasons these coinage metals are chosen are as following:

1. Gold and Silver are very popular electrode materials in practical use, and the (111) orientations are the most common.
2. Gold and silver are surfaces of low reactivity and thus allowing moderate adsorbate-substrate interaction.
3. Procedures for the cleaning and reconstruction of single crystalline Au (111) and Ag (111) are well established.

The single crystals are mounted on tantalum STM sample plates, for transfer into UHV system through the loadlock entry port; additional preparing and cleaning are performed in the main chamber. The procedure to generate well-ordered Au (111) surfaces typically involves two cycles of Argon ion sputtering (30 minutes, 1000 V, and 10 mA) and subsequent annealing to 480-490 °C for 20 minutes. The procedure to generate well-ordered Ag (111) surfaces also involves two cycles of Argon ion sputtering (25 minutes, 1000V, and 10 mA) and subsequent annealing to 500 °C for 20 minutes. In the case of Ag (111) surfaces, the crystals are periodically subject to light oxidation to remove carbon impurities. This involves dosing the Ag (111) surface with 300 L of O<sub>2</sub> at a temperature of 300 °C. These processes generate Ag (111) surfaces with typical terrace widths over 100 nm, as shown in Fig. 2.7. Based upon fcc lattice constants of Au, 0.288 nm, and Ag, 0.289 nm, the 100 nm terrace width corresponds to terraces that are 173 atoms wide for Au (111) and 172 atoms wide for Ag (111).

The terraces are generally bounded by irregular step spacing resulting from the relative low sample annealing temperature, which is insufficient to fully equilibrate the surface structure. Additionally, residual impurities can cause steps to be pinned, creating highly curved step edges, as per the Ag (111) steps in Fig. 2.7. For the STM measurements, we will focus our studies on large Au (111) and Ag (111) terraces.

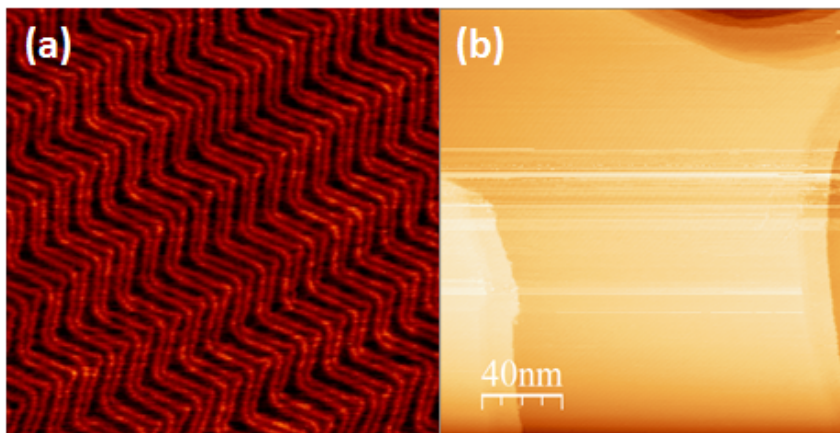


**Figure 2.7** Representative STM images of atomically clean Au (111), revealing the characteristic herringbone reconstruction, 35 ×35 nm (a). Ag (111), step bunch at the upper right indicates a step pinning site due to a local impurity (out of view) (b).

### 2.2.3 Tip preparation for STM

The STM tips used in this thesis research are made from tungsten wire with 0.25 mm diameter. In order to achieve a sharpened tip suitable for STM imaging, a two-step tip sharpening process is used:

- 1) Coarse polishing using 2.0 N (112 g/L) potassium hydroxide (KOH) solution.

In this process, the end of a 1 cm length cut wire (Figure 2.8a) is dipped into the KOH solution (insertion length = 10 mm) for quickly while applying a 25 V (AC RMS) coarse voltage between the wire and another copper electrode immersed in the solution. The untreated wire end is then clamped, and the treated end is inserted normal to the KOH (aq) liquid surface to a depth of 3mm deep with application of a 8-10 V (AC RMS) coarse voltage for 50 seconds.

This process results in a tip with tapered end as shown in Figure 2.8b.

- 2) Fine polishing using 0.5 N (23 g/L) KOH solution.



A Pt-Ir loop electrode (5 mm diameter) is used for the final polishing. The loop is inserted into the KOH solution to generate a suspended liquid film. The Tungsten tip is then mounted on a micrometer head so that the tip end can be rastered normal to the solvent bubble with application of a 3-8 V (AC RMS) coarse voltage applying for 3-5 seconds between tip and solution. This process is monitored under an optical microscope until the desirable tip shape is achieved. This process results in a tip that terminate with an atomically sharp (atoms or cluster terminated) tip end, capable of achieve STM images with atomic resolution, as shown in Figure 2.8c.

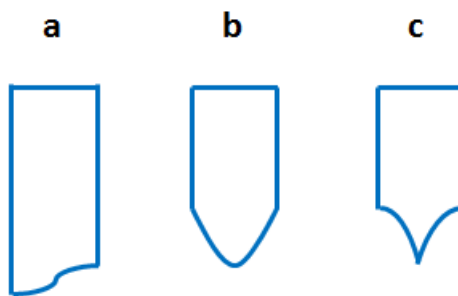


**Figure 2.8** Schematic of tip end before and after corresponding polishing: (a) cut end; (b) tapered end; (c) atomically sharp end.

#### 2.2.4 Liquid $\mu$ aerosol molecular beam deposition

An important accomplishment in this thesis work is the development of deposition procedures suitable for the introduction of nonvolatile species into the UHV environment with carefully controlled fluxes. Methods for introducing nonvolatile species into vacuum were first developed by John Fenn for mass spectrometry applications<sup>39</sup>. "Electrospray methods" have revolutionized mass spectrometry, and resulted in the awarding of the 2002 Nobel Prize. More recently, Toshiki Yamada and

coworkers have successfully introduced nonvolatile species into the UHV environment through the use of an aerosol carrier<sup>40</sup>. Materials such as carbon nanotubes, fullerenes and other semiconductor polymer solutions were converted into aerosols using ultrasonic and pneumatic nebulization. The aerosol vapor was then expanded through a pulsed molecular beam nozzle into the ultrahigh vacuum system. The focus of Toshiki Yamada's efforts was on minimizing sample consumption in the preparation of supported structures for individual surface science analysis. Such aerosol-molecular beam technology provides improved deposition control for nonvolatile species, making it highly suited to fundamental research on various transparent electrode materials.

In this thesis we have fabricated an aerosol-molecular beam deposition source that improves upon the Toshiki source with three innovations: (1) Introduction of an in-line cloud chamber to reduce the aerosol size to 1-10  $\mu\text{m}$  through gravimetric filtration. (2) Addition of two stages of differential pumping with a compact design to further improve the liquid-to-UHV vacuum transition, while maximizing flux to the sample through reduced nozzle-sample distance. (3) Utilization of a modular design; so that the source can be attached to any UHV systems with an available 2 3/4" conflate port with line-of-sight to the sample.

The new aerosol molecular-beam deposition source is illustrated in Fig. 2.9.

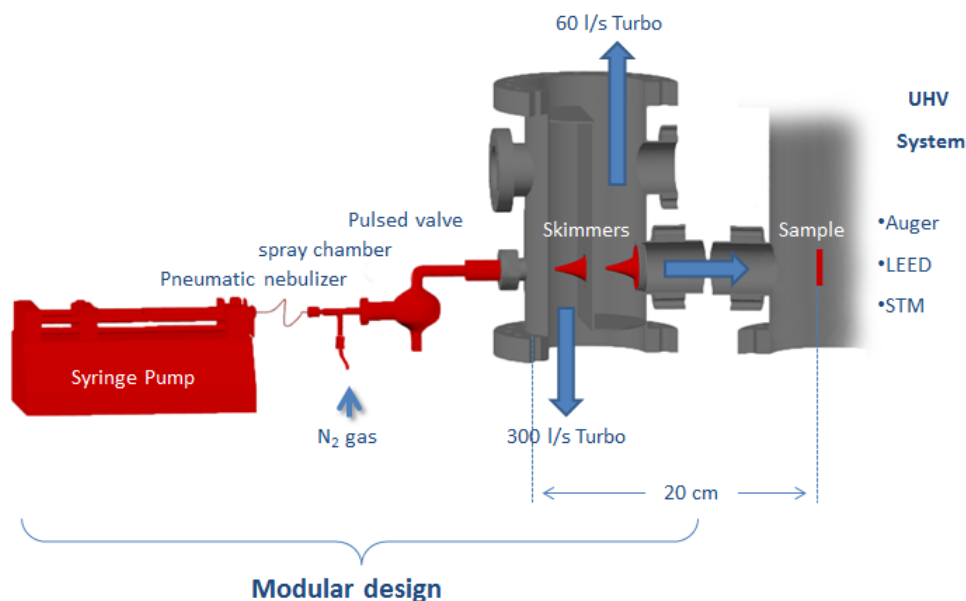


**Figure 2.9** Schematic of aerosol molecular-beam deposition source.

The operation of the pulsed aerosol molecular beam source is as follows: Briefly, the sample solution is pumped with a syringe pump (Harvard Instruments: 702208 Series 11- 0.0014  $\mu\text{L/hr}$  minimum flow; 1.59 L/hr maximum flow & Hamilton Gastight Series 1000 syringe, 2.5 mL volume with TLL connector) at a predefined rate of 0.075 mL/min and introduced into the T-shaped pneumatic nebulizer (Glass Expansion: AR40-1-FM01E, 0.1 mL/min uptake), where it combines with N<sub>2</sub> gas (970 Torr) and is converted to a dense mist. This mist is further introduced into a cyclotron cloud spray chamber (Glass Expansion: 20-809-0261-HE), where microdroplets are separated gravimetrically, and smaller 1-10  $\mu\text{m}$  droplets are subsequently delivered to the nozzle source. The pulsed valve (General Valve Series 9) has a 1 mm orifice that is electrically actuated by a solenoid coil. The pulse duration (0.8 ms typical), total number of molecular beam pulses, and pulse interval (1 s typical) are electronically controlled. The aerosol that passes through the molecular beam source is entrained in a supersonic molecular beam, with a  $\cos^2$

distribution, that is further collimated by passing through two conical skimmers, before deposition of aerosol droplets on the sample substrate, positioned at a distance of 20 cm from the nozzle. The differential pumping stages are needed to connect the aerosol 970 Torr N<sub>2</sub> source to the UHV system while maintaining the necessary vacuum conditions.

The initial testing of the source involved characterizing the aerosol-free jet. The pulsed valve and its preceding components were attached directly to a diffusion pumped high vacuum system, and films were deposited on samples positioned at a same distance of 20 cm from the nozzle.

The system was first vacuum tested, and a fast ion gauge (Beam Dynamics) and an oscilloscope was used to determine the temporal characteristics of the free jet produced by expansion of the aerosol generated from a PCBM (0.5  $\mu\text{mol/mL}$  CHCl<sub>3</sub>) solution. The species PCBM is available in pure form (99 %, La Mer) and has known optical properties, providing a most convenient system for source characterization. The source flux was determined by deposition on a quartz substrate, followed by optical absorption spectrometry.

A film of PCBM was prepared by exposing a quartz (SiO<sub>2</sub>) substrate to 500 pulses of the aerosol (0.8 ms duration). The UV-Vis absorption spectrum, obtained by transmission through the film, is shown in Fig. 2.10.

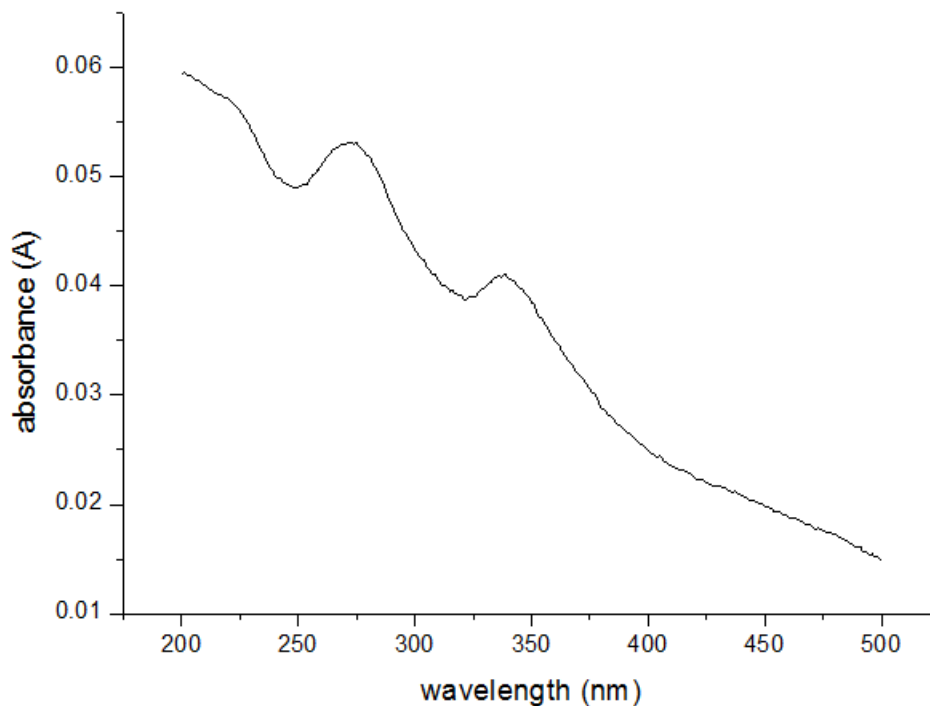


**Figure 2.10** The UV-VIS absorption spectrum of a PCBM film deposited on a SiO<sub>2</sub> substrate through 500 pulses of the aerosol free jet source (0.5  $\mu\text{mol/mL}$  CHCl<sub>3</sub>). The characteristic PCBM absorption band at 330 nm is used to calculate source flux.

PCBM absorbs strongly in the visible, with a maximum at 330 nm (absorption coefficient  $\epsilon = 6.4 \times 10^4 \times \text{L} \times \text{mol}^{-1} \times \text{cm}^{-1}$ ) that is here used for calibration purposes through adaptation of Beer's Law:

$$A = \epsilon c \ell \quad \text{Eq.2.5}$$

where A is the measured absorbance (unit-less), c is the solution concentration (mol/L), and  $\ell$  is path length (cm). In the present case involving transmission through a film, it is convenient to express Beer's law as:

$$A = \epsilon N_a \quad \text{Eq.2.6}$$

where  $N_a$  is the number of adsorbed PCBM molecules per unit surface area. Here we set  $N_a$  in unit of  $\text{mol}/\text{cm}^2$  since our sample surface is almost  $1\text{cm}^2$ . Based upon the known value for  $\epsilon = 6.4 \times 10^4 \times \text{L} \times \text{mol}^{-1} \times \text{cm}^{-1}$  and the measured 0.040 absorbance

value, we determine that 500 pulses yield a surface coverage of 3.89 molecules/nm<sup>2</sup>. Based upon the known 2D packing density of PCBM molecules in the solid state (1.04 molecules/nm<sup>2</sup>), this corresponds to PCBM coverage of 3.74 monolayer (ML) equivalents. The PCBM flux is thus determined to be 0.75% ML/pulse. We further note each droplet with a 1  $\mu$ m nominal diameter will contain  $3.9 \times 10^5$  PCBM molecules. We thus estimate that each pulse delivers  $\sim 2 \times 10^6$  droplets to the surface.

## Chapter 3 Single Component Self-Assembly on Metal Surfaces

As an introduction to the structural and electronic properties of binary systems, I will first describe single component films on Au (111) and Ag (111). The ZnPc and TN-ZnPc studies have been published in the Journal of Vacuum Science & Technology A (L. Tskipuri, Q. Shao, J. Reutt-Robey, *Solvent-assisted growth of metal phthalocyanines thin films on Au (111)*, Journal of Vacuum Science & Technology A 2012, **30**: 031402). The C<sub>60</sub>-PCBM studies have been published in the Journal of Physical Chemistry C (L. Tskipuri, Q. Shao, and J. Reutt-Robey, *Molecular ordering in PCBM-Au(111) interface formation*, Journal of Physical Chemistry C **116** (41), 21874 (2012) ). In these collaborative efforts, I contributed to the experimental design, experimental measurements, data acquisition and analysis, and interpretation. These two single component thin film studies provide substantial background for the whole thesis work.

### 3.1 Solvent-Assisted Growth of Metal Phthalocyanine Thin Films on Au (111)

#### 3.1.1 Introduction

New applications of organic molecules and nanoparticles in flexible electronics and photovoltaic technologies have spurred interest in improved methods for controlled materials deposition from the liquid state. Deposition techniques based upon directed flow of aerosols have recently been reported that offer materials versatility, relatively low cost, and large-scale manufacturing capacity.<sup>41</sup> In the aerosol deposition method, thin films are formed spraying a growth substrate with small droplets of solution. Through controlled droplet size, composition and flux, film deposition with

submonolayer precision can be realized.<sup>28,42</sup> Aerosol spray deposited organic photovoltaic cells and organic thin film transistors have been fabricated with demonstrated performances comparable to those of spin-cast cells.<sup>43,44,45,46</sup> Substantial efforts have been directed toward further device improvement through optimization of solvent spray deposition parameters. Solvent removal is critical for controlled surface topography and morphology, and molecular-level studies of solvent incorporation and removal from aerosol-deposited films are needed. In this section, we present investigations of molecular-beam aerosol deposition of metal phthalocyanine (MPc) films with in situ structural analysis via UHV-STM. MPcs are highly amenable to molecularly resolved imaging with STM, particularly in monolayers on gold and other transition metals with their molecular plane parallel to the metallic surfaces,<sup>47,48,49,50,51,52,53,54</sup> facilitating detailed analysis. For films prepared by PVD, surface mass transport is commonly increased by elevating the temperature of the growth substrate. For solution-deposited organic films, “solvent annealing” methods are increasingly employed in device applications to enhance mass transfer.<sup>55</sup> In this present section, we examine the effect of aerosol solvation on molecular-level film structure in the monolayer regime, revealing the impact of solvent on MPc surface mobility.

### **3.1.2 Experimental methods**

All experiments were conducted in the UHV-STM system with the liquid  $\mu$ aerosol molecular beam source, as illustrated in Chapter 2. Single crystal Au (111) substrates were first prepared with sputter-anneal cycles. Prepared substrates were then transferred under UHV for aerosol spray deposition utilizing solutions summarized in



Table 3.1. For prolonged pulse trains (1000 pulses), pressure in the load-lock compartment reached  $1 \times 10^{-6}$  Torr, rapidly decreasing to  $< 5 \times 10^{-8}$  Torr following the last valve closure. For the 0.5 mmol/L solution concentrations employed in this study, MPc coverages of 0.75% monolayer (ML)/pulse were deposited. These experimental procedures are typical for all experiments in this thesis work.

### 3.1.3 Results and discussion

Structural characteristics of films produced were measured with constant current imaging. All STM images were recorded at positive sample biases (0.65–0.85 V) and low tunneling currents (21–45 pA), for which no damage from the tunneling current was observed. Images were obtained at 27 °C within 30 min of film deposition and accumulated for up to 12 h after deposition. At the lowest coverages ( $< 0.05$  ML, data not shown) films consist of MPc islands decorating step edges and isolated MPc islands on extended terraces. Similar structural features are observed for both ZnPc and TN–ZnPc films for all studied solvents, indicating large diffusion lengths in this low-coverage regime. Increasing TN–ZnPc exposure to 0.4 ML produces a dense pattern of islands. As shown in Fig. 3.1a, islands are irregular molecular aggregates with an apparent height of 0.2 nm, as measured by STM topography. We note that flat lying MPc molecules, produced by PVD (physical vapor deposition), have apparent heights of just 0.1 nm.<sup>56</sup> Consequently, the aerosol-deposited TN–ZnPc molecules must have tilted orientations with respect to the substrate to account for the greater film height. Aerosol solvent variations in film structure are shown in Figs. 3.1a and 3.1b. Films prepared from a dichlorobenzene solvent (Fig. 3.1b) show a pronounced island registration to the  $(23 \times \sqrt{3}$ -herringbone)-Au (111) reconstruction, forming long

stripes on the surface with the molecules positioned at the tips of the herringbone. Such island registration to the substrate reconstruction indicates a thermodynamically favorable structure, showing that films grown from the dichlorobenzene solvent are grown closer to equilibrium than those deposited from the acetone solvent (Fig. 3.1a). The marked difference in TN–ZnPc island patterning from these two solvents is attributed to differences in solvent volatility. Under the present vacuum conditions, where solvent recondensation rates are negligible, solvent evaporation follows the Arrhenius rate law:

$$\frac{1}{n} \frac{dn}{dt} = A \exp \left( - \frac{\Delta H_{vap}}{RT} \right)$$

**TABLE 3.1** Solutions utilized for aerosol deposition.

Parameter	Solvent		
	Acetone	Toluene	<i>m</i> -Dichlorobenzene
Boiling point (°C)	56	111	180
$\Delta H_{vap}$ (kJ/mol)	31	37	52
ZnPc (mg/mL)	0.58	0.67	n/a
TN–ZnPc (mg/mL)	3.85	n/a	0.77

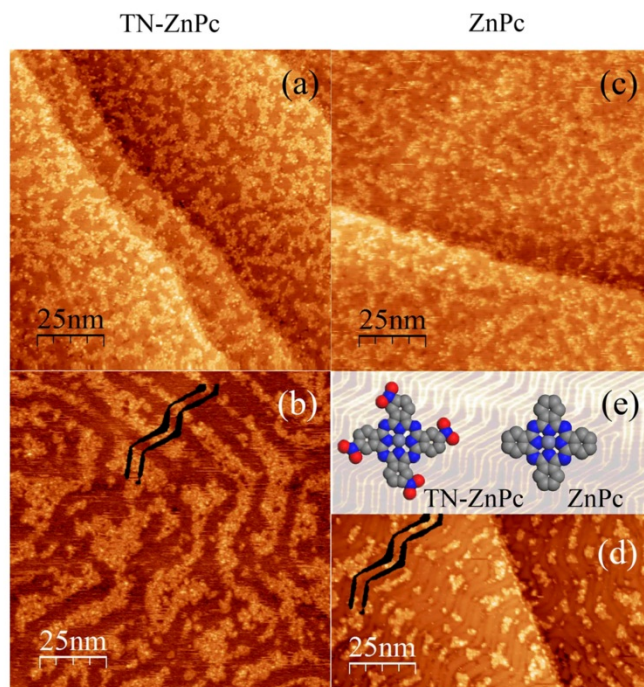


**Figure 3.1** Impact of aerosol solvent on patterning of MPc islands on Au (111) (0.4 ML coverage). UHV-STM images of as deposited films. Left: TN-ZnPc/Au(111) from (a) acetone and (b) dichlorobenzene; right: ZnPc/Au(111) from (c) acetone and (d) toluene (0.25 ML); (e) molecular models of TN-ZnPc and ZnPc.

where  $n$  is the number of solvent molecules,  $\Delta H_{\text{vap}}$  is the enthalpy of vaporization for bulk solvent, and  $A$  is the attempt frequency. With a value of  $\Delta H_{\text{vap}} = 52$  kJ/mol, *m*-dichlorobenzene has almost twice the enthalpy of vaporization as acetone.<sup>57</sup> The room temperature vaporization rate of dichlorobenzene is a factor of 104 times slower than that of acetone. Assuming the transition state theory  $10^{12} \text{ s}^{-1}$  value for  $A$ , droplets (1  $\mu\text{m}$  in diameter) of acetone evaporate within 1 ms of contacting the substrate, leaving the MPc solute to form a nearly random distribution of islands with a structure characteristic of diffusion-limited aggregation. Here we neglect spreading of the microdroplet and the possible residual partial monolayer of solvent, stabilized by solvent–substrate interactions, as reported for Au (111).<sup>58</sup> Droplets (1  $\mu\text{m}$  in diameter) of *m*-dichlorobenzene take much longer to evaporate (10 s vs 1 ms). The persistence

of a solvent film evidently assists the realization of thermodynamically favored MPc film structure. These results are accounted for with a growth scenario in which a solvent film enhances the surface mobility of the TN–ZnPc in the submonolayer regime, depositing TN–ZnPc islands at energetically favorable surface sites. To further demonstrate solvent impact on solute mobility, ZnPc films were prepared. STM images obtained for ZnPc deposited from acetone and toluene solvents are presented in Figs. 3.1c and 3.1d. For deposition from acetone, ZnPc film morphology is very similar to that of TN–ZnPc films grown under identical conditions, indicating that any intrinsic differences in ZnPc and TN–ZnPc mobilities at the Au (111)-vacuum interface, due to the electron-withdrawing NO<sub>2</sub> groups,<sup>59</sup> have a minor impact on morphology of aerosol deposited film. For the case of ZnPc films grown from the less-volatile toluene solution, ZnPc islands adopt the pattern of the Au (111) herringbone, reminiscent of TN–ZnPc in dichlorobenzene (Fig. 3.1d). This again illustrates that MPc surface mobility is enhanced by the persistence of a solvent layer that supports structure evolution. The stability of these submonolayer MPc islands is surprising, as a submonolayer of PVD-grown MPc molecules on metal surfaces has proven difficult to image at room temperature<sup>60,61</sup>. The different packing arrangement (tilt angle) and persistent solvent molecules, evidenced in the following, must stabilize submonolayer islands in aerosol-generated films.

Full monolayer MPc films, as prepared by aerosol deposition on room temperature substrates, exhibit nanoscale texture, as shown in Fig. 3.2a. Monolayer films of TN–ZnPc, as deposited from acetone, have 0.4 nm asperities, indicative of second-layer TN–ZnPc, and vacancy cavities. Such vacancy cavities are commonly observed in

aerosol deposition and are indicative of solvent expulsion and evaporation. The broad height distribution in monolayer films (Fig. 3.2c) is independent of solvent. This topographic spread indicates a distribution of TN–ZnPc orientations with respect to the surface normal and is attributed to competing MPc–Au and MPc–solvent interactions. Vacancy cavities of nominal 10 nm<sup>2</sup> dimension are routinely observed in as-grown films, independent of solvent employed. Such cavities are readily eliminated by mild annealing.

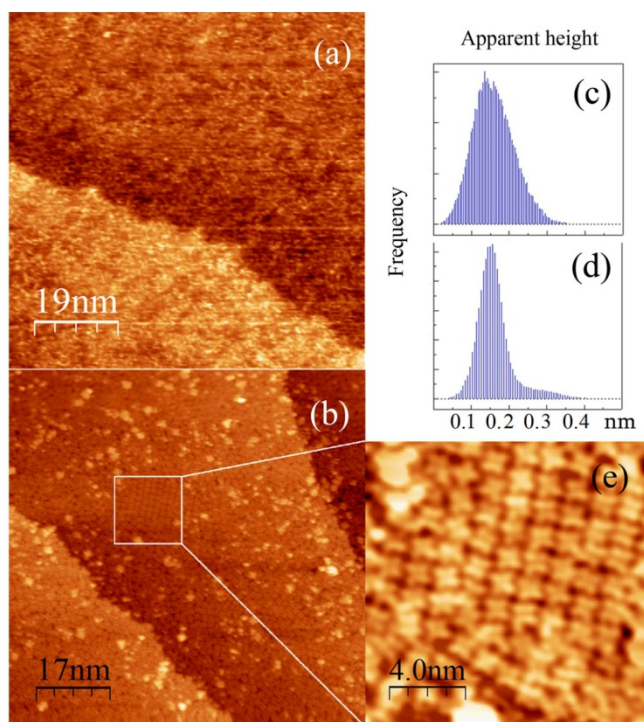


**Figure 3.2** Monolayer TN–ZnPc films deposited on Au (111) from acetone microaerosols. UHV-STM images of films as deposited on room temperature substrates (a) and following a 10 min 200 °C anneal (b); (c,d) corresponding height distribution histograms of as deposited (c) and thermally annealed (d) films; (e) molecularly resolved domain of TN–ZnPc film.

Aerosol-deposited TN–ZnPc monolayer films subject to 200 °C vacuum thermal annealing are shown in Fig. 3.2b. Resulting film order begins to approach that of PVD generated films. Topographic analysis of annealed films shows a sharp peak in

the height distribution histogram at 0.15 nm corresponding to the flat-lying monolayer of molecules, and a small shoulder at 0.3 nm corresponding to second-layer species (Fig. 3.2d). The staggered molecular arrangements of annealed monolayers reflect short range repulsion between the NO<sub>2</sub> ligands. Molecular orientation with respect to the substrate is more sharply defined in the annealed films, relative to the as-grown films. This effect is attributed to the complete removal of all solvent molecules, which impact short range MPc interactions and disrupt packing and orientation. The presence of multiple orientational domains (typical orientational domain size of 20 nm, see Fig. 3.2e) suggests that film order may be further improved through growth-temperature optimization.

Aerosol-deposited ZnPc monolayer films subject to 180 °C vacuum thermal annealing are shown in Figs. 3.3a and 3.3b. This treatment produces a first-layer of ZnPc with a narrow height distribution (Fig. 3.3c) in a nearly random 2D molecular arrangement with small bilayer islands. The density and orientation of first-layer ZnPc indicates complete solvent removal. The random 2D arrangement of first-layer ZnPc is consistent with previous reports of ZnPc films grown by PVD on Au (111), which find weak adsorbate–substrate interactions<sup>62,63</sup> and a persistent herringbone reconstruction of the gold substrate under the ZnPc monolayer.<sup>64</sup> Weak ZnPc–ZnPc interactions for flat-lying molecules are insufficient to drive 2D ordering on Au (111), unlike the TN–ZnPc films, where ligand-dominated intermolecular repulsion induces 2D ordering. In the as-deposited aerosol films, the solvent has a strong impact on film morphology for both ZnPc and TN–ZnPc. Upon thermal annealing, as for PVD-

deposited materials, film ordering is dictated by adsorbate–substrate and adsorbate–adsorbate interactions.

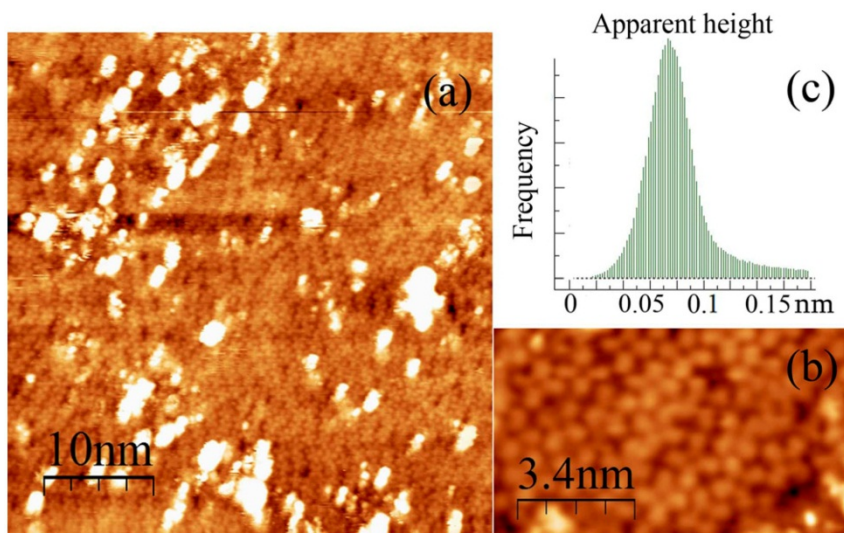


**Figure 3.3** Monolayer ZnPc film deposited on Au (111) from chloroform microaerosols. (a) UHV-STM image of film deposited on room temperature substrate followed by a 10 min 180 °C anneal; (b) molecularly resolved image of ZnPc film; (c) corresponding height distribution histogram of thermally annealed film.

### 3.1.4 Summary

In conclusion, ZnPc and TN–ZnPc films deposited on Au (111) at room temperature from aerosol microdroplets produce deposition patterns that reflect the volatility of the microaerosol solvent. At submonolayer coverages, island registration to the substrate herringbone is obtained for deposition from low-volatility aromatic solvents indicating solvent-enhanced surface transport. As deposited monolayer films show a broad height distribution, independent of solvent, indicating tilted MPc molecules with nonuniform packing. Post deposition thermal treatment produces monolayer films with uniform flat-lying surface orientations and in the case of TN–ZnPc packing order comparable to PVD grown films. Thermally annealed ZnPc films are more randomly ordered in 2D reflecting weaker interactions. Further tuning of aerosol-

generated film structure should be possible through controlled substrate temperature under deposition.

### **3.2 Molecular ordering in C<sub>60</sub>-PCBM thin films**

#### **3.2.1 Introduction**

Aerosol spray-deposited organic thin film transistors (OTFTs) and organic photovoltaic cells have been fabricated with demonstrated efficiencies comparable to those of spin-cast cells.<sup>43,44,65,66,67,45,46</sup> While a large number of papers have focused on the optoelectronic properties of such devices, molecular organization in films produced by such far-from-equilibrium growth conditions are poorly understood. Device performance is known to depend strongly on the molecular arrangement in the active layer, which sets the ability to carry charge.<sup>68,69</sup> Greater knowledge of molecular ordering is important for the advancement of organic electronic technologies and is needed to provide fundamental insight on far-from-equilibrium crystallization processes.

In the present section, we examine molecular ordering in films of C<sub>60</sub>-PCBM grown by the  $\mu$  aerosol deposition method. This functionalization introduces highly anisotropic PCBM–PCBM interactions and leads to the solvated crystals that have been reported<sup>69</sup>. A layered crystal structure of fullerene moieties, separated by sheets of the addends and an equivalent number of solvent molecules, was crystallized from dichlorobenzene. A monoclinic crystal structure with two disordered solvent molecules for each PCBM was grown from the solvent chlorobenzene. More recently, a novel dip-coating procedure yielded single crystals of PCBM with hexagonal symmetry from chloroform solvents.<sup>70</sup>



Investigations of vapor-deposited PCBM monolayers on Au (111)<sup>71,72,73</sup> report dramatically different PCBM packing arrangements than observed for the parent fullerene. Neat C<sub>60</sub> adopts a 2D hexagonal monolayer structure on gold and other transition metal surfaces,<sup>74,75,76</sup> with a nearest neighbor spacing of 1.02 nm, nearly identical to that in the bulk crystal. Reported PCBM arrangements on Au (111), in contrast, involve double rows of paired fullerene moieties spaced by the butyric acid methyl ester addends, oriented for hydrogen-bond formation. DFT theoretical computations demonstrated the stability of PCBM hydrogen-bonding motifs and predicted additional PCBM chain phases of comparable energy. In PVD generated films, PCBM arrangements are of much lower density than known fullerene monolayer phases and PCBM bulk crystal planes.

These studies, and the anisotropy of PCBM, suggest that further structural tuning of the PCBM crystalline phases should be possible. 2D hexagonal monolayers of PCBM, free of molecular solvent, should be accessible through control of film growth parameters. Additional PCBM polymorphs, arising from the predicted PCBM–PCBM hydrogen-bonding interactions, should be accessible. Investigations of structure formation in PCBM films as a function of key growth parameters are needed to expand our knowledge of PCBM–PCBM and PCBM–surface interactions and provide general insight into structure evolution for such high-cohesivity molecular films.

In this section we present investigations of the structure evolution in PCBM films, prepared by the novel microaerosol molecular-beam deposition method. The fine metering of this UHV-compatible deposition source bridges solution and physical

vapor deposition methods. PCBM monolayer phases are formed from select solvents, and molecular-level packing arrangements are monitored in situ via UHV-STM. Newly observed packing arrangements include new chain-phase and 2D hexagonal structures. Kinetic bottlenecks to long-range ordering are found and interpreted by DFT computation.

### **3.2.2 Methods**

All experiments were conducted in the UHV-STM system with the integrated pulsed microaerosol molecular beam source, as previously described.<sup>77</sup> The pulsed microaerosol was generated from the 0.5 mmol/L solutions of PCBM (SES Research, 99%) in chloroform and 1,3-dichlorobenzene with the nitrogen carrier gas. Films were directly transferred to the UHV STM stage for structural characterization and measured with constant current STM imaging. All images were recorded with positive sample biases (0.65–0.85 V) and low tunneling currents (21–45 pA). Images were obtained at 27 °C within 30 min of film deposition and accumulated for up to 48 h after deposition. The Au (111) substrates used for this research were prepared with atomically-clean terraces with the characteristic herringbone reconstruction structure as described in section 2.2.2.

Gas-phase density functional theory (DFT) calculations were carried out using the Dmol<sup>3</sup> package.<sup>78,79</sup> The Perdew–Burke–Ernzerhof (PBE)<sup>80,81,82</sup> functional was used for exchange and correlation.

### 3.2.3 Results

#### Submonolayer PCBM Film

Submonolayer PCBM films, directly grown from pulsed microaerosol deposition, were first examined. Low coverage (0.1– 0.2 monolayer (ML)) films grown from both chloroform and dichlorobenzene solutions on Au (111) (Figure 3.4 a, c) have a random distribution of PCBM islands, with no apparent registration to the underlying gold herringbone reconstruction. Increasing PCBM exposure to 0.5 ML (Figure 3.4 b,d) creates a more dense pattern of irregular molecular aggregates. In the “dark” PCBM-free regions of the 0.5 ML films, topographic variations suggest the presence of solvent molecules even under UHV conditions.

Solvent inclusion in the films is next tested. Low coverage (0.1 ML) PCBM films grown from chloroform solution and subject to thermal annealing are shown in Figure 3.5. After a 10 min 120 °C anneal, molecular islands with two height levels are observed. The bright protrusions are due to PCBM, and the additional layer structure is attributed to the chloroform solvent. This structure is very temperature responsive: After annealing at 160 °C for 10 min, the “pools” of solvent are reduced and encircled with PCBM (Figure 3.5 b). Annealing to 185 °C eliminates such solvent “pools”, with only PCBM cluster aggregates (Figure 3.5 c) remaining. The cluster aggregates appear to be loosely packed with PCBM molecules and are completely stable with respect to room temperature STM imaging (Figure 3.5 c,d). This amenability to room temperature

STM imaging is atypical for small clusters on extended terraces (Figure 3.5 c,d), suggesting that stabilizing solvent molecules may yet be contained in the aggregates.

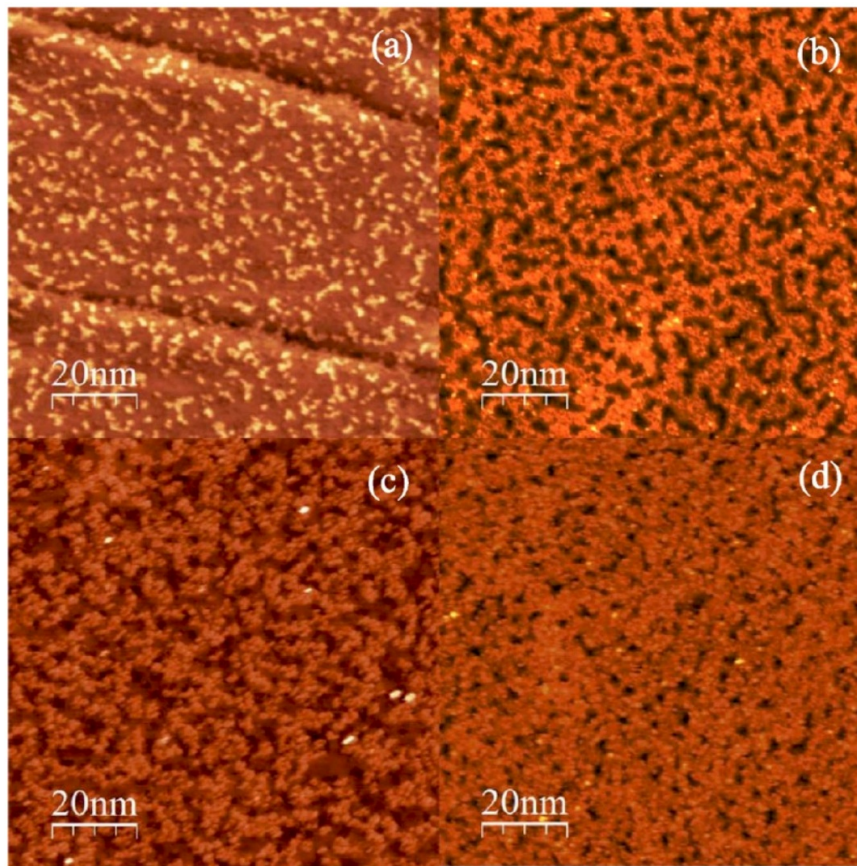


**Figure 3.4** UHV-STM images of submonolayer PCBM films deposited from microaerosol solvents on Au(111) at 300 K: (a) 0.1 ML PCBM/chloroform; (b) 0.5 ML PCBM/chloroform; (c) 0.15 ML PCBM/dichlorobenzene; (d) 0.5 ML PCBM/dichlorobenzene.

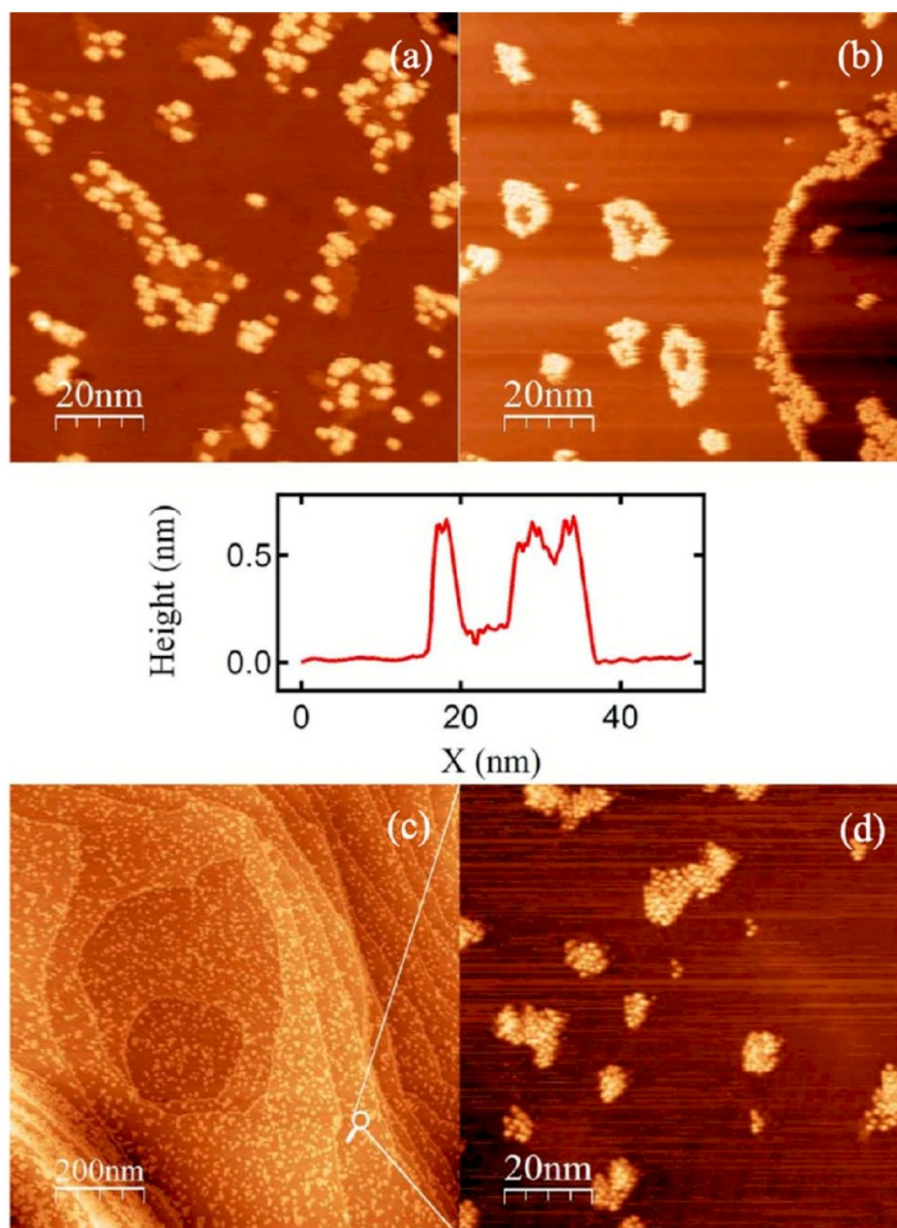


**Figure 3.5** 0.1 ML PCBM films deposited on Au (111) from chloroform microaerosols. UHV-STM images of PCBM islands following (a) flash anneal to 180 °C and (b) 15 min 160 °C anneal. Line profile indicates residual solvent (0.2 nm height) inside such PCBM island (not shown in (a, b)) with 0.6 nm asperities; (c, d) 15 min anneal at 185 °C shown with two magnification.

With increasing coverage to 0.4 ML and thermal annealing PCBM islands grow along the Au (111) crystallographic directions, forming triangular domain networks upon temperature elevation, as shown in Figure 3.6 a. Direct inspection of the

molecular packing of such a film after annealing to 185 °C (Figure 3.6 b), and the absence of diffraction features in the Fourier-transformed images, reveal no apparent long-range order in the PCBM packing. Upon doubling the coverage to 0.8 ML, the film wets the surface and is punctuated with vacancy voids (Figure 3.6 c). The formation and coalescence of small vacancy islands in this temperature window is indicative of an ongoing thermally activated process of solvent expulsion from the PCBM layer. Closer inspection of the PCBM layer with STM reveals the onset of short-range ordering of PCBM molecules into double-row structures, as indicated by black arrows on Figure 3.6 d. These short (<10 nm) PCBM chains are in registration with the substrate and do not lengthen appreciably upon further annealing.

### **Monolayer PCBM Films**

Monolayer PCBM films, in which the surface is completely covered by a single layer of PCBM molecules, were prepared by deposition from both chloroform and dichlorobenzene solutions. The density of such monolayer films could be varied between 0.8 and 1.0 molecules/nm<sup>2</sup> by PCBM exposure. Further PCBM deposition leads to multilayer formation.

Figure 3.7 a,b shows a monolayer film with a PCBM density of 0.86 molecules/nm<sup>2</sup>. The monolayer is a loosely packed arrangement of PCBM without long-range order. Such glassy films are structurally similar to those produced by physical vapor deposition<sup>83,72,73</sup>. Thermal annealing (180 °C, 30 min) produced no apparent change in the molecular ordering.

A denser monolayer film (1 molecule/nm<sup>2</sup>) is shown in Figure 3.7 c. This increased PCBM density produces two distinct monolayer phases: crystalline PCBM islands in

coexistence with a disordered film phase. These PCBM islands, as shown under magnification in Figure 3.7 d, are a 2D hexagonal arrangement of PCBM molecules with a 0.98 nm nearest-neighbor separation. The PCBM separation is 4% less than the 1.02 nm nearest-neighbor separation for 2D hexagonal C<sub>60</sub> on Au (111).<sup>74,75,76</sup> PCBM island sizes up to 10 – 25 nm are observed in film grown on the room temperature substrate. Extended film anneals at temperatures up to 250 °C yielded no significant change in the 2D hexagonal PCBM island sizes or shapes.

### **Particulate PCBM Deposition**

The impact of a PCBM surface density gradient on film structure evolution was next explored. A liquid suspension with micrometer-sized PCBM particulates in a saturated solution was created by ultrasonication of a 5 mmol/L solution of PCBM in chloroform. Isolated particulates of PCBM could thus be deposited on the surface together with a submonolayer PCBM film, as shown in Figure 3.8 a. The boundary between the PCBM particle (height = 50 nm) and the submonolayer PCBM film imposes a chemical potential. Upon annealing to 185 °C for 15 min, long, double row PCBM structures appear on the now solvent-free Au (111) terraces (Figure 3.8 b). The initial PCBM particulate height undergoes reduction during the process, confirming material flow on the surface. The double-row structures are most dense near the PCBM particulate, winding toward the lower-density Au (111) surface, in direct response to the surface chemical potential. Two distinct double-row structures are shown in Figure 3.8 c,d: a zigzag pattern (c), with a unit cell angle of 55°, and a head-to-head pattern (d), with a unit cell angle of 90°. (The unit cell angle corresponds to the fullerene offset on adjacent chains.) Both structures register to Au



(111), and three  $120^\circ$ -rotated orientational domains (not shown) can be found for each structure. Away from the PCBM mound, chain segments of differing orientations join together to create winding structures. PCBM molecules at chain joints have a higher PCBM coordination (three nearest neighbors) than straight PCBM chains (two nearest neighbors).

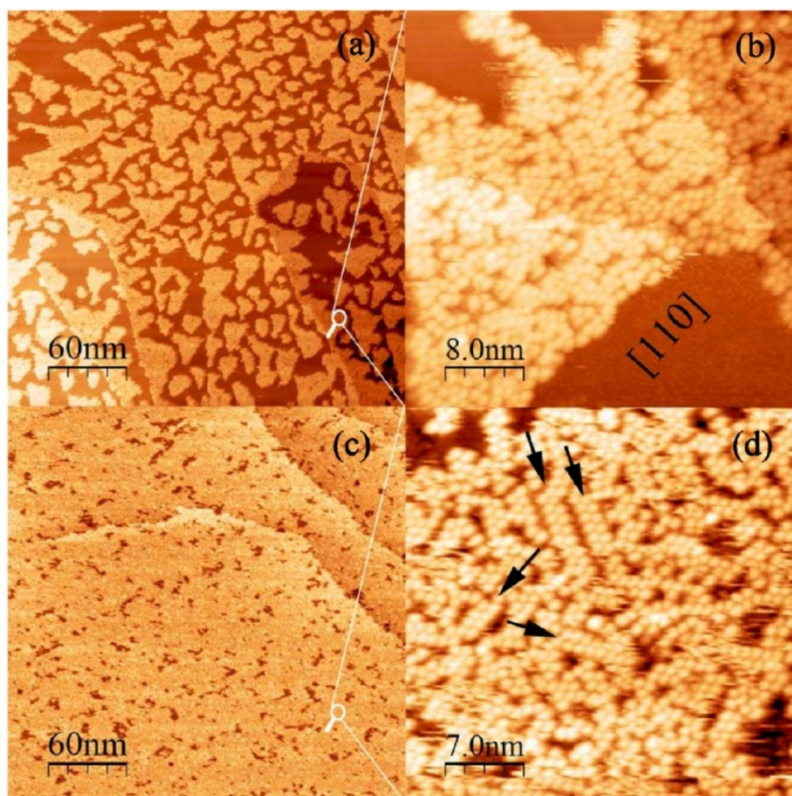


**Figure 3.6** Submonolayer PCBM films deposited on Au (111) from chloroform microaerosols. UHV-STM images shown with two magnification: (a, b) 0.4 ML film after a 20 min 230 °C anneal; (c, d) 0.8 ML film after a 15 min 130 °C anneal. Arrows indicate doublerow structures.

### 3.2.4 Discussion

Microaerosol deposition of PCBM films clearly involves a very-far-from-equilibrium growth dynamic. Glassy molecular films are produced by deposition on



room temperature substrates, with thermal annealing needed to induce PCBM ordering.

Emerging structural patterns depend sensitively on the surface density of PCBM. At lower PCBM densities, two distinct double-row structures emerge. Short segments of both double-row structures follow deposition from homogeneous solutions.

Domains of both double-row structures follow deposition from PCBM solution suspensions at particulate-submonolayer boundary regions. At intermediate PCBM film densities, the PCBM films remain disordered even upon thermal annealing.

At a molecular film density of 1 molecule/nm<sup>2</sup>, however, the films break into ordered 2D hexagonal domains and disordered PCBM regions. A schematic “processing phase diagram” of the accessible PCBM film structures as a function of the temperature and coverage growth parameters is presented in Figure 3.9.

The molecular model for double-row self-assembly is based upon the van der Waals interactions between neighboring fullerene moieties and hydrogen-bonding interactions that involve the butyric acid methyl ester group. Several potential dimer and tetramer structures with comparable energies have been identified by DFT calculations, distinguishable by the offset arrangement (i.e., unit cell angle) of adjacent fullerene chains. In the PVD-generated films, only the head-to-head PCBM chain structures were reported. In the present study, we sampled a different growth space, PCBM tetramer geometries with both large and small values of the  $\theta$ -tetrameral

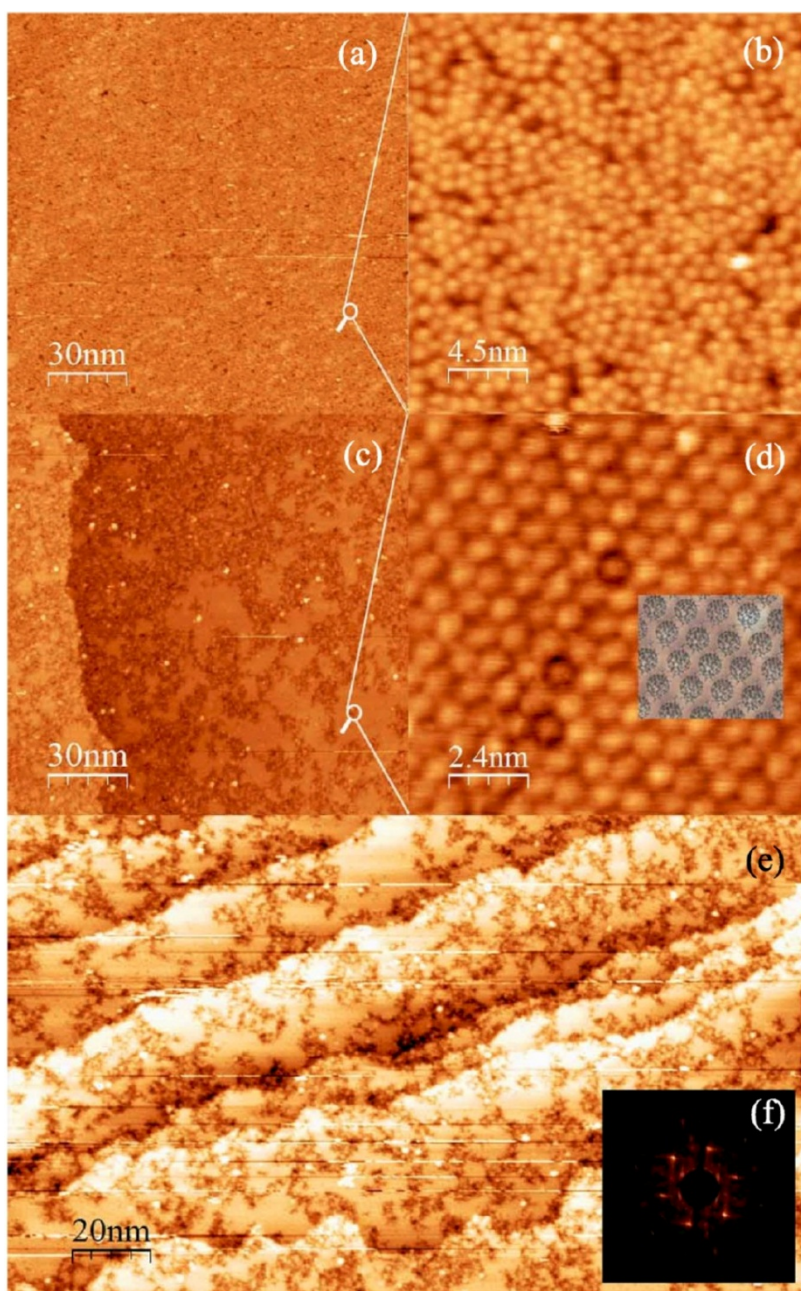


**Figure 3.7** Density-dependent structures in PCBM monolayer films: (a, b) Lower density ( $0.86 \text{ molecules/nm}^2$ ) PCBM monolayer after 10 min  $200^\circ\text{C}$  anneal. Magnified image shows disordered structure. (c) Higher density ( $1 \text{ molecules/nm}^2$ ) PCBM film shows coexisting phases. (d) Ordered 2D hexagonal structure domain with insert packing model. (e) Large scale PCBM monolayer with 2D hexagonal domains. (f) fast Fourier transform pattern of 2D hexagonal structure of the same film domain yields the  $0.98 \text{ nm}$  unit cell.

unit cell angle are found. Two different arrangements of PCBM double-rows are shown in Figure 3.8 c (zigzag pattern with  $\theta \approx 55^\circ$ ) and Figure 3.8 d (head-to-head pattern with  $\theta \approx 90^\circ$ ). The observation of multiple chain orientations in the solution grown films is not surprising, given the comparable energies of the dimer and tetramer structures, which vary by just a few kcal/mol.<sup>84</sup> Chain formation is most sensitive to local PCBM density and is enhanced (for particulate depositions) by thermal annealing. For films deposited from homogeneous solutions, the PCBM packing density within the chains ( $\sim 0.79$  molecules/nm<sup>2</sup>) is lower than the average PCBM film density. Chain formation thus raises the PCBM density in the surrounding region, suppressing further chain formation. This explains why domains of the chain phase do not form from homogeneous solution. More facile chain formation occurs upon deposition from heterogeneous solutions. Evidently, a PCBM reservoir (mound) and a low-density PCBM region create a favorable condition for thermally activated chain growth.

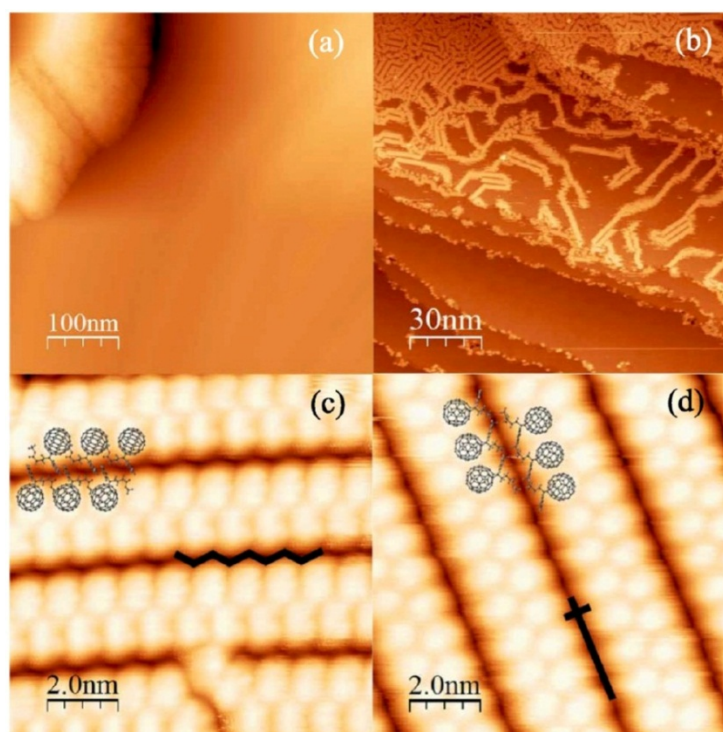


**Figure 3.8** UHV-STM images of PCBM film deposited on Au(111) from chloroform microaerosols: (a) as-deposited on room temperature substrate, (b) followed by a 10 min 180 °C anneal, (c, d) double-row molecular structures observed in surface regions near the PCBM particle. Initial PCBM particulate height is greatly reduced.

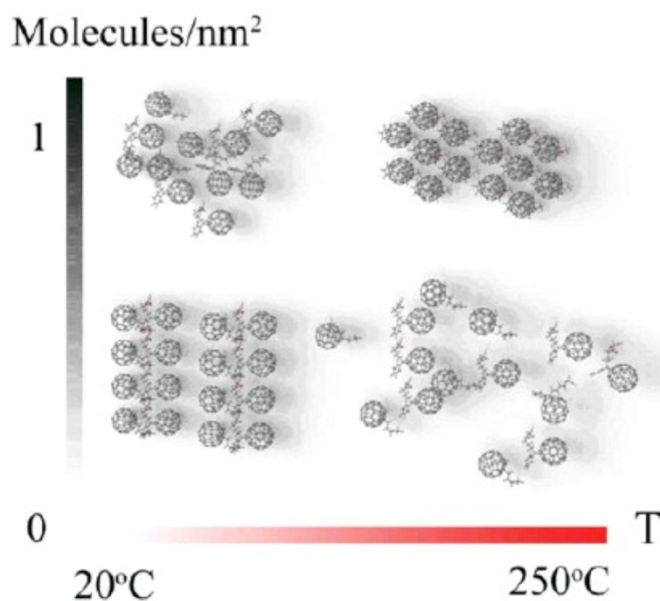


**Figure 3.9** “Processing phase diagram” depicts accessible PCBM structures from chloroform microaerosols as a function of surface coverage and anneal temperature.

The 2D hexagonal PCBM monolayer phase, in contrast, is the densest phase. Nucleation and growth of 2D hexagonal domains will thus reduce the PCBM density in the surrounding region. The PCBM films show a density-dependent transition from a disordered glassy phase to the 2D hexagonal structure. Islands of 2D hexagonal PCBM are self-limiting to 10–25 nm dimension. The 2D hexagonal PCBM islands closely resemble those of C<sub>60</sub>, albeit with a 4% reduced lattice constant, more limited domain size, and irregular shape. The possibility of hexagonal order was described in previous studies<sup>69,70</sup> and a theoretical model was proposed for layered PCBM hexagonal packing arrangement with  $a = 0.97$  nm (in-plane) and  $c = 1.26$  nm (interlayer) distances, respectively.<sup>85</sup>

The growth of 2D hexagonal PCBM domains requires thermal activation. This indicates a kinetic barrier to reorient the phenyl and ester groups from the more random orientations of the disordered phase to an upright configuration needed for close packing. We have used DFT calculations to explore the orientational dependence of PCBM reorienting. Specifically, we computed the orientation dependence of PCBM dimer energies as a function of PCBM separation. Figure 3.10 shows the total

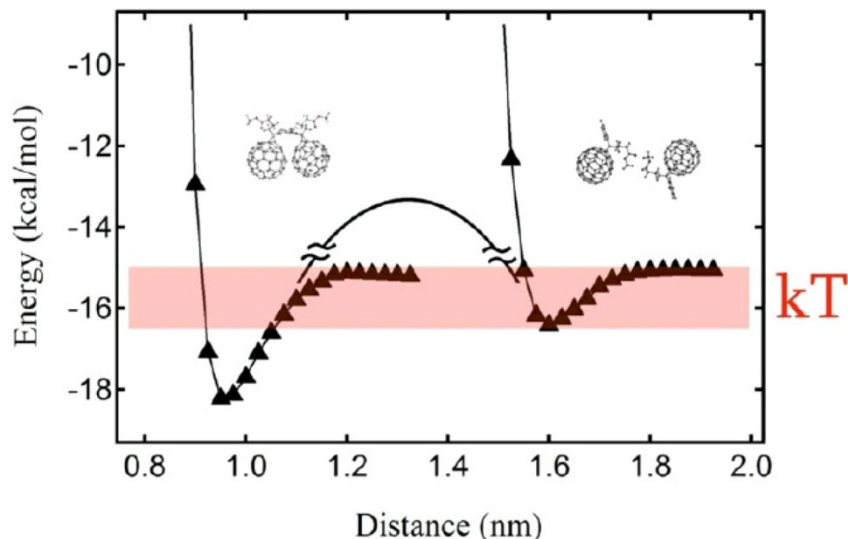


**Figure 3.10** Energies of PCBM dimers in a “standing-up” orientation (left) and a “lying-down” orientation (right), computed by DFT as a function of intermolecular distance. Diamonds represent calculated values. Solid black line depicts an energy barrier for reorientation from a lying-down to a standing-up structure. Shaded region shows available thermal energy under experimental conditions.

energies of PCBM dimers computed for “standing-up” and “flat-lying” orientations as a function of intermolecular distance. In the flat-lying configuration (right) a potential well of 1.3 kcal is found at a separation of 1.6 nm, corresponding to the attraction of the phenyl ester groups. Further compression of the PCBM in this “flat-lying” orientation leads to a sharp increase in energy. For the “standing-up” orientation (left) a deeper well of 3 kcal/mol is found at a PCBM distance of ~10 nm. The hexagonal PCBM film consists of all “standing-up” PCBM molecules. Production of the 2D hexagonal phase involves a reorientation of the functional groups from other orientations. This change in orientation must have a kinetic barrier, as illustrated schematically in Figure 3.10. Annealing temperatures of 200 °C drive the formation of the 2D hexagonal PCBM phase, suggesting an activation energy greater than 1 kcal/mol thermal energy. The actual barrier will, of course, depend upon interaction

between the substrate and van der Waals interaction between PCBM and cannot be determined from this simple calculation.

A characteristic feature of the 2D hexagonal PCBM islands, shown in Figure 3.7 c,e, is their extended shapes. Islands as long as 100 nm are produced, but compact (round) islands of this dimension never arise, even after annealing. Significantly, 2D hexagonal PCBM islands coexist with the disordered PCBM phase, and island shapes reflect the interfacial energies between these two distinct PCBM phases. The extended 2D hexagonal PCBM island shapes indicate low interfacial energies between the 2D hexagonal PCBM domains and the surrounding disordered PCBM phase. Indeed, low domain boundary energy is expected from attractive PCBM interactions along this boundary: PCBM molecules at the 2D hexagonal island boundary (unlike those in the island interior) can reorient the addends and interact attractively with PCBM neighbors in the surrounding disordered phase.

Finally, we comment on the somewhat unexpected ease of imaging submonolayer fullerene films with UHV STM. We note that residual solvent molecules<sup>77,58</sup> stabilized by solvent–substrate interactions can restrict the surface diffusion of deposited PCBM to the point where stable STM imaging at room temperature becomes possible. This contrasts with STM measurements on submonolayer PCBM films prepared by PVD, where the room formation of a 2D gas precludes room temperature STM measurements.<sup>60,61</sup> In the present experiment, even after solvent removal by thermal annealing, PCBM islands can be molecularly imaged, for sufficiently mild tunneling conditions, where the tunnel gap resistance is  $>1\text{ G}\Omega$ .

### 3.2.5 Summary

We have investigated structure evolution in solution processed PCBM films on Au (111). Molecular organization was monitored from disordered structures of variable density through distinctive arrangements, driven by thermal annealing. Double-row structures, involving two distinct PCBM hydrogen bonding arrangements, were observed: a head-to-head chain arrangement, as reported for PVD films, and a zigzag arrangement with offset PCBM. The formation and coexistence of both double-row patterns is consistent with theoretical predictions of these structure motifs, which have near equivalent energies. The PCBM surface density needed to nucleate double-row structures in microaerosol-deposited films exceeds the density of an ordered PCBM chain domain.

Consequently, only short segments and small domains of the double-row structure are formed. At intermediate coverages ( $0.6\text{--}0.9$  molecules/nm<sup>2</sup>), only disordered PCBM films are formed. At a higher PCBM density of 1 molecule/nm<sup>2</sup>, the PCBM monolayer film phase separates into crystalline 2D hexagonal monolayer islands and a disordered PCBM monolayer phase. The nearest-neighbor PCBM spacing in 2D hexagonal islands agrees well with structure predictions and is 4% compressed from the corresponding 2D hexagonal structure for C<sub>60</sub>. The 2D hexagonal PCBM islands have irregular and somewhat ramified shapes, indicating low domain boundary energy. This reflects attraction between perimeter 2D hexagonal PCBM molecules and neighboring PCBM in the disordered phase.

The phenyl ester groups needed for solution processability create kinetic challenges for molecular ordering. A relatively high temperature (177°C) is required to generate



2D hexagonal islands in the dense, but glassy, PCBM monolayer film. The kinetic barrier for 2D hexagonal PCBM formation reflects the energy cost for reorienting PCBM from the random adsorption geometry of the deposited phase to the standing-up geometry required for an 2D hexagonal structure with a unit cell of just 0.98 nm. Orientation dependent PCBM–PCBM interactions are significant and stabilize a disordered monolayer with thermal energy needed to drive 2D hexagonal island formation. The short 0.98 nm unit cell length of the 2D hexagonal PCBM structure indicates attractive interaction between the phenyl ester addends in this standing up configuration, as supported by dimer calculations. Additional low-temperature STM measurements are needed to resolve the 2D hexagonal structure with submolecular resolution to obtain more precise information on the functional group arrangement in this 2D assembly.

## Chapter 4 Vertical Phase Separation in Bilayer C<sub>60</sub>-PCBM: ZnPc Films

We report a UHV-STM study of thermally driven interface rearrangement in binary films of C<sub>60</sub>-PCBM and ZnPc, a model electron acceptor-electron donor system for organic solar cells. Neat C<sub>60</sub>-PCBM films have been previously shown to undergo a transition from a disordered (glassy) phase to a crystalline 2D hexagonal arrangement above a critical packing density of 0.86 molecules/nm<sup>2</sup>. We now show how local PCBM density has a critical impact on binary film structure evolution. Bilayer films of C<sub>60</sub>-PCBM and ZnPc, undergo a spontaneous vertical phase separation to PCBM/ZnPc/Au (111) stacking at lower ( $< 0.86$  molecules/nm<sup>2</sup>) PCBM densities. This vertical phase separation is shown to be electrostatically preferred, with PCBM/ZnPc/Au (111) dimer stacking lower in energy by 0.16 eV/pair relative to ZnPc/PCBM/Au (111) stacking. At higher local PCBM densities, sufficient to nucleate 2D hexagonal PCBM domains, ZnPc molecules do not displace PCBM to the second layer. PCBM density variations in binary films thus give rise to a heterogeneous interface structures. This work have been published in the Journal of Physical Chemistry C (Q. Shao, L. Tskipuri, and J. Reutt-Robey, *Vertical Phase Separation in Bilayer [6,6]-Phenyl-C<sub>61</sub>-butyric Acid Methyl Ester:Zinc Phthalocyanine Films*, Journal of Physical Chemistry C(118), 2014, 18612). In the collaborative efforts, I contributed to the experimental design, experimental measurement, data acquisition, data analysis and interpretation.

## 4.1 Introduction

Pairings of electron-accepting fullerenes with electron-donating molecular semiconductors have received great scientific interest as model systems for organic photovoltaic devices<sup>86</sup>. As described in Chapter 1, optimization of interface structure in donor-acceptor heterojunctions for efficient charge separation and transport is sought to improve the overall performance of those photovoltaic devices<sup>87,88</sup>. A better understanding of the fundamental relationship between electronic properties and film morphologies on the nanoscale at charge-separating interfaces is needed. Here we report an investigation of molecular-level structure evolution in a binary system consist of PCBM and ZnPc, prepared by the microaerosol liquid deposition method. In previous work on single-component films of PCBM and ZnPc, we have shown how monolayer phase selection is controlled by the growth kinetics<sup>89</sup> and solvent choice<sup>77</sup>. Molecular-level characterization of interface structures produced from different kinetic regimes is crucial to understand and control how molecular interactions drive interfacial architecture.

Obtaining a greater molecular-level understanding of how donor and acceptor solutes adsorb, crystallize and separate is of fundamental interest and needed to advance liquid deposition technologies. In this present work, we used the liquid microaerosol deposition method to create uniform and gradient bilayer films of the binary PCBM-ZnPc on Au (111). We track thermally induced structure evolution from different initial film structures.

Our aim is to reveal the molecular partitioning and stacking, as driven by the relative strengths of molecule-molecule and molecule-substrate interactions. Table 4.1 provides the hierarchy of energetic interactions for this system.

Pair Interaction Energy (eV)		Adsorption Energy (eV)	
PCBM-PCBM	1.5 <sup>90</sup>	MPc/Au(111)	0.4 <sup>91</sup>
ZnPc-ZnPc	0.87 <sup>90</sup>	PCBM/Au(111)	1.2 <sup>92</sup>
ZnPc-PCBM	0.44 <sup>90</sup>		

**Table 4.1** Energetic interactions in the PCBM, ZnPc, and Au (111) system.

We briefly summarize the structural features of single-component films prepared by microaerosol deposition.<sup>77, 89</sup> Monolayers of PCBM on Au (111), deposited from chloroform solvent, exhibit distinct temperature- and density-dependent structures: At very low coverage, small domains of double-row structures, involving two distinct PCBM hydrogen-bonding arrangements, arise following thermal annealing up to 130 °C; at intermediate coverage (0.6 - 0.86 molecules/nm<sup>2</sup>), only disordered PCBM films are formed, even with thermal annealing; at higher (> 0.86 molecules/nm<sup>2</sup>) PCBM density and after annealing to 177 °C, crystalline 2D hexagonal monolayer islands of PCBM form with stand-up molecular orientation. Stable monolayers of ZnPc on Au (111), displaying a nearly square lattice phase and density of 0.55 molecules/nm<sup>2</sup>, are produced following annealing to 127 °C. Within this monolayer, ZnPc adopt flat-lying orientations with respect to Au (111).

We now build upon these previous works, investigating nanophase separation in binary mixtures and molecular orientation at the resulting donor-acceptor interfaces. We show how bilayer PCBM-ZnPc films prepared with two distinct initial film

structures transform to the layered structure motif in this present work. We show how this vertically phase-separated arrangement is thermodynamically favorable but require thermal activation. We further identify configurations from which this stacked structure is inaccessible. The results provide guidance for tailoring interface structures in molecular semiconductor mixtures.

## **4.2 Methods**

For the 0.5 mmol/L (of each solute) concentrations employed in this study, an average coverage of 0.75%ML monolayer equivalent/pulse was deposited. Films were directly transferred to the UHV-STM stage for in situ structural characterization and measured with constant current STM imaging. All images were recorded with positive sample biases (0.65 V - 0.85 V), low tunneling currents (21 - 45 pA), 512 line scans, and 512 points per line. All image analysis was performed with the program “WSxM”. This analysis involved first performing a planar background subtraction (average minimum plane) and subsequent height histogramming. For these height histograms, the x-axis is relative height and the y-axis is the number of counts in each relative height bin (bin size 0.01 nm).

The well-ordered Au (111) surfaces were generated by two cycles of Argon ion sputtering and subsequent annealing with atomically-clean terraces, as described in section 2.2.2.

Binary thin films were prepared with the following two protocols:

1. Co-deposition, where PCBM and ZnPc molecules were first mixed in chloroform with equimolar concentrations of 0.5 mmol/L and then deposited onto Au (111).
2. Sequential-deposition, where PCBM molecules were first deposited onto Au

(111) substrate from a 0.5 mmol/L chloroform solution and then ZnPc molecules were deposited onto the PCBM/Au (111) surface also from a 0.5 mmol/L chloroform solution.

Density functional theory (DFT) calculations were carried out for dimers using the Dmol<sup>3</sup> package<sup>79</sup>. The generalized gradient approximation and the GGA - DFT functional Perdew-Burke-Ernzerhof (PBE)<sup>80,81</sup> were used for exchange and correlation. All electron calculations were performed with the double numerical plus d-functions (DND) basis set and a real space cutoff of 0.53 nm.

### **4.3 Results and Discussion**

Measurements were conducted on films of bilayer thickness in order to explore interface formation and the possible vertical separation of solutes at the substrate.

#### **Codeposited Bilayers**

A bilayer film with equal parts PCBM and ZnPc was deposited from the aerosol mixture on the room temperature Au (111) surface, as described above. An STM image of the as-grown bilayer film is shown in Figure 4.1a. Film morphology consists primarily of an irregular network of molecular aggregates with no apparent registration to the underlying gold herringbone reconstruction. Aggregates are interconnected in a branched network. The branches have a relatively uniform width (4-5 nm) and a longer segment length on the order of 10 nm. In addition to the  $\sim 4.5 \times 10 \text{ nm}^2$  segments, we observe isolated aggregates of comparable size. Such aggregates are separated by distances on the order of 15 nm, suggesting a diffusion length of this length. The size of these aggregates,  $\sim 45 \text{ nm}^2$ , indicates that they contain on the order of 45 molecules (assuming each molecule occupies  $1 \text{ nm}^2$ ). The

total height variation is 0.15 nm (seen in Figure 4.1b, fwhm = full width at half-maximum), smaller than the STM-measured heights of monolayer PCBM films (0.4 nm) and ZnPc films (0.2 nm) in direct contact with the Au (111) substrate. The more shallow height variation in the mixed films indicates that the films are a disordered arrangement of PCBM, ZnPc and residual  $\text{CHCl}_3$ , as illustrated schematically in Figure 4.1c.

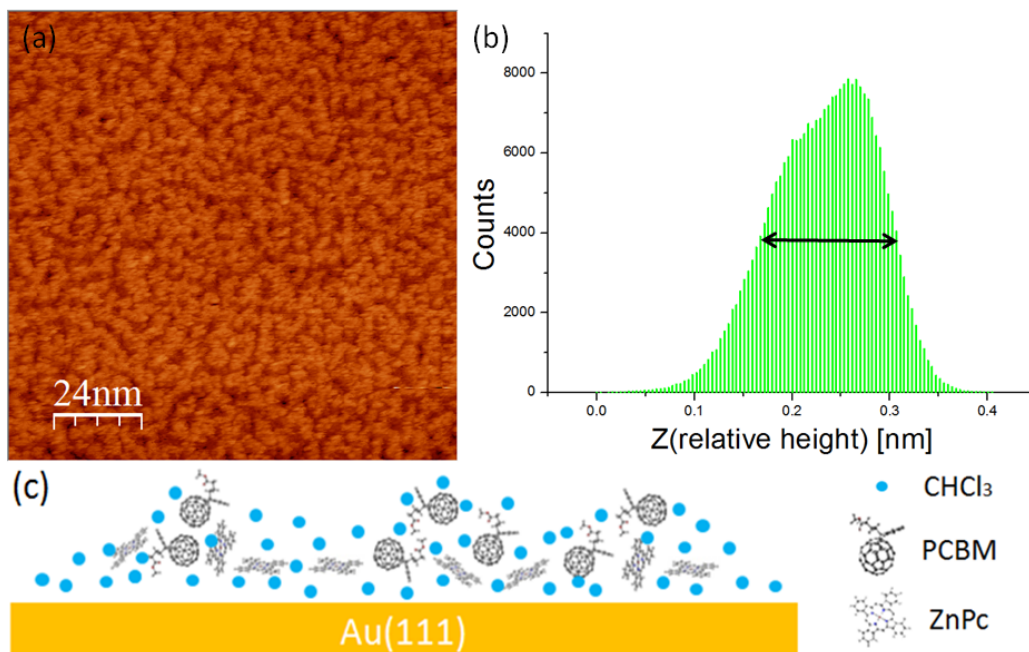


**Figure 4.1** Binary PCBM + ZnPc film codeposited from equimolar microaerosol chloroform solvent onto Au (111): (a) UHV-STM image,  $120 \times 120 \text{ nm}^2$ . (b) Corresponding height histogram with an arrow denoting  $\text{fwhm} = 0.15 \text{ nm}$ . The asymmetric histogram contains two modes, corresponding to the dark and light regions of the STM image. (c) Schematic illustration of as deposited film structure. Height variations are attributed to solvent-covered gold regions and to solute aggregates.

Previous studies of single-component aerosol-deposited films of both PCBM and ZnPc revealed solvent retention<sup>89</sup> at room temperature even under UHV conditions. Here we tested for solvent retention in mixed PCBM-ZnPc films by seeking to release solvent by step-wise annealing, as shown in Figure 4.2. Upon increasing temperature

to 80 °C (Figure 4.2 a) a change in film morphology is clearly observed. The pattern of uniformly spaced aggregates in the original film (Figure 4.1a) disappears and the film becomes rougher, with a height variation (fwhm of Figure 4.2c) of 0.4 nm (vs. 0.15 nm in direct deposited film). Upon further heating to 100 °C (Figure 4.2b), the contrast becomes much more pronounced due to a sharpening of the height distribution and the height variation reveals more obvious vertical phase separation, as shown in the histogram in Figure 4.2d. These asymmetric distributions can be fit to two and three modes, respectively, as shown in Appendix B. Changes in surface topography indicate that solvent molecules are driven from the film by 80°C.

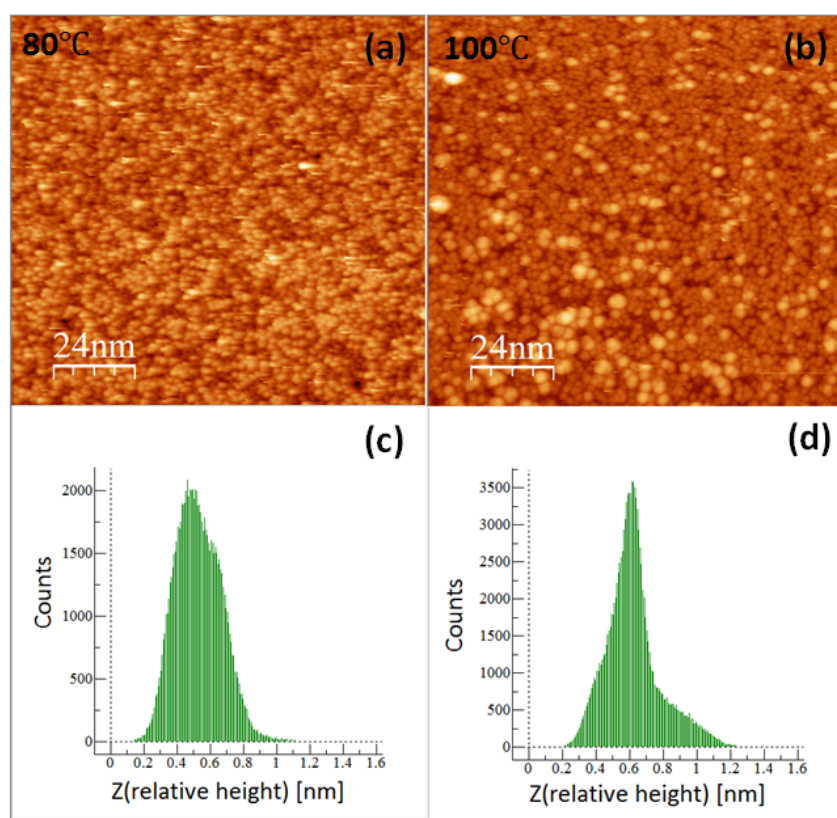


**Figure 4.2** STM images of binary films following stepwise annealing: (a) 80 °C anneal for 20 min. (b) 100 °C anneal for 20 min. (c) Height histogram of film a shows an increased spread in height distribution relative to unannealed films. (d) Height histogram of further annealed film b reveals three modes (See Appendix B for mode analysis).



Under stronger thermal activation, PCBM and ZnPc arrange into more ordered structures with evident vertical separation. Figure 4.3a shows a molecularly resolved image of a film after heating to 270 °C for 20 min. Bright spherical protrusions are PCBM molecules, and the dark layer under is comprised of ZnPc molecules. The corresponding height histogram, provided in Appendix B-3, reveals a 0.31 nm apparent height difference between the ZnPc monolayer and second layer PCBM. Figure 4.3b reveals highly ordered ZnPc molecules in direct contact and registration with Au (111). Similar ZnPc structures are observed and well-studied in PVD deposited ZnPc monolayers<sup>93</sup>. Upper-layer PCBM molecules are loosely clustered with no apparent order or registration with respect to the underlying ZnPc film. The height histogram of this film (See Appendix B) indicates three distinct modes. These height variations and known molecular dimensions assist in the interpretation of solute molecules vertical phase separation.

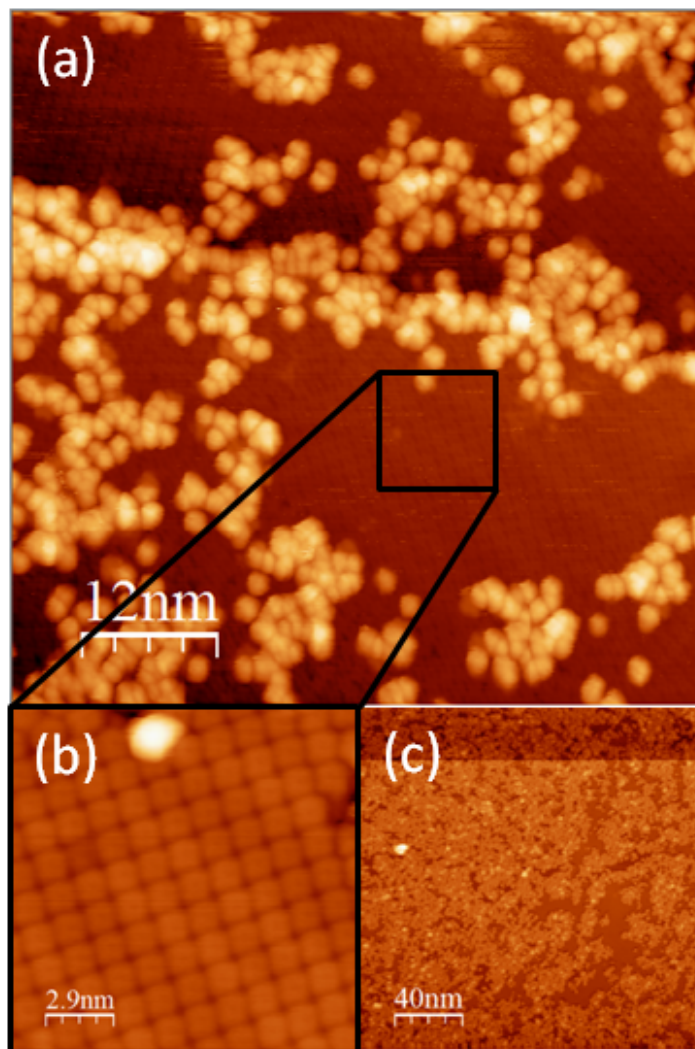


**Figure 4.3** STM images of binary film after thermal anneal (270 °C, 20 min) revealing phase separation is shown: (a) bilayer film with first layer ZnPc (dark) and second layer PCBM (bright spherical protrusions), (b) first layer ZnPc image with molecular resolution, (c) large-scale STM image of binary film. PCBM molecules are brighter regions, and exposed ZnPc monolayer is darker regions.

When the aerosol microdroplets arrive on the Au (111) surface, they first form a disordered film of PCBM, ZnPc, and  $\text{CHCl}_3$  molecules that is continuous and has molecular level (0.15 nm) roughness. This structure (Figure 4.1c) is stable on a timescale of days at room temperature and is reminiscent of glassy molecular films formed by very rapid physical vapor deposition<sup>94</sup>. Thermal activation is required to

release solvent and drive the rearrangement of PCBM and ZnPc into a layered arrangement consisting of an ordered ZnPc layer in direct contact with the Au (111) substrate and a second layer of PCBM. Analysis of images shows that this stacking arrangement is the dominant structural motif, observed on > 90% of the surface area. A large scale example is shown in Figure 4.3c. In patches where this stacked structure is not observed, the PCBM monolayer is generally found. This PCBM monolayer is generally a low-density  $< 0.86$  molecules/nm<sup>2</sup> monolayer phase, consisting of disordered and loosely packed PCBM. Despite the thermal annealing, no domains of 2D hexagonal PCBM are observed.

The vertical phase separation, produced by thermal activation, indicates the PCBM/ZnPc/Au (111) stacking arrangement is lower in energy than the disordered film and kinetically accessible from the disordered film structure. In order to determine if this structure is thermodynamically preferred, we prepared films with alternative initial structural arrangements and measured subsequent structure evolution. In particular, we create films with reverse stacking of solutes, i.e., ZnPc/PCBM/Au (111), and show that rearrangement to PCBM/ZnPc/Au (111) occurs. This indicates that the latter structure is thermodynamically more favorable.

### **Sequential-Deposited Bilayers**

A film of PCBM molecules was first deposited using the pulsed microaerosol deposition source with a 0.5 mmol/L PCBM/chloroform solution onto the bare Au (111) substrate at room temperature. A 1.1 monolayer thickness PCBM film was prepared, to yield a film structure consisting of coexisting 2D hexagonal and disordered domains, as shown in ref 85. A single monolayer equivalent of ZnPc was

then subsequently deposited from the microaerosol source with a 0.5 mmol/L ZnPc/chloroform solution.

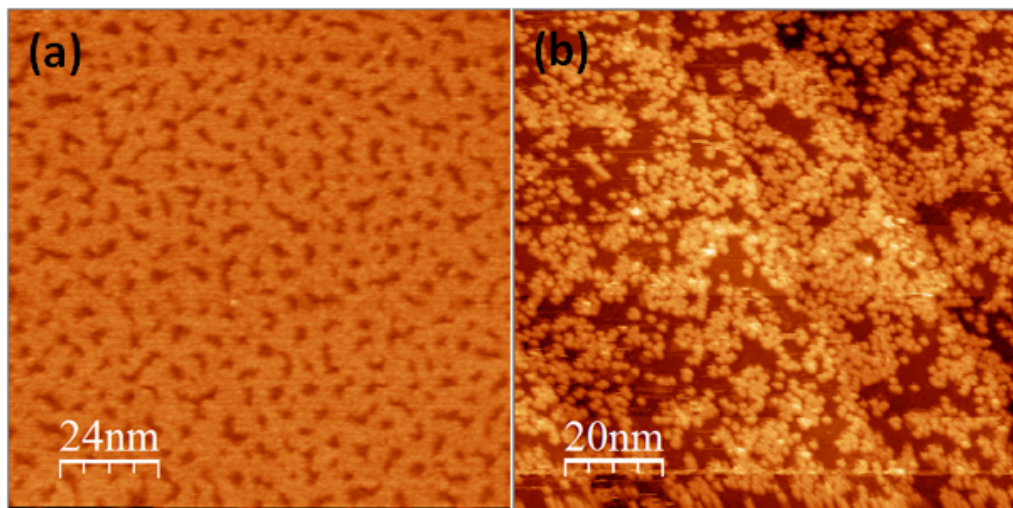


**Figure 4.4** Sequentially deposited monolayer ZnPc on monolayer PCBM/Au (111) films from microaerosol chloroform solvent. STM images show (a) as-deposited film morphology and (b) film morphology after a 20 min, 260 °C anneal.

The morphology of the resulting film, shown in Figure 4.4, appears similar to that of codeposited films (Figure 4.1a). This similarity of appearance in codeposited and sequentially deposited structures is because both films are disordered. Due to diffusion limitations at room temperature, however, the first layer in the sequentially deposited film is predominantly PCBM and the second layer is predominantly ZnPc.

Heating the sequentially deposited ZnPc/PCBM/Au (111) film to 260 °C for 20 min, results in rearrangement to the PCBM/ZnPc/Au structure (Figure 4.4b). This bilayer film structure is extremely stable and persists up to the desorption temperature of PCBM.

Rearrangement of the ZnPc/PCBM/Au film to PCBM/ZnPc/Au indicates that ZnPc molecules can displace PCBM molecules from the Au (111) surface. Such molecular

displacement has been observed when the adsorption energy of the displacing molecules exceeds that of the displaced molecules<sup>95</sup>. However, previous temperature-programmed desorption (TPD) studies reveal that the adsorption energy of ZnPc is smaller than that of PCBM (considered as C<sub>60</sub> cages)<sup>96</sup>(see Table 4.1). In this bilayer case, intermolecular interaction energies must also be considered. We carried out simple DFT calculations on the dimers to explore the energy difference between these two different ZnPc/PCBM dimer arrangements (as shown in Figure 4.5). These calculations, predict that the difference in intermolecular energy between these dimer arrangements is negligible (~2 meV) and the preferred arrangement cannot be predicted from this simple dimer calculation. We turn to molecular electrostatics considerations, which have proven to be a very useful structure predictor in crystal engineering<sup>97</sup>. We next compute the electrostatic energy of two dimer stacking arrangement illustrated in Figure 4.5, taking into account electrostatic interaction with the substrate.

This calculation utilizes the intrinsic dipole moment of PCBM and the quadrupole moment of ZnPc. PCBM has an intrinsic dipole moment of 1.85 D<sup>98</sup> and ZnPc has a quadrupole that is equivalent to a dipole moment of 4.05 D<sup>99</sup>, as depicted in Figure 4.5a. Calculating the energy between dipole and its image dipole as  $E = p^2/4\pi\epsilon_0 r^3$ , we determine the electrostatic energy of those two stacking arrangements:  $E_1 = -0.23$  eV (Figure 4.5b) and  $E_2 = -0.07$  eV (Figure 4.5c). The distance between these charges and their images,  $r$ , follows the molecular dimensions: the height of C<sub>60</sub>-PCBM is 1.2 nm (the C<sub>60</sub> cage is 0.71 nm), the ZnPc-Au (111) monolayer separation is 0.2 nm and a 0.3 nm van der Waal separation between the fullerene cage and ZnPc is assumed.

The calculated energy difference between the two stacking arrangements is  $E_1 - E_2 = -0.16$  eV with the observed PCBM/ZnPc/Au stacking arrangement lower in energy. As a point of fact, the electrostatic energy between PCBM and its image is calculated as point charges instead of dipoles due to the breakdown of far-field approximation. Computational details for this calculation are found in the Appendix A.

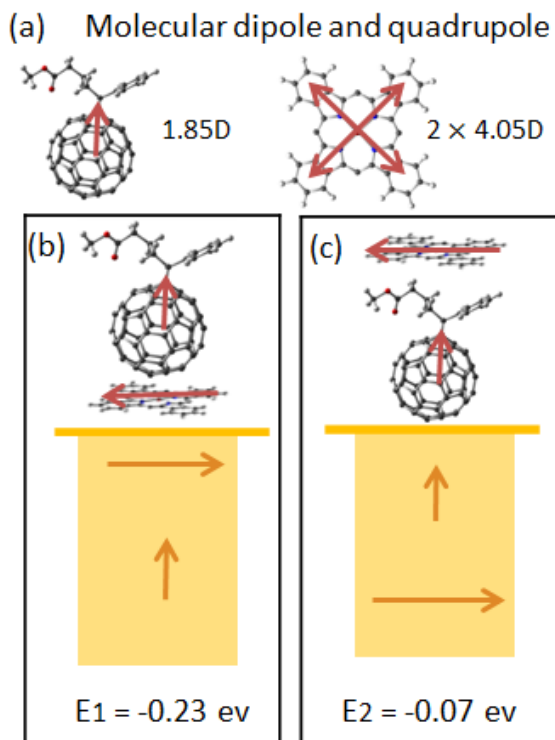


**Figure 4.5** Electrostatic energy computed for two different dimer stackings: (a) Molecular moments; red arrows depict dipoles. (b) PCBM/ZnPc/Au arrangement. (c) ZnPc/PCBM/Au arrangement. Yellow represents Au (the bright line is the Au (111) mirror plane). Image dipoles are shown as gray arrows. PCBM/ZnPc/Au (111) stacking favored by 0.16 eV (= 3.7 kcal/mol) over ZnPc/PCBM/Au (111) stacking.

According to this simple electrostatic calculation, the PCBM/ZnPc/Au stacking sequence is preferred because the energy cost of raising the quadrupolar ZnPc from its image is greater than the energy cost of raising the dipolar PCBM from its image. This electrostatic effect will be quite general for symmetrical macrocycles (which

have a substantial quadrupole moment) in combination with molecules with large dipole moments.

Because fullerenes have strong intermolecular interactions (see Table 4.1), we further examined the impact of PCBM local density on displacement by ZnPc. Previously we showed that the deposition of a PCBM monolayer of initial average density  $> 0.86$  molecule/nm<sup>2</sup> yields PCBM monolayers with coexisting 2D hexagonal regions (0.86 molecules/nm<sup>2</sup>) and disordered regions<sup>89</sup>. Covering such a two-phase PCBM monolayer with a ZnPc layer, followed by annealing, reveals two variations in the displacement of PCBM. Figure 4.6a shows isolated PCBM molecules displaced to the second layer by ZnPc. Figure 4.6b shows undisplaced PCBM arranged as crystalline PCBM islands. In addition, displaced PCBM, both isolated and loosely packed, are observed. The inset of Figure 4.6b reveals the crystalline PCBM islands to be 2D hexagonal, with a nearest-neighbor 0.97 nm distance, in good agreement with our previous study of 2D hexagonal on Au (111). Such 2D hexagonal PCBM are not displaced by ZnPc. In contrast, the isolated and loosely packed PCBM molecules occupy the second layer and are evidently displaced by ZnPc. Second-layer and first-layer PCBM molecules are distinguished by a small apparent height difference of  $\sim 0.1$  nm. These results indicate ZnPc molecules preferentially displace PCBM molecules from Au (111) in regions of lower PCBM density to form the stacked arrangement (Figure 4.5b). In regions of 2D hexagonal PCBM, the PCBM-PCBM interactions are strongly stabilizing and PCBM molecules are not displaced. Further annealing time yields no significant additional changes in film structure.

Bilayer PCBM-ZnPc film structures are shown to depend explicitly on film processing conditions. The stacked PCBM/ZnPc/Au structure is favored and kinetically accessible from initial film structures with lower PCBM densities. The multiphase structure with coexisting 2D hexagonal PCBM domains and PCBM/ZnPc/Au (111) stacking is kinetically accessible from films with higher local PCBM densities. Once formed, the multiphase structure is thermodynamically preferred, as the PCBM-PCBM interactions are much stronger than the electrostatic interactions that lead to PCBM/ZnPc/Au (111) stacking.

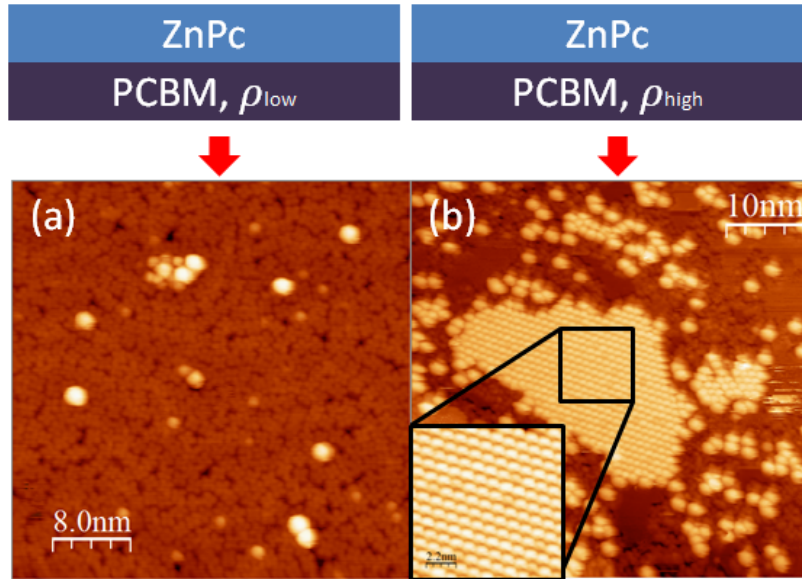


**Figure 4.6** Impact of local PCBM density ( $\rho$ ) on PCBM displacement to second layer: (a)  $\rho_{\text{low}}$ , where PCBM is displaced to second layer. (b)  $\rho_{\text{high}}$ , PCBM nucleate to form 2D hexagonal island (inset) in contact with Au(111), which cannot be displaced to the second layer.

#### 4.4 Summary

Bilayer ZnPc and PCBM films with different initial compositional gradients (mixed vs alternate-layered) are prepared, and thermally driven structure evolution is followed with UHV-STM. Directly deposited films exhibit 0.15 nm height variations



(fwhm) without apparent order. The lack of molecular-level resolution in such films results from the variable molecular orientations, coupled with significant retention of the chloroform solvent. Upon thermal activation (to 80 °C or higher), solvent is released and films order into a PCBM/ZnPc/Au (111) stacking arrangement with noncrystalline PCBM. The displacement of PCBM by ZnPc at the Au (111) interface is thermodynamically preferred and favored by a 0.16 eV/pair reduction in electrostatic energy for the PCBM/ZnPc/Au stacking. Local PCBM density is shown to be an important and limiting factor for displacement to occur. Islands of the higher density 2D hexagonal PCBM phase prove highly stable and are not displaced by ZnPc. As a consequence, codeposited ZnPc and PCBM films, with their lower PCBM densities, preferentially lead to PCBM/ZnPc/Au (111) structures. Seeded initial layers of PCBM, however, generate heterogeneous film structures consisting of coexisting 2D hexagonal PCBM domains and stacked PCBM/ZnPc/Au (111) structures. This work shows how deposition controls can be used to generate film architectures with distinct molecular stacking arrangements at the metal substrate. Molecular stacking directly impacts interfacial electronic properties, and its control is important for device applications.

## **Chapter 5 2D Hexagonal Motifs and Layered Stacking in C<sub>70</sub>-PCBM Films on Au (111)**

We report a molecularly detailed study of structure evolution in thin films of C<sub>70</sub>-PCBM in the monolayer to multilayer regime. We show how molecule-molecule interaction and local density have an impact on C<sub>70</sub>-PCBM monolayer development and layer stacking. Thin films of C<sub>70</sub>-PCBM were generated from fullerene solutes entrained in CHCl<sub>3</sub> aerosol solvent on Au (111) substrates. Structure is tracked from the monolayer to multilayer regime with molecular detail by UHV-STM. Films deposited on room temperature substrates reflect appreciable solvent retention in the range of 10 layers. Upon 80 °C thermal activation, solvent molecules are released and domains of ordered packing arrangements arise, the extent of which depends upon the local PCBM density in the initial films. In high density regions ( $> 0.9$  molecules/nm<sup>2</sup>), 2D hexagonal domains of C<sub>70</sub>-PCBM are produced in the monolayer, with 6% defect densities giving rise to 2D quasi-hexagonal structures. We observe second-layer hexagonal structures nucleated by the hexagonal monolayer structures, and attribute the registration shift between the layers to hydrogen bond formation between the PCBM functional groups. A structural model for the ordered bilayer domains is proposed.

### **5.1 Introduction**

Fundamental STM studies of fullerene and fullerene derivative thin films, in particular of C<sub>60</sub>, C<sub>70</sub><sup>96, 100</sup> and PCBM<sup>89</sup>, are motivated by the necessity to control their morphology in view of applications in quantum-scale photovoltaic device fabrication<sup>101</sup>. The adsorption and self-assembly of functional molecular systems on

solid surfaces is believed to be a powerful tool to fabricate well-ordered structures suitable for potential applications in molecular electronics or nanomechanics. Studies of parent (all carbon) fullerene overlayers on metal surfaces in recent years have also revealed that the adsorption geometry of the fullerene adsorbate depends highly on the electronic structures of the adsorbate-substrate system<sup>102</sup>. Fullerenes are known as strong electron acceptors and we can anticipate that the extent of charge transfer should play a role in determining the geometric structure. Charging of the fullerenes (substrate-to-fullerene electron donation) will alter intermolecular interactions.

Extensive studies of the geometric structures of C<sub>60</sub> and C<sub>70</sub> overlayers on low-index surfaces of the coinage metals Au<sup>103</sup>, Ag<sup>104</sup>, Cu<sup>105</sup> have been reported. As summarized in Table I, C<sub>60</sub> generally forms ordered commensurate arrangements on these surfaces, the (4 × 4) structure on Cu (111)<sup>106</sup> and the (2√3 × 2√3)R30° structure on Ag (111) and Au (111)<sup>100a, 107</sup>, all with a nearest neighbor distance (NND) of 1.004 nm<sup>108</sup>. Additional commensurate structures have been found and identified as metastable states, as they rearrange into the preferred arrangements upon thermal annealing<sup>109</sup> or have been trapped by the confinement of substrate steps<sup>76</sup>. These observations have been understood in the literature by the rule of lattice match. Energy appears to be minimized by monolayer geometries that support C<sub>60</sub>'s preference for 2D hexagonal packing, with the unit cell of the 2D hexagonal monolayer matched to that of the underlying substrate lattice. C<sub>70</sub> overlayers have a greater variety of morphologies than C<sub>60</sub> because the molecular symmetry is lower, leading to a change in the charge distribution. For a C<sub>70</sub> solid, the nearest-neighbor distance is dependent on the molecular orientation: 1.06 nm for freely rotating

molecules (fcc and hexagonal structures) and 1.04nm for molecules with parallel alignment of their long axes, with the long-axis orthogonal to the crystal plane (known as the deformed hexagonal structure<sup>110</sup>). Translating this to monolayer films, C<sub>70</sub> forms the (4 × 4) structure on Cu(111)<sup>105</sup> with upright orientation on the surface. However, the most stable phases of C<sub>70</sub> monolayers on the surfaces of Ag (111) and Au (111) is the ( $\sqrt{13} \times \sqrt{13}$ ) R ± 13.9° structure<sup>111</sup> instead of the expected ( $2\sqrt{3} \times 2\sqrt{3}$ ) R30° structure. In this case, the coulomb repulsion invalidates simple lattice matching considerations. The ( $\sqrt{13} \times \sqrt{13}$ ) R ± 13.9° and the ( $2\sqrt{3} \times 2\sqrt{3}$ ) R30° structures are shown in Figure 5.1. Additional studies have found that C<sub>70</sub> induces pit formation on metal surfaces, as the pits effectively facilitate increased charge transfer to the fullerene (> 1.1 electrons/molecule) from Cu (111) to C<sub>70</sub><sup>112</sup> (for comparison, Cu (111) to C<sub>60</sub> charge transfer is just 1.0 electrons/molecule<sup>113</sup>. ) This increased charge transfer occurs because the C<sub>70</sub> LUMO distributes mainly around the poles of the ellipsoidal-shaped C<sub>70</sub> molecule<sup>114</sup>. Consequently, the LUMO is closer to the metal for better electronic coupling/charge transfer. This causes stronger coulomb repulsion between C<sub>70</sub> molecules than C<sub>60</sub>.

For fullerene derivatives of C<sub>60</sub>-PCBM and C<sub>70</sub>-PCBM, the first electron affinity is similar to that for C<sub>60</sub> and C<sub>70</sub>. However, the HOMO-LUMO gap of C<sub>60</sub>-PCBM (1.496 eV) is smaller than that of C<sub>60</sub> (1.666 eV)<sup>115</sup>. For PCBM derivatives the lowest unoccupied molecular orbital (LUMO) is shifted higher than that of neat fullerenes. From the natural charge populations, adding the functional group onto the C<sub>70</sub> cage does not change the charge populations significantly. Quantum chemistry calculations indicate that the functional group is not involved in the process of photoelectric

conversion, but does play a key role in adjusting the HOMO-LUMO levels for increasing photoelectric conversion efficiencies<sup>1</sup>. Thus, C<sub>70</sub>-PCBM is a promising electron-accepting component for organic solar cell devices. Keen interest in the structure and electronic properties of C<sub>70</sub>-PCBM films on noble metal surfaces motivates the present study. Due to the technological interest in liquid-deposition films, we have utilized a micro-aerosol solvent deposition method to deliver the fullerene solutes from chloroform solutions of micromolar concentrations. The present study focuses on issues of molecular ordering related to PCBM orientation and density.

In this present work we report the UHV-STM study of C<sub>70</sub>-PCBM overlayers on Au (111). We compare the adsorption and molecular ordering of C<sub>70</sub>-PCBM with previous results obtained with C<sub>60</sub>-PCBM (Chapter 3) in light of their geometric and electronic differences.

**Table 5.1** Favored fullerene monolayer structures on (111)-oriented coinage metal surfaces: structural parameters.

Geometric information	C <sub>60</sub>	C <sub>70</sub>
Cu(111)	(4×4) <sup>9</sup>	(4×4) <sup>8</sup>
Au(111) & Ag(111)	$(2\sqrt{3} \times 2\sqrt{3})R30^\circ$	$(\sqrt{13} \times \sqrt{13})R\pm 13.9^\circ$
NND	1.004 nm <sup>10</sup>	1.04 – 1.06 nm <sup>13</sup>
Charge transfer from Cu(111) surface	~ 1.0 e/molecule <sup>16</sup>	> 1.1 e/molecule <sup>15</sup>

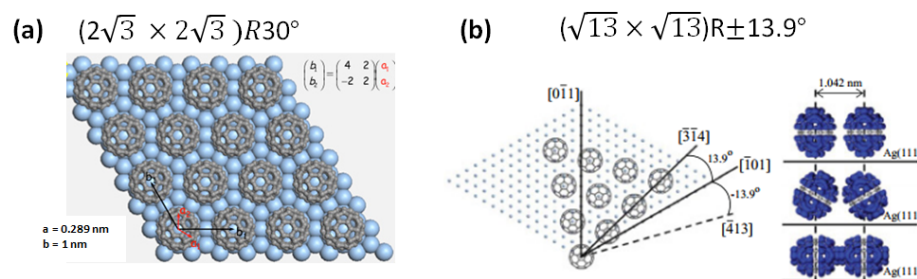


**Figure 5.1** (a) The  $(2\sqrt{3} \times 2\sqrt{3})R30^\circ$  structure of C<sub>60</sub> on metal-(111) surface. (b) The  $(\sqrt{13} \times \sqrt{13})R\pm 13.9^\circ$  structure of C<sub>70</sub> on metal-(111) surface<sup>1</sup>. Nearest neighbor distance (NND) is shown on right with different molecular orientations.

## 5.2 Experimental Methods

The precise deposition control facilitates the present studies of PCBM films from the submonolayer to multilayer regime. For the 0.5 μmol/ml solution concentrations employed in this study, molecular coverage of 0.75% monolayer (ML)/pulse were deposited. A monolayer of C<sub>70</sub>-PCBM is defined as 0.74 molecules/nm<sup>2</sup>. Atomically-clean Au (111) substrates were prepared as described in section 2.2.2. Films were directly transferred to the UHV-STM stage for structural characterization, and measured with constant current STM imaging after deposition.

All images were recorded with positive sample biases (0.75 V - 0.95 V) and low tunneling currents (20-35 pA), 512 line scans and 512 points per line. All image analysis was performed with the program “WSxM”.

### **5.3 Results and Discussion**

Measurements were conducted on films from monolayer thickness to multilayer thickness in order to explore the crystallization habit of C<sub>70</sub>-PCBM molecules and the fundamental mechanisms of interface formation.

#### **C<sub>70</sub>-PCBM deposition on Au (111)**

Films prepared by the deposition of 1 monolayer equivalent (MLE) C<sub>70</sub>-PCBM molecules on the room temperature Au (111) surfaces are first examined. Figure 5.2a presents a large-scale STM image of the resulting film. The image reveals an atomically flat gold terrace, decorated by bright aggregates with no apparent registration to the underlying gold herringbone reconstruction. Expansion of a small area in Figure 5.2b magnifies the bright PCBM islands and the darker regions between these islands. While this magnified image reveals the irregular contours of the aggregates, molecular resolution of these rather large (1 nm diameter) individual PCBM molecules is not obtained. This is attributed to the smoothened topographic contours due to solvent retention in the PCBM film, as well as a distribution of PCBM orientations. We note that the size of the chloroform molecule (0.7 nm diameter) is much smaller than PCBM, and the residual solvent molecules effectively blur the observation of individual PCBM molecules. (We confirm that this is not an artifact of the tip by monitoring tip sharpness by the measured widths of crystallographic steps.)

Height variations in the PCBM film provide evidence for solvent retention and PCBM orientation. Fig. 5.2c shows a line profile of the PCBM film. The 0.20 nm apparent height difference between the dim regions and brighter PCBM aggregates is 1/3 the 0.6 - 0.7 nm values for  $C_{60}$  or  $C_{70}$  molecules in direct contact with metal surfaces. The shallow height variation in this deposited film is consistent with the continued presence of  $CHCl_3$  in the inter-island regions, and its inclusion in the PCBM islands.

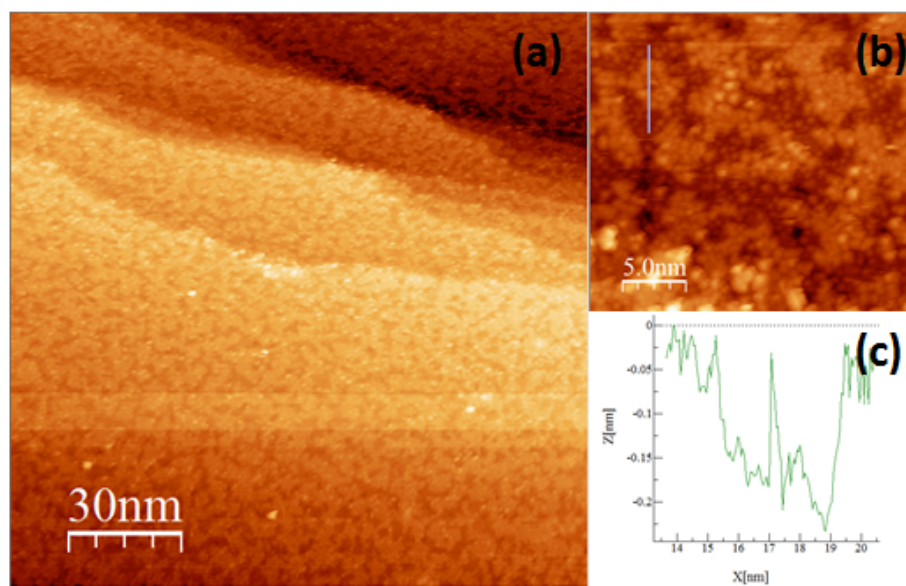


**Figure 5.2** Monolayer PCBM film directly deposited from microaerosol chloroform solvent onto room-temperature Au (111). (a) UHV-STM image, 150 nm  $\times$  150 nm. (b) Magnified region reveals aggregates islands and dim inter-island regions. (c) Line profile taken from the blue line in (b) shows the 0.20 nm apparent height of the PCBM aggregates relative to the dim regions.

Monolayer  $C_{70}$ -PCBM films subjected to thermal annealing undergo morphological changes. Figure 5.3a shows a large scale STM image obtained after a 180°C thermal anneal. Density variations in the film structure are enhanced by annealing, resulting in larger PCBM islands in coexistence with lower-density PCBM regions. Fig.5.3b



displays a lower density area, in which C<sub>70</sub>-PCBM molecules aggregate into small molecular clusters, while Fig.5.3c shows larger PCBM islands with irregular boundaries, indicating regions of higher local PCBM density. This heat treatment further permits the molecular resolution of individual C<sub>70</sub>-PCBM in regions of lower-PCBM density. In the regions with small aggregate islands, Figure5.3b, PCBM molecules appear to be irregularly packed to form disordered structures. In the high-density region (Figure5.3c) PCBM molecules are not individually resolved, suggesting that solvent retention persists even at this relatively high temperature.

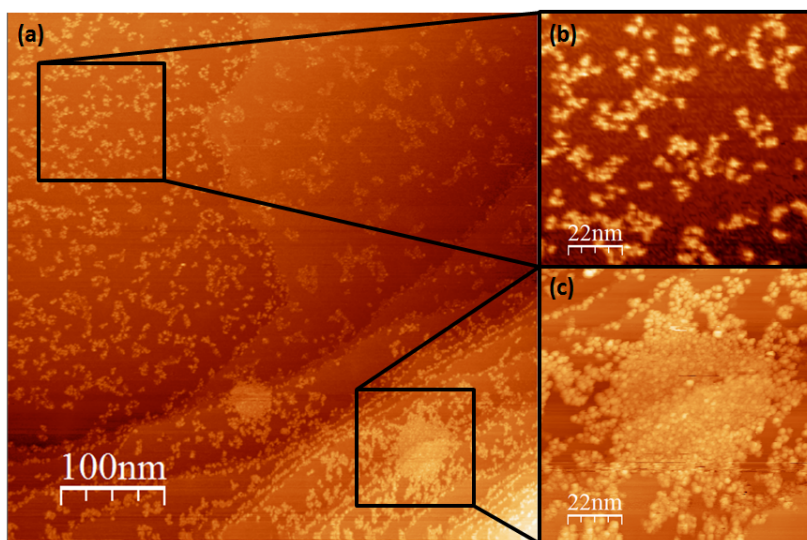


**Figure 5.3** Images of monolayer (1 MLE) C<sub>70</sub>-PCBM film following 180°C annealing for 20 min, acquired by UHV-STM: (a) Film morphology illustrates variable PCBM density, with coexistence of small clusters and larger islands. (b) Magnified region of lower PCBM density demonstrates the irregular features of PCBM aggregates. (c) Magnified image of larger PCBM island reveals the higher local PCBM density and lack of apparent ordering.

### Monolayer Packing – 2D hexagonal and 2D quasi-hexagonal packing

Under stronger thermal activation (to 210 °C), the larger PCBM islands (Fig. 5.3c) undergo further structural transformations, and molecular resolution is readily attained. The C<sub>70</sub>-PCBM molecules arrange into more ordered structures with evident

2D hexagonal domains, as shown in Figure 5.4. Figure 5.4a presents a molecularly-resolved image of a film after 30 min heating to this temperature. Bright spherical protrusions are identified as PCBM molecules. The average apparent height of these domains, measured as 0.6 nm, is consistent with the STM measured height of C<sub>70</sub>-PCBM molecules on metal surfaces. Image 5.4a shows that the PCBM molecules have a spread of apparent heights of 0.15 nm, as measured by the full width at half maximum of the histogrammed height distribution (Figure 5.4c). This spread in apparent heights indicates that the C<sub>70</sub>-PCBM molecules adopt varied orientations at these annealed domains. In magnified images of these domains, most C<sub>70</sub>-PCBM molecules appear to be spherical and possess six nearest neighbors (Figure 5.4b), indicative of 2D hexagonal packing. However, some slightly elongated molecules (Figure 5.4b) and some point vacancies are observed, giving rise to local distortions in the 2D hexagonal packing, which we label as 2D quasi-hexagonal units. Examples of 2D hexagonal and 2D quasi-hexagonal arrangements are marked in Figure 5.4b. The relatively high density of vacancy defects (~ 6 % in Fig. 5.4b) and local distortions in the 2D hexagonal packing is attributed to disorder in the molecular orientations. A fast Fourier transform (FFT) of this PCBM domain reveals the characteristic 2D hexagonal features, and determines the nearest neighbor distance to be  $1.16 \pm 0.05$  nm. This spacing is 11% larger than the 1.04 nm NND of C<sub>70</sub>. This indicates that most C<sub>70</sub>-PCBM molecules adopt upright orientations on Au (111) with some stereo repulsion between the functional groups. The relatively high defect densities (6 %) of the 2D hexagonal domains, and their relatively small sizes (typically 10-25 nm) indicates that the ordering of C<sub>70</sub>-PCBM is much more

kinetically challenged than the ordering of C<sub>60</sub>-PCBM (defect densities < 1%; domains up to 100 nm<sup>89</sup>). This reflects both the reduced symmetry of C<sub>70</sub>-PCBM (more orientational disorder), as well as the stronger metal-to-C<sub>70</sub> PCBM charge transfer (Table 5.1), which will destabilize the domains through dipolar repulsion.

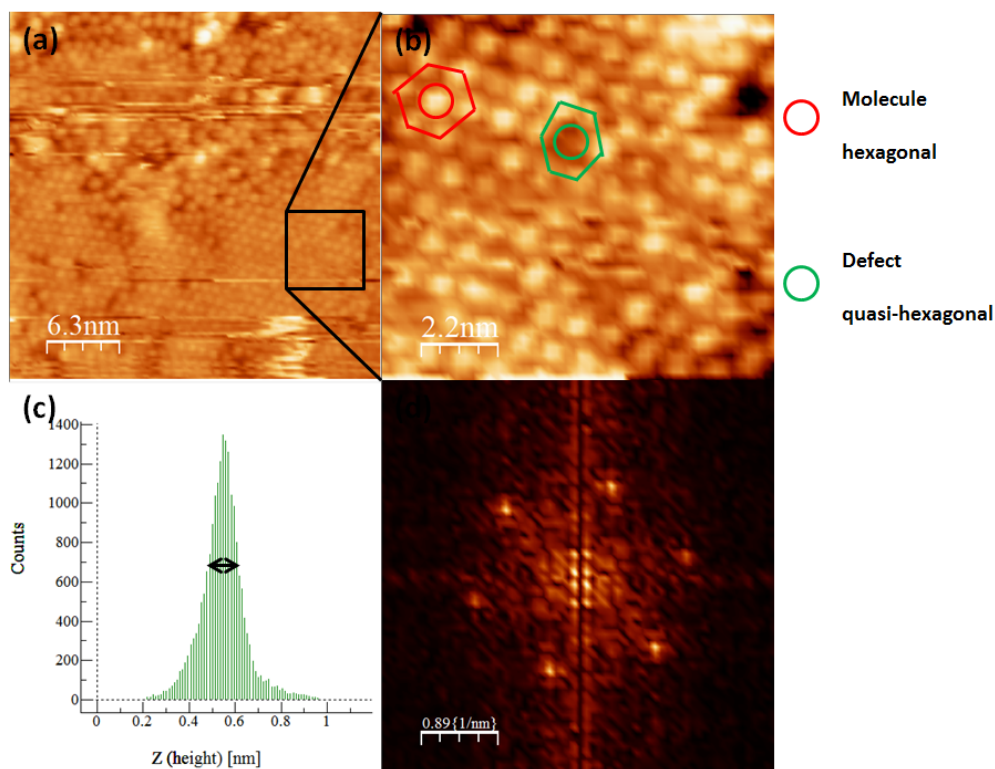


**Figure 5.4** UHV-STM images of high density C<sub>70</sub>-PCBM monolayer regime: (a) Large scale film morphology after a 210°C 30min anneal, 2D hexagonal domains occurs. (b) Scaled image of the ordered 2D hexagonal domain. 2D hexagonal packing molecule and unit cell is marked with red color, and orientational defect and 2D quasi-hexagonal unit is marked with green color as shown. (c) Histogram of film a, reveals monolayer hexagonal packing molecules with FWHM = 0.15 nm. (d) FFT of image b, NND is measured as  $1.16 \pm 0.05$  nm.

We next address how variations in the PCBM monolayer film structures impact the subsequent structure of the PCBM multilayer films. In particular, we examine the impact of the finite 2D hexagonal PCBM monolayer domain sizes on bilayer film

structures. We also explore the impact of varied PCBM orientations on the 2nd-layer film orientation.

### **Multilayer Films: Functional Groups & Interlayer Coupling**

Multilayer PCBM films are readily generated by the microaerosol molecular beam deposition method. Unannealed multilayer films are reminiscent of the as-deposited monolayer films: largely disordered and impossible to image with molecular resolution. However, following the same thermal protocols as monolayer films (annealing to 210°C), we achieve molecular resolution on multilayer films and are able to obtain structural insights on the crystallization and stacking of PCBM layers.

Figure 5.5 shows a multilayer film structure. We note that PCBM films, like most molecular films, do not grow in a layer-by-layer fashion, giving rise to films with multilayer structures. Figure 5.5 shows an image that includes regions of monolayer PCBM, bilayer PCMB, and even tri-layer PCBM, with surface areas of 50%, 35% and 15%, respectively. The ability to image multiple layer structures with molecular resolution allows us to draw insight into the layer stacking. Figure 5.5a is a large scale STM image of a film which contains both crystalline and disordered regions. Double-row and 2D hexagonal structures, found in the monolayer and bilayer regions respectively, are enlarged. We focus our attention on bilayer regions with toplayer hexagonal packing, as presented in Fig. 5.5b. The apparent height difference between the two PCBM layers is measured as 0.20 nm, based upon a height histogram (Fig. 5.5c). We note that each layer has a height distribution ("roughness") of just 0.1 nm, as measured by the FWHM in the height distribution. This is consistent with the monolayer topography in the ordered hexagonal domains.

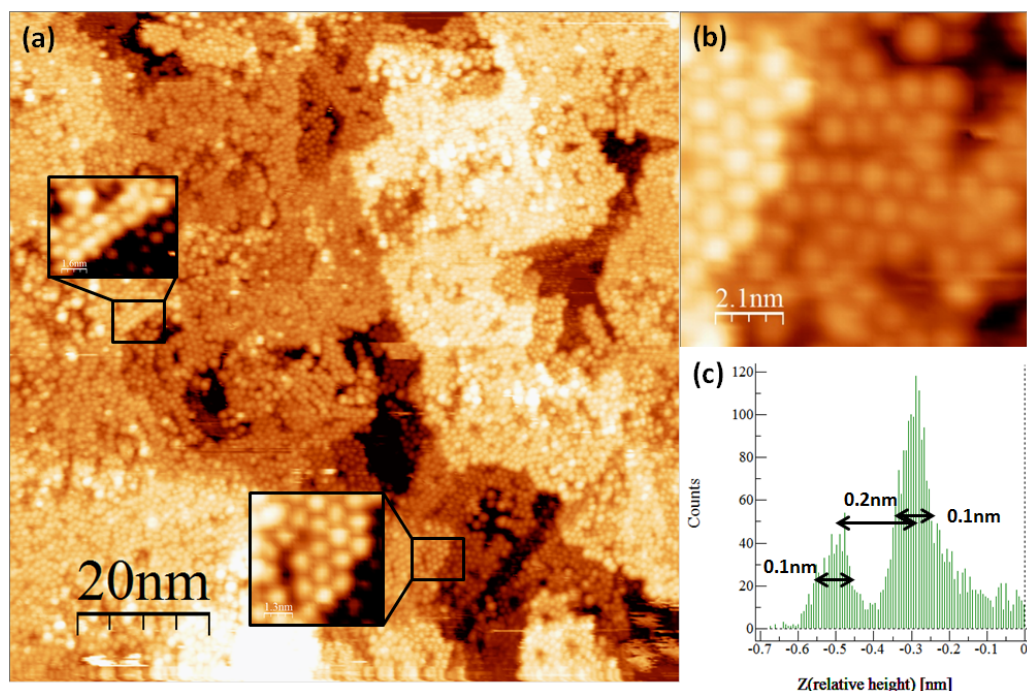


**Figure 5.5** STM images of multilayer C<sub>70</sub>-PCBM films after 210 °C anneal for 30 min: (a) Both double-row structure and 2D hexagonal ordering can be found in the multilayer film. (b) Scaled image of a two layer area from image (a). The second layer has a shift in registration compared with the first layer molecules. (c) Height histogram of film (b) has two significant modes with FWHM = 0.1 nm for both and a height difference between two layers measured as 0.2 nm.

We generally observe that second-layer hexagonal ordering is found only above surface regions where hexagonal ordering is found. Here we take advantage of the multilayer film structure, in which the successive layers do not completely cover the monolayer, so that we may simultaneously characterize both layers. Unsurprisingly, the structure of the second PCBM layer is sensitive to the structure of the first PCBM layer, indicating second-layer PCBM is "templated" by the first-layer hexagonal arrangement.

We next determine the registration between the layers in these locally ordered PCBM bilayer structures. We mark the unit cells of the first layer and second layer

molecules in Fig. 5.6 with red and green circles, respectively, revealing the registration of the second PCBM layer above the first layer. Accordingly, we find that second layer molecules occupy the two-fold bridge sites of the first layer hexagonal structure (Figure 5.6b). This interlayer registration is reasonable based upon the symmetry of  $C_{70}$ -PCBM and the exposed phenyl- butyric acid methyl ester functional groups of the monolayer PCBM films. These exposed functional groups are available to interact with functional groups in the second PCBM layer to form hydrogen bonds between the layers, resulting in assembly of dimer pairs. Dimer formation drives the second layer hexagonal packing, accounting for the registration shift between the layers. Moreover, this dimer structure is an efficient packing arrangement, and lowers the energies of the films. Monolayer dimer structures of  $C_{60}$ -PCBM molecules have been observed and energies are computed in previous works<sup>2,89</sup> (Figure 5.7a). A proposed model of the bilayer film structure in locally ordered regions is illustrated in Figure 5.7. Notice that the interlayer spacing predicted by this model is 1.78 nm.

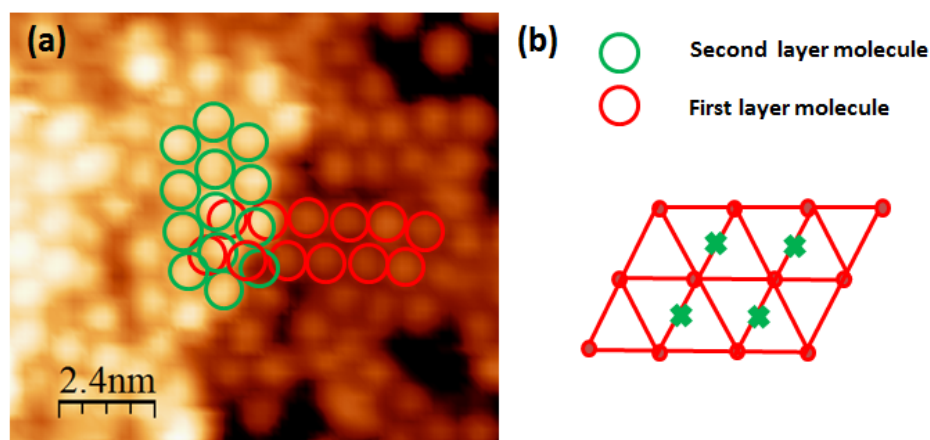


**Figure 5.6** Registration between first and second layer  $C_{70}$ -PCBM: (a) STM images of partial bilayer  $C_{70}$ -PCBM film from Figure 5.5b. Red circles marked first layer molecules (lower terrace) and green circles correspond to second layer molecule (upper terraces). (b) Lattices of first (red) and second (green) 2D hexagonal layers. Second layer molecules occupy two-fold bridge sites on first layer lattice.



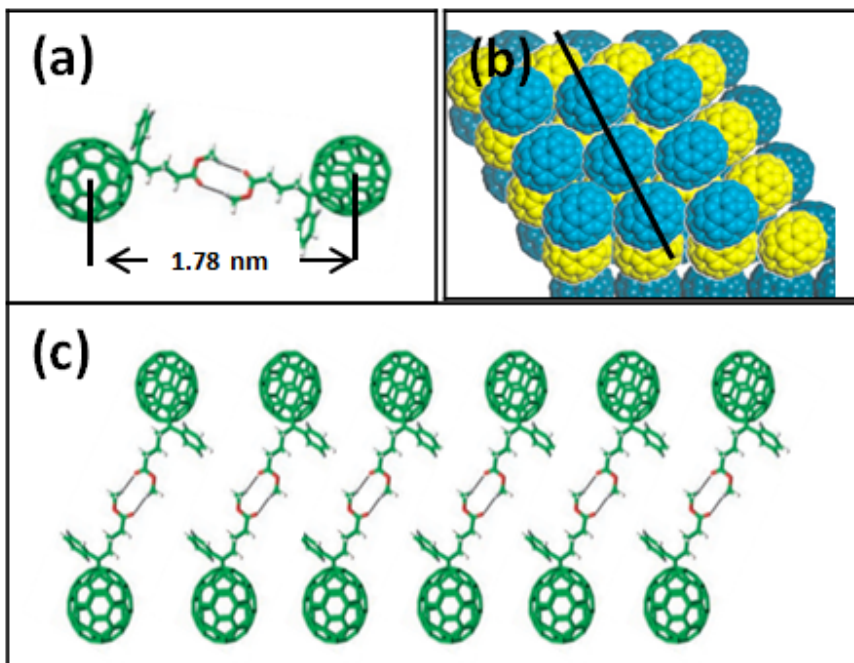


**Figure 5.7** Schematic Model of Crystalline PCBM Bilayers: (a) PCBM dimer, that is the building block of the bilayer, joined by a hydrogen bond between the two ester groups. The fullerene cage space is 1.78 nm based upon DFT calculations<sup>2</sup>. (b) Top view of the bilayer PCBM structure, showing the fullerene cage exposed to the vacuum. (Functional groups cut for image clarity) (c) Side view, taken across the black line in b, depicts the hydrogen bonds and registration shift.

The registration shift between the 2D hexagonal layers in the bilayer film, due to hydrogen bonding, demonstrates the importance of functional groups in interface formation. The absence of long range order is similarly due to the functional groups. Crystallization processes in molecules with strong anisotropic interactions, such as PCBM, lead to the complex film structures reported herein. The functionalization of fullerenes to increase their solubilities and permit solution processing thus has a profound impact on the structure of fullerene films. The functional group and molecular geometric structure is key factors in determine fullerene-derivative OPV and solar cell device performances.

## 5.4 Conclusion

C<sub>70</sub>-PCBM thin films from chloroform solution are prepared, and thermally-driven structure evolution is followed with UHV-STM. Directly deposited films exhibit 0.20 nm height variations without apparent order. The lack of molecular-level resolution in this film results from the variable molecular orientations, coupled with significant retention of the chloroform solvent. Upon thermal activation, solvent is released and 2D hexagonal domains nucleate in regions with higher PCBM local density. The characteristic 2D hexagonal domain size is on the order of 10 - 25 nm<sup>2</sup>, and the hexagonal monolayer structures exhibit 1.16 nm nearest-neighbor separations. Low symmetry C<sub>70</sub>-PCBM molecules, produce both hexagonal and quasi-hexagonal monolayer ordering, with a defect density in the order of 6 %. This lattice constant indicates that the PCBM molecules have orientational disorder in the functional groups, accounting for the large distance between the PCBM molecules. This structure is incommensurate with Au (111). Multilayer (up to 3-layer) films of PCBM are imaged with molecular resolution. The structure of the bilayer film in regions with locally ordered hexagonal layers is measured in detail. A characteristic registration shift observed between the first and second hexagonal layers, as well as the substantial interlayer separation, indicates the formation of hydrogen bonds between ester groups on the first and second layer PCBM molecules. Hydrogen-bond interactions are thus playing an important role in multilayer structure formation. This work provides insight into film architectures with distinct molecular ordering at the metal substrate. Molecular ordering directly impacts interfacial electronic properties,



and its control is important for device applications. Different functional groups and more symmetry fullerene derivatives are subjects of future study.

## **Chapter 6 Supramolecules-CHCl<sub>3</sub> Assembly on Ag (111):**

### **Structure & Stability**

In this last Chapter, we will focus on the unexpected structure and stability of solvent layers on metal surfaces and present a molecularly resolved STM study of the solvent molecule (chloroform, CHCl<sub>3</sub>) adsorption and organization on Ag (111). Chloroform is an organic solvent commonly used in liquid-processing of organic electronic materials due to its high solubility for different polar organic solutes. In Chapter 2, we have described the influence of solvent on the morphology of metal phthalocyanine films in the submonolayer regime, due to solvent impact on MPc surface mobility. We now show how pure solvent layers chemisorb on metal surfaces even at room temperature, and explore the impact of ionic supramolecule solutes on the stability and organization of the solvent layer. Adsorption and ordering of supramolecules and solvent molecules are tracked in the monolayer and multilayer regime with molecular level detail by UHV-STM. Based upon previously reported UHV studies of the thermal properties of hydrochlorocarbon molecules<sup>116,117</sup>, the present observation of the persistence of monolayers of chloroform on the surface at temperatures as high as 80 °C is quite unexpected. Possible physical explanations for the unexpected stability of chloroform layers, prepared by aerosol deposition, will be discussed.

#### **6.1 Introduction**

As described previously, under far-from-equilibrium growth conditions, the resulting fullerene and MPc film morphologies are solvent sensitive and highly variable. In Chapter 3, 4, 5, we presented molecular-level studies of solute nucleation, growth and

solvent expulsion. The persistence of solvent molecules in these semiconducting organic electronic films is an important effect that is not well acknowledged in the organic electronic community. To obtain further insights into the persistence of solvent molecules at electrode surfaces, we focus herein on more basic observations of solvent adsorption and ordering. Measurements of the properties of organic solvent layers are of both fundamental interest and needed to advance liquid deposition technologies.

Chloroform has a variety of useful applications, providing additional motivation for its study. The major industrial use of chloroform is for the production of chlorodifluoromethane, an important precursor to tetrafluoroethylene, a refrigerant known as Freon 1114, and a reagent needed to manufacture Teflon. As a solvent, chloroform is largely unreactive, miscible with most organic solutes, nonflammable and conveniently volatile. Under suitable conditions, it serves as an important reagent in organic synthesis, particularly as a source of the dichlorocarbene  $\text{CCl}_2$  group. In previous chapters, we chose chloroform as the main solvent to serve our liquid aerosol deposition experiment because both ZnPc and PCBM have comparatively  $\mu\text{g/L}$  solubility in chloroform. The solvent retention, and its impact on solute ordering, motivates further study of the adsorption and ordering of pure chloroform molecules at electrode surfaces.

To provide background for the present investigations of solvent monolayer and thin film structures, we first summarize the known solid state structures of chloroform. Chloroform, unlike similar haloforms, has a single known crystal structure, as shown in Figure 6.1. This crystal structure of bulk solid chloroform was determined by

Fourme and Renaud using x-ray diffraction at 185 K<sup>118</sup>. They show that chloroform crystallizes in the primitive orthorhombic system, space group Pnma(D<sub>2h</sub>), with four molecules per unit cell and no evident hydrogen bonding. It has a known melting temperature of -63.5°C.

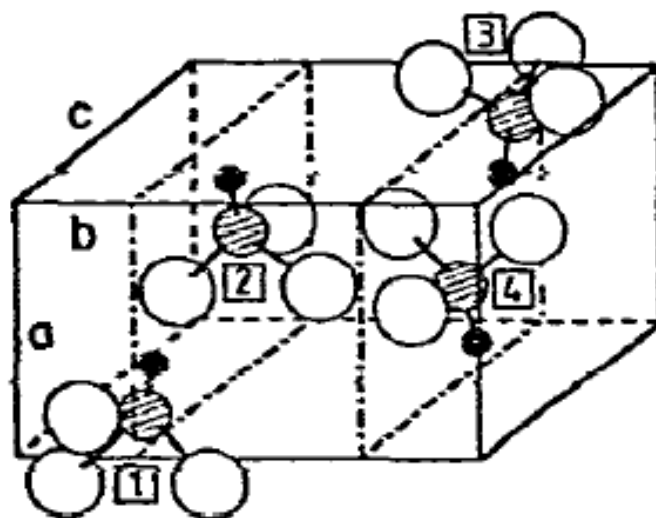


**Figure 6.1** Crystal structure of solid chloroform.<sup>119</sup>

We next summarize previous surface science studies of chloroform on coinage metal surfaces. The UHV adsorption of chloroform gas on Cu (111) in the temperature range -173 – 207 °C was reported<sup>120</sup> in 1999 using line of sight sticking probability (LOSSP) measurements and line of sight temperature programmed desorption (LOSTPD) measurements. Chloroform was found to adsorb molecularly at -173 °C with near-unit sticking probability. On heating to -103 °C on this relatively active copper substrate, the monolayer reacts to form chemisorbed chlorine adatoms and adsorbed ethyne. Above room temperature (47 °C), the initial sticking probability of chloroform on Cu (111) drops to a value of just 0.25.

The above surface study indicates that chloroform molecules on Cu (111) bind to the surface very weakly at room temperature. On the less active Ag (111), chloroform

molecules are expected to desorb fully at room temperature by TPD studies<sup>116</sup>. Consequently, we expect chloroform monolayers to be unstable on the Ag (111) surface at room temperature (Estimate desorption temperature -80 °C, based upon mass-dependent extrapolation of desorption data of other measured hydrochlorocarbon molecules on Ag (111)). We note that more extensive surface science studies have been reported for solvent molecules such as benzene, methanol and acetone, because of their relevance to heterogeneous catalysis<sup>121</sup>. In all cases, these molecules desorb molecularly from Ag (111) below room temperature. Halocarbon solvents, such as chloroform and dichloroform, are generally less studied, except in the context of surface photochemistry<sup>122</sup> and dechlorination<sup>123</sup>, the latter on more active metals such as palladium.

In the present STM studies of solvent adsorption, we focus on chloroform as a model solvent system. We have found that chloroform is easy to image with molecular resolution by STM, facilitating the present structural investigations. In the present work, we seek to observe and account for the stability of chloroform adlayer structures. Second we examine how the presence of ionic solutes impacts the stability and structure of the adlayer.

To facilitate our exploration of this topic, we select the tris(spiroborate) cyclophane anion,  $C_{186}H_{244}B_3IrN_6O_{12}^{-3}$ , referred to as “twin bowls”, and the tpy:2,2':6',2"-terpyridine cation,  $IrN_6C_{30}H_{24}^{+3}$  as ionic solutes, as shown in Figure 6.2<sup>124</sup>. The corresponding counterions of the anion and cation are  $Me_2NH_2^+$  and  $PF_6^-$  respectively. In solution, these ionic solutes self-assemble into supramolecular chains. The anion is used as a host for chemical guests due to its double-bowl shape. The cation has a

spherical shape that fits within those bowls (Figure 6.2). According to NMR investigations, the average length of the supramolecular chains in solution is 20-30 nm. Upon deposition on the Ag (111) surface, we anticipate that the supramolecule-chloroform solvation energy will be substantial (of order 5 eV/monomer<sup>125,126</sup>), further increasing the retention (stability) of the solvent at the Ag (111) interface. We thus investigate and contrast the adsorption and monolayer structures realized by the deposition of pure chloroform aerosol and the chloroform aerosol with ionic supramolecular solutes.

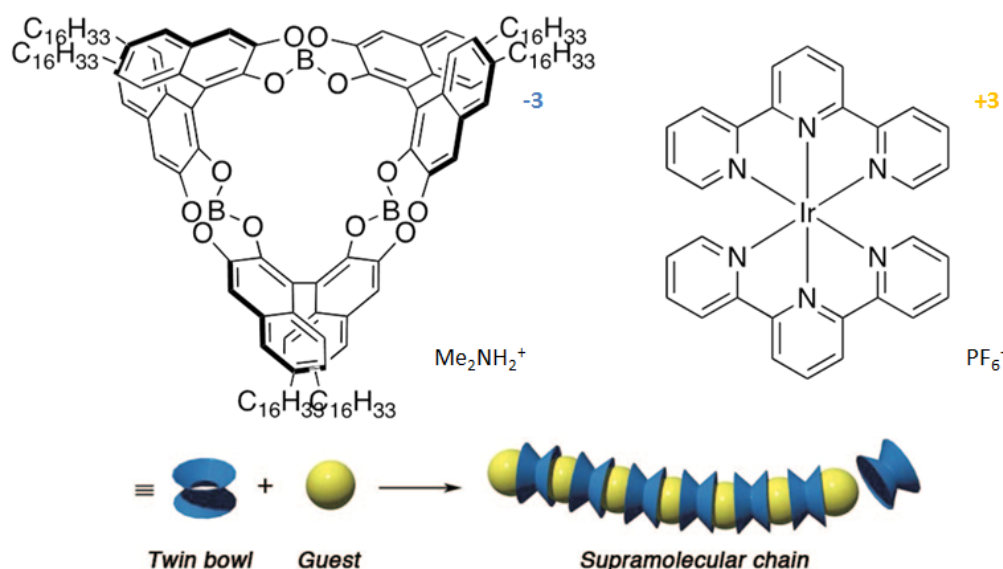


**Figure 6.2** Supramolecular ionic polymer used for the present study: The anion  $C_{186}H_{244}B_3IrN_6O_{12}^{-3}$  (blue) (counterion  $Me_2NH_2^+$ ) and the cation  $IrN_6C_{30}H_{24}^{+3}$  (olive) (counterion  $PF_6^-$ ) assemble into the linear supramolecular structures shown as above. This assembly is facilitated by the "twin bowls" shape of the anion unit.

## 6.2 Experimental Methods

Chloroform solutions with the twin bowls supramolecular ionic polymer were prepared by combining 0.084 mmol/L (of the monomer ions  $C_{186}H_{244}B_3IrN_6O_{12}^{-3}$  and  $IrN_6C_{30}H_{24}^{+3}$ ). Twin bowls supramolecules were deposited using the microaerosol

deposition method. A coverage of 0.13% twin bowls ML was deposited per pulse. We define 1ML of twin bowls as  $0.53 \text{ monomer/nm}^2$ . All images were recorded with positive sample biases (0.7 V – 1.0 V), low tunneling currents (20 - 40 pA). Ag (111) surfaces were prepared by Argon ion sputtering and subsequent annealing as described in section 2.2.2.

### **6.3 Results and Discussion**

#### **Pure $\text{CHCl}_3$ Films on Ag (111)**

Following UHV deposition of 1000 pulses of microaerosol chloroform droplets (corresponding to 5-10 multilayers of solvent in the dosage) on the room temperature Ag (111) surface, samples were transferred in situ to the STM for structural characterization. STM measurements could be performed within 15 minutes of deposition, and the films could be imaged stably for periods up to 3 days. Figure 6.3a shows a large-scale STM image of the sample surface following chloroform deposition. The sample surface topography displays a bi-level structure consisting of bright (higher) regions which contain darker (lower) irregularly shaped vacancy islands. The surface morphology changes significantly after deposit solvent molecules, and the solvent molecules stick on the surface and form film with irregular vacancies. Topographic profiles across the vacancy island (Figure 6.3b) indicate the depth of the vacancy island to be just 0.15 nm, considerably smaller than the silver step height on Ag (111) surface (0.25 nm). We conclude (see further below) that the dark regions represent monolayer chloroform films in direct contact with the Ag (111) substrate, and the bright regions (Fig. 6.3) are due to a second-layer of solvent molecules.

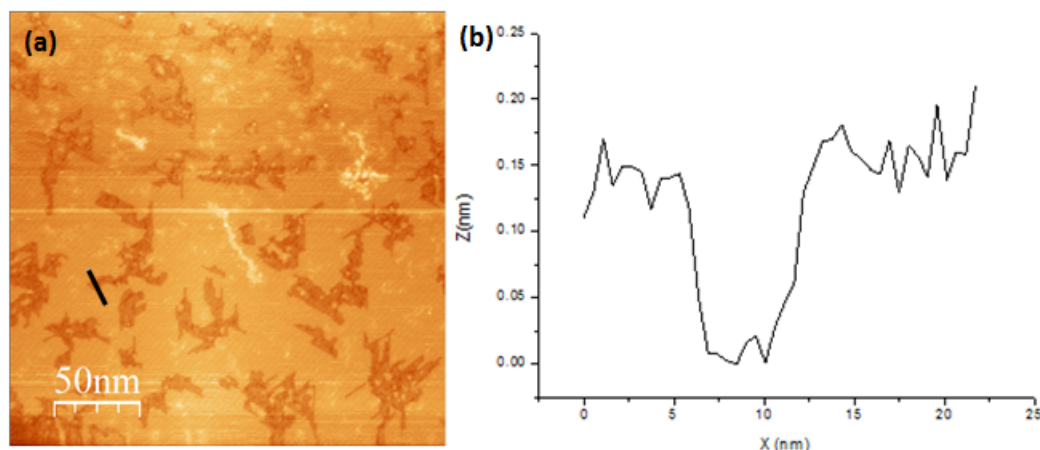


**Figure 6.3** Topography of chloroform film on Ag (111) following microaerosol deposition on the room temperature substrate. (a) STM image shows a bi-layer structure, with irregular island voids. (b) Topographic profile across the vacancy island (blue line in (a)) reveals the 0.15 nm island depth.

Deposition of chloroform generally results in the formation of multilayer structures, which may be imaged on room temperature substrates for up to one day. Figure 6.4a, acquired in another surface region, shows a surface with a tri-layer film of chloroform. As in the above case of the bilayer film, the lowest layer contains irregular-shape vacancies, and second and third layer appear as irregular-shape islands. Such surface topography is typical of molecular films, which generally do not grow in a layer-by-layer fashion. In multilayer regions, we were not able to obtain molecular resolution. However, in the first-layer region, molecular level resolution was occasionally achieved and ordered  $\text{CHCl}_3$  structures were found, as shown in Figure 6.4b. A line profile across the ordered  $\text{CHCl}_3$  monolayer structures revealed a nearest neighbor distance (NND) of 0.88 nm. This distance is three times the Ag (111) nearest neighbor distance, suggesting that the chloroform molecules are locally commensurate with the substrate and experiencing repulsive interactions (enforcing a large separation).



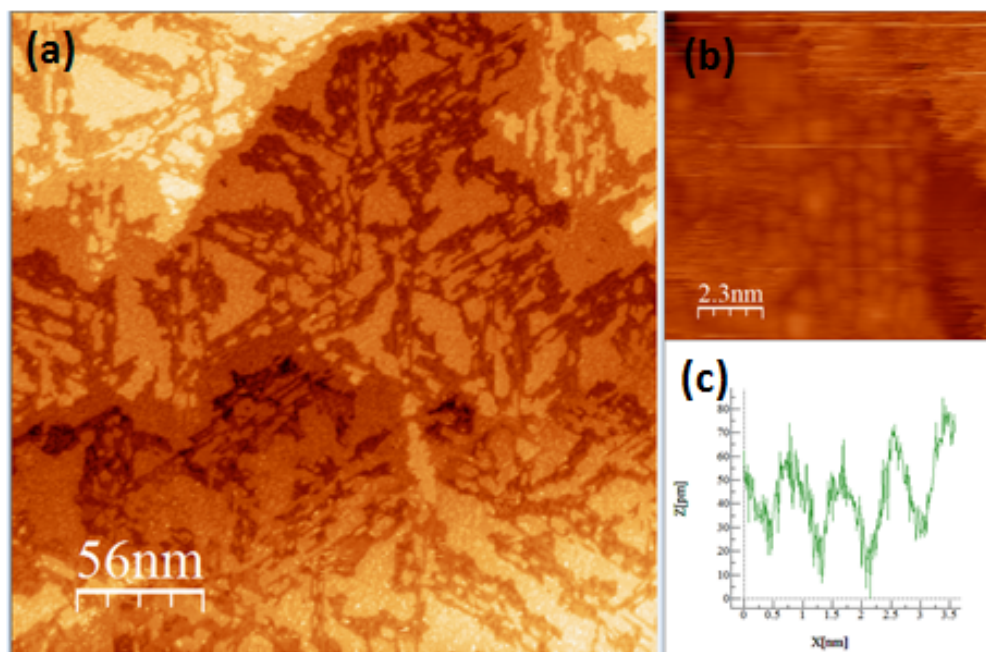


**Figure 6.4** Trilayer of chloroform on Ag (111). (a) Large scale of STM image shows island structure. (b) Magnified monolayer region shows regions with ordering. (c) Line profile of ordered 2D hexagonal  $\text{CHCl}_3$  monolayer region (green line) reveals the nearest neighbor separation to be is 0.88 nm, suggesting a (3 x 3) chloroform adlayer.

These films could be imaged under vacuum for a period of 3 days. Chloroform molecules show a surprising stability on Ag (111) at room temperature even in a UHV environment. Based upon temperature-programmed desorption studies of hydrohalocarbon molecules, chloroform, deposited as a gas, has desorption temperature estimate as  $-80^\circ\text{C}$ . In order to understand the stability of this liquid-aerosol deposited films (relative to the gas-deposited films), we considered two possible explanations. The first is that the aerosol deposition results in the formation of superheated crystals. The second is that contact between the liquid layer and the surface induces a relaxation (mild reconstruction) of the Ag (111) surface, increasing the adsorption energy of the chloroform molecules. We can rule out the possibility of

superheated crystals, as the film is stable with respect to shocking (mechanical disturbance). We note that other solvents (toluene, acetone) studied in our laboratory show similar stability under vacuum. We suspect the stability of these liquid-deposited films involves a solvent-induced relaxation of the substrate, to allow for enhanced film stability. We note that similar solvent retention is observed with other solvents (toluene, acetone on Ag (111)) (although molecular resolution was not observed) and also on Au (111), but not on C (0001). This is consistent with the greater likelihood of relaxing metallic surfaces (which have nondirectional metallic bonds) relative to graphite surfaces (which have highly directional covalent bonds). We suggest that collective interaction between the metallic substrate and the thick solvent layer on deposition may facilitate this structural relaxation.

It is clear that aerosol-deposited small-molecule films are more stable than vapor-deposited small-molecule films. The film must be heated to a temperature of  $\sim 80$  °C to desorb the  $\text{CHCl}_3$ , as observed by imaging the surfaces. We can crudely estimate the desorption energy of the chloroform molecules on the order of 1.0 eV, much higher than the 0.6 eV value determined by extrapolate TPD data of monolayer vapor deposited halocarbon molecules reported by White *et al.*<sup>127</sup>.

The presence of solute molecules at the metallic substrate will additionally impact the adsorption energy of the solvent through the additional stabilizing "solvation energy." A supramolecular ionic solute should significantly change the adsorption energies through solvent - solute interactions. Modified surface energetics due to strong solute - solvent interaction can be further expected to impact the structure of

the solvent layer. To explore these effects, measurements were then conducted on thin films of ionic supramolecules.

### **Supramolecular Ionic "twin bowls" Solutes in Chloroform Films**

Exposure of 0.6 ML equivalent of twin bowls supramolecules from chloroform solution was deposited on the room temperature Ag (111) surface, utilizing the same deposition protocols as for pure chloroform. Figure 6.5 shows two representative STM images of the resulting film morphologies. This solute - containing film reveals striking geometric structures including bright triangular and elongated rectangular islands separated by dimmer regions. The typical size of the island is in the range of 20 - 30 nm and they are separated by distance in the order of 5 -10 nm. Figure 6.5b reveals the molecular ordering in the bright islands. Based upon the observation of 120 ° -rotational domains, these triangular and rectangular structures are commensurate with the underlying Ag (111) substrate. Significantly, ordered suprastructures with 20 - 30 nm lengths (comparable to the twin bowls lengths measured in solution by NMR) are found within the triangular structures. Based upon the STM measured heights, these striking triangular islands are found to be tri-layer structures. The bright islands are assigned to 2D arranged chains of the supramolecules, and the supramolecules are molecularly resolved in the geometric islands as shown in Figure 6.5b. The boundaries of the bright islands appear blurry and reveal ion-exchange along the chain ends that is inefficient along the chain sides. This is consistent with easier ion detachment from the chain end. The dim area between the bright islands is region composed of monolayer  $\text{CHCl}_3$  and possibly

counterions in contact with Ag (111). The sizes of counterions are comparable to chloroform molecules.

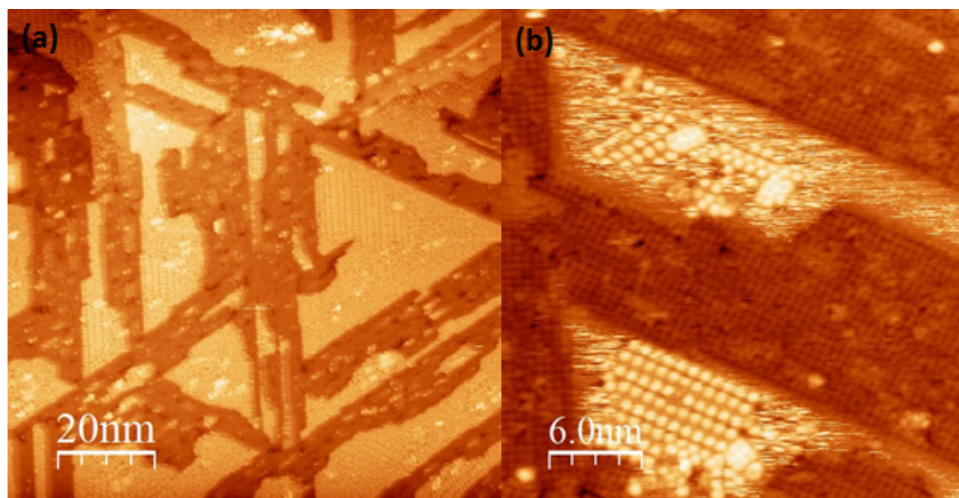


**Figure 6.5** STM images of as deposited  $\text{C}_{186}\text{H}_{244}\text{B}_3\text{IrN}_6\text{O}_{12}^{-3}$  (twin bowls) and  $\text{IrN}_6\text{C}_{30}\text{H}_{24}^{+3}$  molecules, 0.084 mM in chloroform, 0.6 monolayer coverage on Ag (111). (a) Large scale of solute-induced triangular and rectangular structures. (b) Magnification of solute-induced islands reveals details of supramolecular solute packing. Darker region between islands corresponds to monolayer chloroform and possible counterions in direct contact to Ag (111).

We next focus on the detailed molecular ordering in the bright islands and in the dim area.

High resolution images of both the solute-induced islands and dim areas are shown in Figure 6.6. The molecular packing inside the solute-induced island is enlarged in Figure 6.6a inset and Figure 6.6b, showing the geometry and unit cell dimensions of the structure. We note that the boundary of bright islands are lower (by 0.05 nm) than the ordered regions, and appear noisy. This is attributed to a solvating chloroform (or counterion) zone along the twin bowls domain boundary. The darker (chloroform monolayer) regions found between the large triangular structures are shown in Fig. 6.6e. The observation of this  $c(4 \times 2)$  adlayer structure is comparable

to that observed by White *et al.* for  $\text{CH}_3\text{Cl}$  on Ag (111) based upon LEED measurements. There are also a large number of randomly located brighter spots within these dim areas, as shown in Figure 6.5b, which may correspond to counterions.

Further details of the supramolecule islands and the  $\text{CHCl}_3$  monolayer lattices are measured by line profiles of these two packings in Figure 6.6. In Figure 6.6 a – d (supramolecule solutes in triangular islands), the NND along the two vectors are measured as 0.83 nm and 1.67 nm, with an internal angle of  $60^\circ$ . This size reveals a nesting structure of twin bowls chains structure, consistent with previous reported result.<sup>128</sup> The additional STM internal structure (Figure 6.6b) is attributed to the protruding  $\text{C}_{16}\text{H}_{33}$  hydrocarbon chain on the twin bowls anions. In Figure 6.6 e – h,  $\text{CHCl}_3$  monolayer, the NND along both vectors are measured as 0.58 nm. This indicates a  $c(4 \times 2)$   $\text{CHCl}_3$  adlayer on Ag (111) (lattice constant is 0.289 nm).

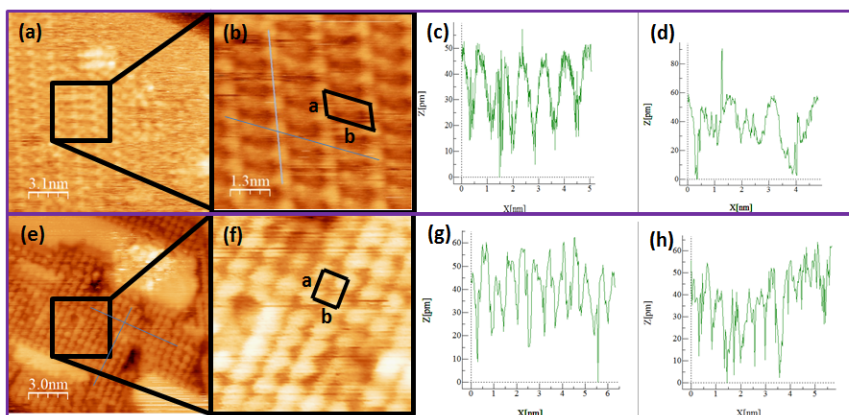


**Figure 6.6** Molecular-resolved STM images of deposited  $\text{C}_{186}\text{H}_{244}\text{B}_3\text{IrN}_6\text{O}_{12}^{-3}$  (twin bowls) and  $\text{IrN}_6\text{C}_{30}\text{H}_{24}^{+3}$  supramolecules, 0.084 mM in chloroform, 0.6 monolayer solute coverage on Ag (111). (a) Internal structure of solute-induced triangular island. Expanded chains structure is shown in (b). (b) – (d) Unit cell dimensions of the supramolecular solute features are measured as  $a = 0.83$  nm and  $b = 1.67$  nm,  $\theta = 60^\circ$  by topographic line profiles. (e) – (h) Molecularly-resolved images of the darker monolayer regions. The lattice constants of the square  $\text{CHCl}_3$  unit cell are measured as 0.58 nm.

Due to the concentration of solute molecules, the corresponding surface areas of the solute-arrays in the film, and the match of their molecular dimensions to the twin bowls supramolecule dimensions, we can confidently identify and assign the twin bowls supramolecules at the Ag (111) surface. We note that the island shape reflects the solvent arrangement about the array of twin bowls supramolecules. The dim regions between these triangular (solvated-solute) islands consist of  $c(4 \times 2)$   $\text{CHCl}_3$  monolayer and counterion clusters. A model of  $c(4 \times 2)$   $\text{CHCl}_3$  structure is shown in Figure 6.7.

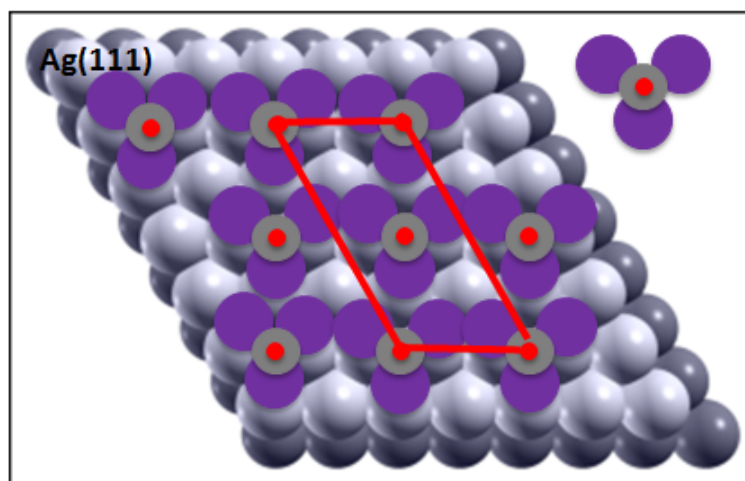


**Figure 6.7** Molecular model of  $\text{CHCl}_3$  ordering, depicting a  $c(4 \times 2)$  adlayer on Ag (111).

We note that this ordering of the chloroform monolayer is comparable to that found for  $\text{CH}_3\text{Cl}$  molecules at low temperatures on Ag (111). In the present work, we do not observe this molecular ordering for pure solvent films. However, the presence of ionic supramolecules and counterions induces the ordering of  $\text{CHCl}_3$  into this ordered  $c(4 \times 2)$  structure in regions away from the supramolecule solute. The ionic solute

molecules thus not only improve the stability of the chloroform adlayer (allowing us to observe multilayer structures), they also induce ordering of solvent molecules.

We summarize the structural features of the twin bowls-CHCl<sub>3</sub> system schematically in Figure 6.8. The geometric shapes of the large triangular and rectangular islands originate from the twin bowls supramolecules. These ionic supramolecules (solution dimensions in the range of 20~30 nm) aggregate into 2D supramolecular arrangements, which were imaged with molecular resolution. The solvation of these 2D structures by chloroform accounts for their geometric shapes, and for the stable imaging of multilayer chloroform. Between these solute islands is found the CHCl<sub>3</sub> monolayer. The ready ordering of the CHCl<sub>3</sub> into the c(4 x 2) pattern may be induced by the stress imposed by the solute islands in the film or seeded by counterions also occupying the c(4 x 2) lattice. Additionally, this ordering may reflect the stabilizing role of the solute supramolecules. We further note that in the solute films, the Ag (111) surface is completely covered by an adlayer. The solutes effectively prevent CHCl<sub>3</sub> desorption from the monolayer, preserving the local 0.25 ML CHCl<sub>3</sub> coverage in the monolayer region that favors c(4 x 2) ordering.



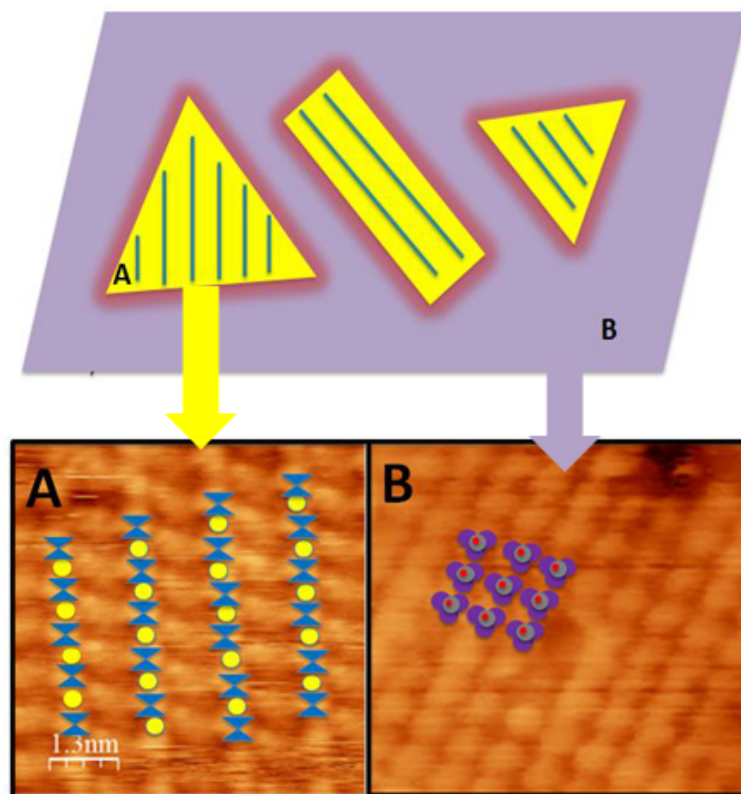


**Figure 6.8** Schematic illustration of domain structures in solute-stabilized  $\text{CHCl}_3$  film: Striated yellow islands (A) are assemblies of twin bowls chain, with assemblies of differing chain lengths yielding triangular domains and assemblies of same-length chains yielding rectangular domains; Violet region (B) corresponds to the  $c(4 \times 2)$   $\text{CHCl}_3$  adlayer. Pink represents the domain-boundary region which is not molecularly resolved.

These results represent the first real-space observation of the twin bowls supramolecules. These results are consistent with NMR measurements of twin bowls, which predict that linear polymers with characteristic chain dimensions in the order of 20-30 nm. We have shown how these ionic solutes provide additional stabilization and ordering of the chloroform solvent layer. However, we remain surprised that the liquid-aerosol deposited pure chloroform forms adlayer structures which are stable (if disordered) at room temperature on Ag (111). We attribute the unexpected stability of these solvent layers to enhanced bonding with the Ag (111) surface, perhaps brought about by solvent-assisted relaxation of the silver surface. This mild symmetry-



preserving relaxation may be induced by the interaction between liquid solvent and the Ag surface atoms.

The presence of ionic species and their solvation energy (estimated as 130 kcal/mol<sup>129</sup>) should stabilize solvent molecules between solute islands, helping to form those highly ordered solvent molecular monolayers. The separation (5-10 nm) between the twin bowls islands is attributed to repulsion between the islands. The ionic supramolecular chain aggregates likely induce stress on the silver substrate, leading to this long-range repulsion between the islands. Size limitation in the twin bowls aggregates (5 - 10 chains) may reflect self-limiting stress. The amorphous boundaries on the aggregate boundaries (twin bowls sides) are attributed to the solvation boundary, for which a noncrystalline arrangement of the solvent molecules (or counterions) is evidently preferred.

In the future, temperature-programmed measurements of the chloroform adsorption desorption energies are needed to separate the impact of the effects of liquid deposition and the effects of solute-co-deposition. Additionally, measurements with other solvent ions of reduced charge are of interest. It would be very useful to have high-resolution (x-ray scattering measurements) performed on the silver surface during liquid adsorption to investigate possible relaxation.

#### **6.4 Conclusion**

We report a UHV-STM study of solvent (chloroform) adlayers on Ag (111) surface at room temperature. Solvent molecules stick on the metal surface and form irregularly shaped vacancy islands in the monolayer regime and irregularly shaped islands in the multilayer regime. With ionic solutes, consist of the anionic

$\text{C}_{186}\text{H}_{244}\text{B}_3\text{IrN}_6\text{O}_{12}^{-3}$  twin bowls and cationic  $\text{IrN}_6\text{C}_{30}\text{H}_{24}^{+3}$  solutes, the supramolecular ionic chains form triangle and rectangular shape islands upon deposition and this induces  $\text{CHCl}_3$  to assemble into  $c(4 \times 2)$  monolayer structures between these solute islands. The square lattice constant is measured as  $a = b = 0.58 \text{ nm}$ . The solvation energy of these ionic species may assist solvent ordering. These kind of solvent layers have never been previously reported in vapor deposited films. This shows the deposition of aerosol droplets (liquid) on metal surfaces may enhance solvent layer stability. Future test of vapor and liquid depositions of  $\text{CHCl}_3$  molecules are needed to obtain a detailed understanding.

## Chapter 7 Summary and Outlook

The formation mechanisms and molecular architectures realized in organic thin films that stand as models for active organic photovoltaic materials were investigated with STM. In particular, I studied the structural evolution of metal phthalocyanines (MPc) and fullerene ( $C_{60}$ -PCBM,  $C_{70}$ -PCBM) films. New predictive insights were obtained on the vertical phase separation of donor/acceptor bilayers, and the impact of functional groups on the ordering in monolayer and multilayer fullerene films. The main goal of this research was to understand the growth and molecular-level ordering mechanisms of donor/acceptor thin films.

We have developed a liquid aerosol delivery sources with fine metering control to enable this fundamental study of deposition and growth of nonvolatile species. Micron-sized droplets are delivered to a sample substrate via a differentially pumped molecular beam source. In this quasi-supersonic source, trains of pulsed droplets impact the surface under UHV conditions.

Several general observations and potential future investigations of interest are proposed for each of the projects discussed:

(1) Aerosol grown ZnPc and TN-ZnPc thin films on Au (111) reflect the volatility of the microaerosol solvent. For low-volatility aromatic solvents, MPc molecules register to the substrate herringbone structure, indicating solvent-enhanced surface transport. As-deposited monolayer films show a broad height distribution, independent of solvent, indicating disordered MPc molecules with nonuniform packing. Thermally treated TN-ZnPc monolayer films show uniform flat-lying surface orientations comparable to PVD grown films and thermally treated ZnPc

films are more randomly ordered in 2D, reflecting weaker molecule-substrate interactions.

All deposition experiments were performed on room temperature substrates. Further tuning of aerosol-generated film structure should be possible through controlled substrate temperature under deposition.

(2) Molecularly-detailed structures of C<sub>60</sub>-PCBM thin films were tracked from the sub-monolayer to the monolayer regime on (111)-oriented Au by UHV-STM. Nascent films reveal glassy monolayer morphologies with substantial solvent incorporation. Subject to step-wise thermal annealing, PCBM monolayers exhibit two distinct crystalline domains depending on local PCBM density, characterized by double-row and 2D hexagonal packing arrangements. The lower-density double-row phase was previously observed in films prepared by physical vapor deposition (PVD). The higher density 2D hexagonal PCBM phase is newly observed and appears to be more thermodynamically favorable, but less kinetically accessible. A relatively high temperature is required to generate the 2D hexagonal islands. Structural models for C<sub>60</sub>-PCBM crystalline domains were presented, and supported by DFT computations.

Low-temperature STM measurements to resolve the 2D hexagonal structure with submolecular resolution and to obtain more precise information on the functional group arrangement in this 2D assembly is of future interest.

(3) Bilayer ZnPc and PCBM films with different initial compositional gradients were prepared and thermally-driven structure evolution was followed with UHV-STM. The lack of molecular-level resolution in directly deposited films reflects variable molecular orientations, coupled with significant retention of the chloroform

solvent. Upon thermal activation, solvent is released and films order into a PCBM/ZnPc/Au (111) stacking arrangement with noncrystalline PCBM. The displacement of PCBM by ZnPc at the Au (111) interface is thermodynamically preferred and favored by lower electrostatic energy for the PCBM/ZnPc/Au stacking. Local PCBM density is shown to be an important and limiting factor for displacement to occur. Islands of the higher density 2D hexagonal PCBM phase prove highly stable and are not displaced by ZnPc.

This work shows how deposition controls can be used to generate film architectures with distinct molecular stacking arrangements at the metal substrate. In the future, local electronic properties of bilayer system can be studied with STS ( $Z(V)$  and  $I(V)$ ) measurements, invaluable techniques to probe nanoscale electronic structure variations corresponding to the STM-characterized film chemical morphology. Scanning tunneling spectroscopy measurements are challenging for organic multilayer systems due to electrical conductivity limitations. The present experiments - in which we can image multilayers - show sufficient conductivity to do high quality local spectroscopy across heterojunctions. However, an apparatus that combines growth and low-temperature spectroscopy capabilities would be needed to overcome perturbing tip-sample interactions.

(4)  $C_{70}$ -PCBM thin films from chloroform solution also order into highly ordered structures in high density areas upon thermal treatment with a characteristic domain size in the order of 10 - 25 nm<sup>2</sup>. The  $C_{70}$ -PCBM molecules produce both 2D hexagonal and 2D quasi-hexagonal ordering with orientational defects in monolayer films. Hydrogen bond interactions through functional groups play an important role in

multilayer formation. We propose structural dimer models with hydrogen-bonding interactions between the functional groups, accounting for the observed 2D hexagonal packing and registry-shift between the 1<sup>st</sup>-layer and 2<sup>nd</sup>-layer.

The phenyl ester groups needed for solution processability create kinetic challenges for large scale molecular ordering. However, the hydrogen bond interactions through phenyl ester groups also enable the formation of multilayer ordering. Hence, different functionalized fullerene derivatives with more symmetry and strong molecule-molecule interactions are of future interest.

(5) Solvent retention under UHV conditions is remarkably observed and strongly impacts film structure evolution for all the above research. Stable chloroform solvent films are obtained even at room temperature under UHV on metal surfaces. Solvation effects in supramolecule adsorption and ordering are additionally explored with ionic supramolecules and those ionic adsorbates induce solvent ordering.

In the future, energetics of CHCl<sub>3</sub> on metal surfaces could be investigated by TPD measurements. Control experiments on vapor deposited solvent thin films (of CHCl<sub>3</sub>) also might lead to further understanding of the adsorption mechanisms and their relationship with growth kinetics, adsorption, and ordering.

New information about organic thin film materials of general importance to organic photovoltaics was obtained. The thin films generated from C<sub>60</sub>-PCBM and C<sub>70</sub>-PCBM by  $\mu$ aerosol molecular beam source have characteristic domain size on the order of 10 - 25 nm. We note that this dimension is comparable to the exciton diffusion length in bulk heterojunctions. Achieving nanophase segregation on this length scale is a

crucial step toward improving the efficiency of small-molecule OPV devices. The incorporation of solvent material shows assistance in material transport. All the structures produced are very stable on a timescale of days at room temperature. The kind of idealized bulk heterojunction structure shown in Figure 1.1 with interdigitated domains of 10-15 nm width and 100-500 nm length, are challenging to generate. We have shown the thin films with domain size of 10-15 nm are readily produced. We have also shown that in binary films, electrostatics and local density determine the layering and structure at the growth substrate. This suggests that the molecular electrostatics and density will be important parameters to optimize in growth to approach the idealized geometry structure of Figure 1.1. Additionally, the rate of solute evaporation will mediate the assembly kinetics.

Using the liquid  $\mu$ aerosol deposition source, not only did we realize favorable growth patterns, but we were also able to deposit and image supramolecules with molecular resolution, as shown in Chapter 6. This methodology expands STM opportunities for studies to other important supramolecular systems.

Based upon the results in this thesis, particular interesting experiments for future work involve local spectroscopy measurements. By doing STM and STS together, structural information could be obtained along with electronic information. That information would help investigate how structural features impact charge transport properties on the interfaces. Working with other functionalized systems to get a general sense of how molecular entanglement would impact ordering will also be very valuable.

This thesis research sought to understand the growth and molecular-level ordering mechanisms at interfaces. Beyond applications in organic photovoltaics, knowledge about adsorption, aggregation and structure evolution is also important for understanding how carbon nanoparticles are transported in the environment and in biomedical applications. Moreover, the general methodology is broadly applicable to other nanoparticle and supramolecular systems.



## Appendices

### Appendix A. Electrostatic Energy Calculation

In Chapter 4, we carry out an electrostatic calculation to find out the energy difference between two dimer stackings. We provide detailed information about the energy calculation here. This calculation utilizes the intrinsic dipole moment of PCBM and the quadrupole moment of ZnPc. The specific calculation steps are as follows:

1. We first calculate the contribution from the PCBM dipole and its image. For an individual PCBM molecule, 0.11 electrons are transferred from the phenyl and butyric acid methyl ester groups to the fullerene C<sub>60</sub> cage. Thus, PCBM can be treated as two  $\pm 0.11e$  point charges separated by a distance of 0.35 nm (from the joint between tail group and C<sub>60</sub> cage to the center of C<sub>60</sub> cage). This corresponds to an intrinsic dipole moment of 1.85 D. Based upon the dipole length and short separation, the energy is computed as point charges. The energy between point charge and its image charge is  $E = e^2/4\pi\epsilon_0 r$ . The two dimer stackings shown in Fig. 4.5 b and c have resulting energies of  $E_{1(\text{PCBM})} = -0.07 \text{ eV}$  and  $E_{2(\text{PCBM})} = -0.07 \text{ eV}$ , respectively.
2. We next calculate the contribution from the ZnPc quadrupole and its image. The quadrupole can be considered as two dipole moments of 4.05 D. Computing the energy between a dipole and its image dipole as  $E = p^2/4\pi\epsilon_0 r^3$ . The two dimer stackings in Fig 4.5 b and c have energies of  $E_{1(\text{ZnPc})} = -0.16 \text{ eV}$  and  $E_{2(\text{ZnPc})} = -3.8 \times 10^{-4} \text{ eV}$ , respectively.

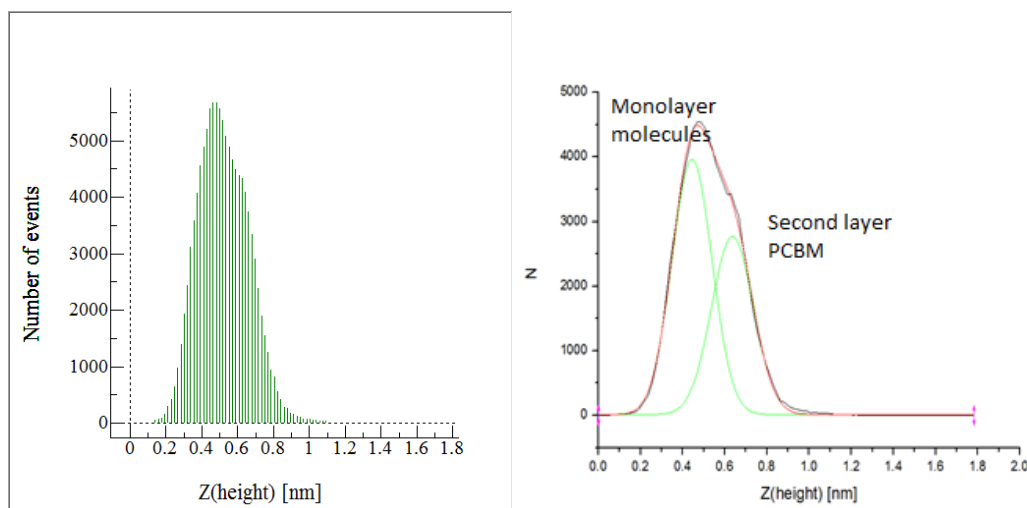
Based upon orientation, there is no contribution from the interaction between the PCBM dipole and ZnPc quadrupole. Therefore, the total energy corresponding to the distinct stacking arrangements is  $E_1 = E_{1(\text{PCBM})} + E_{1(\text{ZnPc})} = -0.23 \text{ eV}$  and  $E_2 = E_{2(\text{PCBM})} + E_{2(\text{ZnPc})} = -0.07 \text{ eV}$ . This result shows that the electrostatic energy differences between these two stackings are dominated by the quadrupole interaction with its image. This is not surprising as quadrupole-quadrupole interactions decay much faster than dipole-dipole interactions.

The calculation utilizes the following distances: the length of  $\text{C}_{60}$ -PCBM is 1.2 nm ( $\text{C}_{60}$  cage is 0.71 nm), monolayer ZnPc positioned 0.2 nm above Au (111) and the van der Waal separation between the fullerene cage and ZnPc is 0.3 nm.

## Appendix B. Height Histogram Analysis of Annealed Films

Detailed information of histogram analysis for binary films in order to further investigate vertical phase separation in Chapter 4 is shown here. Analysis were performed on films after 80°C (Figure 4.2a), 100°C (Figure 4.2b), and 260 °C (Figure 4.3a) annealing, respectively. The structure evolution after thermal treatment is characterized by corresponding changes in the height histograms of those films.

1. After 80°C anneal, the film height histogram (left below) can be fit to two Gaussians (right below):

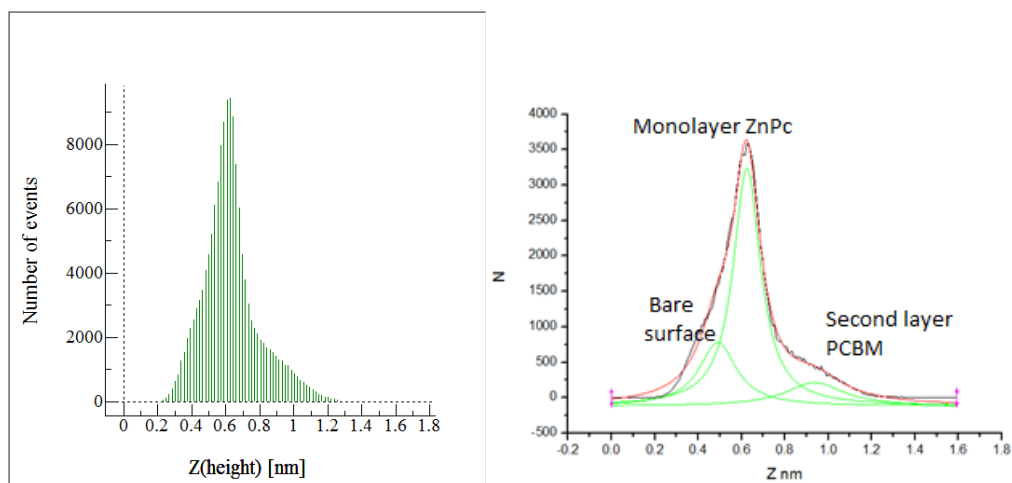


Peaks	Position(nm)	fwhm(nm)	Area(%)
1	0.44	0.19	57.9
2	0.64	0.20	42.1

The apparent height difference of 0.192 nm between these two modes indicates the initial stage of vertical phase separation. The apparent height difference is

less than the 0.3 nm measured apparent height difference between an oriented monolayer (ZnPc) and second-layer (PCBM) molecule, as determined below.

- After 100°C anneal, the film height histogram (left below) can be fit to three Gaussians (right below):

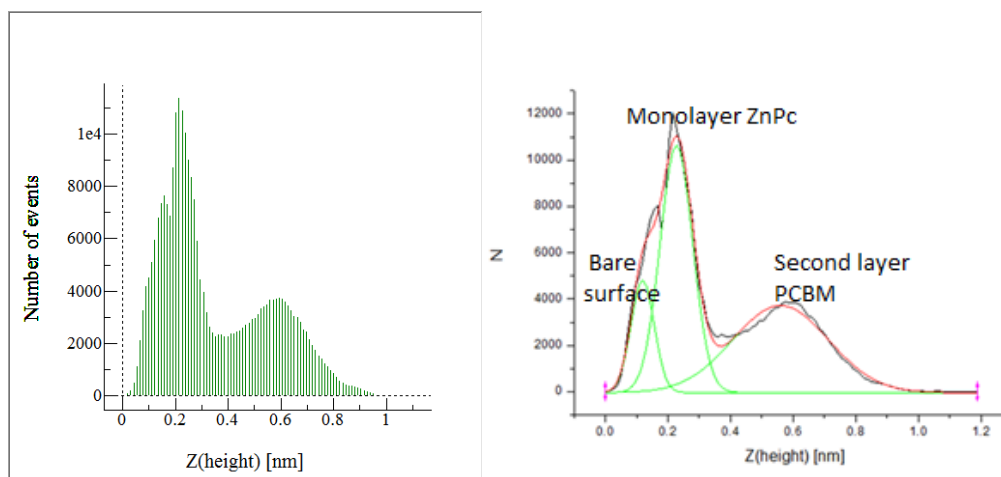


Peaks	Position(nm)	fwhm(nm)	Area (%)
1	0.49	0.21	23.1
2	0.62	0.15	63.6
3	0.94	0.32	13.3

The mode centered at 0.490 nm is the bare Au (111) surface, the mode centered at 0.624 nm is monolayer ZnPc, and that at 0.937 nm is second layer PCBM. Monolayer ZnPc shows a relatively narrow height distribution due its primarily parallel surface orientation. PCBM has a broader distribution due to its variable

orientation (PCBM maximum length is 1.2 nm). Relative area of ZnPc and PCBM show the small amount of second layer PCBM molecules. The apparent height difference between monolayer ZnPc and second layer PCBM is 0.31 nm, consistent with line scans.

3. After 260°C anneal, molecularly resolved STM images with clearly evident bilayer film structure are obtained (Fig. 4.3a). The corresponding film height histogram (below left) shows three modes fit by Gaussians (right below):



Peaks	Position(nm)	fwhm(nm)	Area(%)
1	0.12	0.07	13.7
2	0.23	0.10	42.4
3	0.56	0.31	43.9

The peak for the bare gold surface has a narrow width, as expected, followed by monolayer ZnPc, followed by 2nd layer PCBM (varied orientation). The relative areas of the ZnPc and PCBM correspond to the relative concentration in the film

area. The apparent height difference between the mode centered at 0.227 nm and the mode centered at 0.560 nm (0.33 nm) suggests that PCBM adopt a vertical orientation (as depicted in Fig. 4.5).

## References

1. Wang, P.; Zhang, H.-J.; Li, Y.-J.; Sheng, C.-Q.; Shen, Y.; Li, H.-Y.; Bao, S.-N.; Li, H.-N., *Phys. Rev. B* **2012**, *85*, 205445.
2. Écija, D.; Otero, R.; Sánchez, L.; Gallego, J. M.; Wang, Y.; Alcamí, M.; Martín, F.; Martín, N.; Miranda, R., *Angew. Chem.* **2007**, *119*, 8020-8023.
3. Huang, J.; Li, G.; Wu, E.; Xu, Q.; Yang, Y., *Adv. Mater.* **2006**, *18*, 114-117.
4. Yang, X.; Müller, D. C.; Neher, D.; Meerholz, K., *Adv. Mater.* **2006**, *18*, 948-954.
5. Yang, X.; Neher, D.; Hertel, D.; Däubler, T. K., *Adv. Mater.* **2004**, *16*, 161-166.
6. Halim, M.; Pillow, J. N. G.; Samuel, I. D. W.; Burn, P. L., *Adv. Mater.* **1999**, *11*, 371-374.
7. Qiao, J.; Wang, L. D.; Xie, J. F.; Lei, G. T.; Wu, G. S.; Qiu, Y., *Chem. Commun.* **2005**, 4560-4562.
8. Rehmann, N.; Hertel, D.; Meerholz, K.; Becker, H.; Heun, S., *Appl. Phys. Lett.* **2007**, *91*.
9. Duan, L.; Hou, L.; Lee, T.-W.; Qiao, J.; Zhang, D.; Dong, G.; Wang, L.; Qiu, Y., *J. Mater. Chem.* **2010**, *20*, 6392-6407.
10. (a) Liao, H. H.; Meng, H. F.; Horng, S. F.; Shy, J. T.; Chen, K.; Hsu, C. S., *Phys. Rev. B* **2005**, *72*, 113203;  
(b) Adachi, C.; Kwong, R. C.; Djurovich, P.; Adamovich, V.; Baldo, M. A.; Thompson, M. E.; Forrest, S. R., *Appl. Phys. Lett.* **2001**, *79*, 2082-2084.
11. Lamansky, S.; Djurovich, P. I.; Abdel-Razzaq, F.; Garon, S.; Murphy, D. L.; Thompson, M. E., *J. Appl. Phys.* **2002**, *92*, 1570-1575.
12. Swanson, R. M. In *Approaching the 29% limit efficiency of silicon solar cells*, Photovoltaic Specialists Conference, 2005. Conference Record of the Thirty-first IEEE, 3-7 Jan. 2005; 2005; pp 889-894.
13. Gregg, B. A.; Hanna, M. C., *J. Appl. Phys.* **2003**, *93*, 3605-3614.
14. Peumans, P.; Yakimov, A.; Forrest, S. R., *J. Appl. Phys.* **2004**, *95*, 2938-2938.
15. Forrest, S. R., *MRS. Bull.* **2005**, *30*, 28-32.
16. Hoppe, H.; Sariciftci, N. S., *J. Mater. Res.* **2004**, *19*, 1924-1945.
17. Chen, W.; Qi, D. C.; Huang, Y. L.; Huang, H.; Wang, Y. Z.; Chen, S.; Gao, X. Y.; Wee, A. T. S., *J. Phys. Chem. C* **2009**, *113*, 12832-12839.

18. Johannes, V. B.; Giovanni, C.; Klaus, K., *Nature* **2005**, *437*, 671-679.
19. Deibel, C.; Dyakonov, V., *Rep. Prog. Phys.* **2010**, *73*, 096401.
20. Gao, W.; Kahn, A., *Org. Elec.* **2002**, *3*, 53-63.
21. Fukagawa, H.; Kera, S.; Kataoka, T.; Hosoumi, S.; Watanabe, Y.; Kudo, K.; Ueno, N., *Adv. Mater.* **2007**, *19*, 665-668.
22. Bruner, E. L.; Koch, N.; Span, A. R.; Bernasek, S. L.; Kahn, A.; Schwartz, J., *J. Am. Chem. Soc.* **2002**, *124*, 3192-3193.
23. Armstrong, N. R.; Lin, A. W. C.; Fujihira, M.; Kuwana, T., *Anal. Chem.* **1976**, *48*, 741-750.
24. Alloway, D. M.; Hofmann, M.; Smith, D. L.; Gruhn, N. E.; Graham, A. L.; Colorado, R.; Wysocki, V. H.; Lee, T. R.; Lee, P. A.; Armstrong, N. R., *J. Phys. Chem. B* **2003**, *107*, 11690-11699.
25. Guldi, D. M., *Chem. Commun.* **2000**, 321-327.
26. Guldi, D. M.; Prato, M., *Accounts Chem. Res.* **2000**, *33*, 695-703.
27. Vilmercati, P.; Castellarin-Cudia, C.; Gebauer, R.; Ghosh, P.; Lizzit, S.; Petaccia, L.; Cepek, C.; Larciprete, R.; Verdini, A.; Floreano, L.; Morgante, A.; Goldoni, A., *J. Am. Chem. Soc.* **2008**, *131*, 644-652.
28. Yamada, H.; Imahori, H.; Nishimura, Y.; Yamazaki, I.; Ahn, T. K.; Kim, S. K.; Kim, D.; Fukuzumi, S., *J. Am. Chem. Soc.* **2003**, *125*, 9129-9139.
29. Nakamura, E.; Isobe, H., *Accounts Chem. Res.* **2003**, *36*, 807-815.
30. Chiang, L. Y.; Upasani, R. B.; Swirczewski, J. W., *J. Am. Chem. Soc.* **1992**, *114*, 10154-10157.
31. Nierengarten, J.-F.; Habicher, T.; Kessinger, R.; Cardullo, F.; Diederich, F.; Gramlich, V.; Gisselbrecht, J.-P.; Boudon, C.; Gross, M., *Helv. Chim. Acta.* **1997**, *80*, 2238-2276.
32. He, Y.; Chen, H.-Y.; Hou, J.; Li, Y., *J. Am. Chem. Soc.* **2010**, *132*, 1377-1382.
33. Guldi, D. M.; Asmus, K.-D., *J. Phys. Chem. A* **1997**, *101*, 1472-1481.
34. Wienk, M. M.; Turbiez, M.; Gilot, J.; Janssen, R. A. J., *Adv. Mater.* **2008**, *20*, 2556-2560.
35. Morvillo, P.; Bobeico, E., *Sol. Energ. Mat. Sol. C.* **2008**, *92*, 1192-1198.



36. Thompson Barry, C.; Khlyabich Petr, P.; Burkhart, B.; Aviles Alejandra, E.; Rudenko, A.; Shultz Ginger, V.; Ng Christi, F.; Mangubat Lorenzo, B., Polymer-Based Solar Cells: State-of-the-Art Principles for the Design of Active Layer Components. In *Green*, 2011; Vol. 1, p 29.
37. Tummala, N. R.; Mehraeen, S.; Fu, Y.-T.; Risko, C.; Brédas, J.-L., *Adv. Func. Mater.* **2013**, *23*, 5800-5813.
38. Casalegno, M.; Zanardi, S.; Frigerio, F.; Po, R.; Carbonera, C.; Marra, G.; Nicolini, T.; Raos, G.; Meille, S. V., *Chem. Commun.* **2013**, *49*, 4525-4527.
39. Banerjee, S.; Mazumdar, S., *Int. J. Anal. Chem.* **2012**, *2012*, 40.
40. Yamada, T.; Shinohara, H.; Kamikado, T.; Mashiko, S., *Jpn. J. Appl. Phys.* **2008**, *47*, 1408.
41. Hueblera, A.C.; Doetzb, F.; Kempaa, H.; Katzc, H.E.; Bartzscha, M.; Brandta, N.; Hennigb, I.; Fuegmanna, U.; Vaidyanathand, S.; Granstromd, J., *Org. Electron.* **2007**, *8*, 480.
42. Huang, C.; Nichols, W. T.; O'Brien, D. T.; Becker, M. F.; Kovar, D.; Keto, J. W., *J. Appl. Phys.* **2007**, *101*.
43. Green, R.; Morfa, A.; Ferguson, A. J.; Kopidakis, N.; Rumbles, G.; Shaheen, S. E., *Appl. Phys. Lett.* **2008**, *92*.
44. Chan, C. K.; Richter, L. J.; Dinardo, B.; Jaye, C.; Conrad, B. R.; Ro, H. W.; Germack, D. S.; Fischer, D. A.; DeLongchamp, D. M.; Gundlach, D. J., *Appl. Phys. Lett.* **2010**, *96*.
45. Tedde, S. F.; Kern, J.; Sterzl, T.; Fürst, J.; Lugli, P.; Hayden, O., *Nano. Lett.* **2009**, *9*, 980-983.
46. Hoth, C. N.; Steim, R.; Schilinsky, P.; Choulis, S. A.; Tedde, S. F.; Hayden, O.; Brabec, C. J., *Org. Electron.* **2009**, *10*, 587-593.
47. Mao, J.; Zhang, H.; Jiang, Y.; Pan, Y.; Gao, M.; Xiao, W.; Gao, H. J., *J. Am. Chem. Soc.* **2009**, *131*, 14136-14137.
48. Wei, Y.; Reutt-Robey, J. E., *J. Am. Chem. Soc.* **2011**, *133*, 15232-15235.
49. Hipps, K. W.; Scudiero, L.; Barlow, D. E.; Cooke, M. P., *J. Am. Chem. Soc.* **2002**, *124*, 2126-2127.
50. Calzolari, A.; Jin, W.; Reutt-Robey, J. E.; Buongiorno Nardelli, M., *J. Phys. Chem. C* **2009**, *114*, 1041-1045.

51. Cheng, Z. H.; Gao, L.; Deng, Z. T.; Liu, Q.; Jiang, N.; Lin, X.; He, X. B.; Du, S. X.; Gao, H. J., *J. Phys. Chem. C* **2007**, *111*, 2656-2660.
52. Toader, M.; Hietschold, M., *J. Phys. Chem. C* **2011**, *115*, 12494-12500.
53. Gao, L.; Ji, W.; Hu, Y. B.; Cheng, Z. H.; Deng, Z. T.; Liu, Q.; Jiang, N.; Lin, X.; Guo, W.; Du, S. X.; Hofer, W. A.; Xie, X. C.; Gao, H. J., *Phys. Rev. Lett.* **2007**, *99*, 106402.
54. Buchholz, J. C.; Somorjai, G. A., *J. Chem. Phys.* **1977**, *66*, 573-580.
55. Xiao, X.; Wang, Z.; Hu, Z.; He, T., *J. Phys. Chem. B* **2010**, *114*, 7452-7460.
56. Deng, Z. T.; Guo, H. M.; Guo, W.; Gao, L.; Cheng, Z. H.; Shi, D. X.; Gao, H. J., *J. Phys. Chem. C* **2009**, *113*, 11223-11227.
57. Westwell, M. S.; Searle, M. S.; Wales, D. J.; Williams, D. H., *J. Am. Chem. Soc.* **1995**, *117*, 5013-5015.
58. Guo, S.; Alex Kandel, S., *J. Chem. Phys.* **2008**, *128*.
59. Casado, J.; Pappenfus, T. M.; Miller, L. L.; Mann, K. R.; Ortí, E.; Viruela, P. M.; Pou-Amérigo, R.; Hernández, V.; López Navarrete, J. T., *J. Am. Chem. Soc.* **2003**, *125*, 2524-2534.
60. Jiang, N.; Zhang, Y. Y.; Liu, Q.; Cheng, Z. H.; Deng, Z. T.; Du, S. X.; Gao, H. J.; Beck, M. J.; Pantelides, S. T., *Nano Lett.* **2010**, *10*, 1184-1188.
61. Liu, Q.; Zhang, Y. Y.; Jiang, N.; Zhang, H. G.; Gao, L.; Du, S. X.; Gao, H. J., *Phys. Rev. Lett.* **2010**, *104*, 166101.
62. Lee, M. L.; Fitzgerald, E. A.; Bulsara, M. T.; Currie, M. T.; Lochtefeld, A., *J. Appl. Phys.* **2005**, *97*.
63. Gao, L.; Liu, Q.; Zhang, Y. Y.; Jiang, N.; Zhang, H. G.; Cheng, Z. H.; Qiu, W. F.; Du, S. X.; Liu, Y. Q.; Hofer, W. A.; Gao, H. J., *Phys. Rev. Lett.* **2008**, *101*, 197209.
64. Yoshimoto, S.; Tsutsumi, E.; Suto, K.; Honda, Y.; Itaya, K., *Chem. Phys.* **2005**, *319*, 147-158.
65. Steirer, K. X.; Reese, M. O.; Rupert, B. L.; Kopidakis, N.; Olson, D. C.; Collins, R. T.; Ginley, D. S., *Sol. Energ. Mat. Sol. C* **2009**, *93*, 447-453.
66. Steirer, K. X.; Berry, J. J.; Reese, M. O.; van Hest, M. F. A. M.; Miedaner, A.; Liberatore, M. W.; Collins, R. T.; Ginley, D. S., *Thin Solid Films* **2009**, *517*, 2781-2786.
67. Schilinsky, P.; Waldauf, C.; Brabec, C. J., *Adv. Funct. Mater.* **2006**, *16*, 1669-1672.

68. Hoppe, H.; Sariciftci, N. S., *J. Mater. Chem.* **2006**, *16*, 45-61.
69. Rispens, M. T.; Meetsma, A.; Rittberger, R.; Brabec, C. J.; Sariciftci, N. S.; Hummelen, J. C., *Chem. Commun.* **2003**, 2116-2118.
70. Dabirian, R.; Feng, X.; Ortolani, L.; Liscio, A.; Morandi, V.; Mullen, K.; Samori, P.; Palermo, V., *Phys. Chem. Chem. Phys.* **2010**, *12*, 4473-4480.
71. Écija, D.; Otero, R.; Sánchez, L.; Gallego, J. M.; Wang, Y.; Alcamí, M.; Martín, F.; Martín, N.; Miranda, R., *Angew. Chem. Int. Ed.* **2007**, *46*, 7874-7877.
72. Otero, R.; Écija, D.; Fernández, G.; Gallego, J. M.; Sánchez, L.; Martín, N.; Miranda, R., *Nano Lett.* **2007**, *7*, 2602-2607.
73. Sánchez, L.; Otero, R.; Gallego, J. M.; Miranda, R.; Martín, N., *Chem. Rev.* **2009**, *109*, 2081-2091.
74. Zhang, X.; Yin, F.; Palmer, R. E.; Guo, Q., *Surf. Sci.* **2008**, *602*, 885-892.
75. Guo, S.; Fogarty, D. P.; Nagel, P. M.; Kandel, S. A., *J. Phys. Chem. B* **2004**, *108*, 14074-14081.
76. Altman, E. I.; Colton, R. J., *Surf. Sci.* **1992**, *279*, 49-67.
77. Tskipuri, L.; Shao, Q.; Reutt-Robey, J., *J. Vac. Sci. Technol. A* **2012**, *30*.
78. Delley, B., *J. Chem. Phys.* **1990**, *92*, 508-517.
79. Delley, B., *J. Chem. Phys.* **2000**, *113*, 7756-7764.
80. Perdew, J. P.; Burke, K.; Ernzerhof, M., *Phys. Rev. Lett.* **1996**, *77*, 3865-3868.
81. Perdew, J. P.; Burke, K.; Ernzerhof, M., *Phys. Rev. Lett.* **1997**, *78*, 1396-1396.
82. Perdew, J. P.; Burke, K.; Ernzerhof, M., *Phys. Rev. Lett.* **1998**, *80*, 891-891.
83. Écija, D.; Otero, R.; Sánchez, L.; Gallego, J. M.; Wang, Y.; Alcamí, M.; Martín, F.; Martín, N.; Miranda, R., *Angew. Chem.* **2007**, *119*, 8020-8023.
84. Wang, Y.; Alcamí, M.; Martín, F., *Chem. Phys. Chem.* **2008**, *9*, 1030-1035.
85. Nápoles-Duarte, J. M.; Reyes-Reyes, M.; Ricardo-Chavez, J. L.; Garibay-Alonso, R.; López-Sandoval, R., *Phys. Rev. B* **2008**, *78*, 035425.
86. Günes, S.; Neugebauer, H.; Sariciftci, N. S., *Chem. Rev.* **2007**, *107*, 1324-1338.
87. Brumbach, M.; Placencia, D.; Armstrong, N. R., *J. Phys. Chem. C* **2008**, *112*, 3142-3151.

88. Amb, C. M.; Chen, S.; Graham, K. R.; Subbiah, J.; Small, C. E.; So, F.; Reynolds, J. R., *J. Am. Chem. Soc.* **2011**, *133*, 10062-10065.
89. Tskipuri, L.; Shao, Q.; Reutt-Robey, J., *J. Phys. Chem. C* **2012**, *116*, 21874-21879.
90. Pfuetzner, S.; Mickel, C.; Jankowski, J.; Hein, M.; Meiss, J.; Schuenemann, C.; Elschner, C.; Levin, A. A.; Rellinghaus, B.; Leo, K.; Riede, M., *Org. Electron.* **2011**, *12*, 435-441.
91. Zhang, Y. Y.; Du, S. X.; Gao, H. J., *Phys. Rev. B* **2011**, *84*, 125446.
92. Wang, L.-L.; Cheng, H.-P., *Phys. Rev. B* **2004**, *69*, 165417.
93. Hipps, K. W.; Lu, X.; Wang, X. D.; Mazur, U., *J. Phys. Chem.* **1996**, *100*, 11207-11210.
94. Ediger, M. D.; Angell, C. A.; Nagel, S. R., *J. Phys. Chem.* **1996**, *100*, 13200-13212.
95. Kash, P. W.; Yang, M. X.; Teplyakov, A. V.; Flynn, G. W.; Bent, B. E., *J. Phys. Chem. B* **1997**, *101*, 7908-7918.
96. Altman, E. I.; Colton, R. J., *Surf. Sci.* **1993**, *295*, 13-33.
97. Holman, T.; Ward, M. D., Crystal Engineering with Soft and Topologically Adaptable Molecular Host Frameworks. In *Stimulating Concepts in Chemistry*, Wiley-VCH Verlag GmbH & Co. KGaA: 2005; pp 221-234.
98. Zhang, C.; Chen, H.; Chen, Y.; Wei, Z.; Pu, Z., *Acta. Phys-Chim. Sin.* **2008**, *24*, 1353-1358.
99. Guo, L.; Meng, F. S.; Gong, X. D.; Xiao, H. M.; Chen, K. C.; Tian, H., *Dyes. Pigm.* **2001**, *49*, 83-91.
100. (a) Altman, E. I.; Colton, R. J., *Phys. Rev. B* **1993**, *48*, 18244-18249;  
 (b) Gimzewski, J. K.; Modesti, S.; Schlittler, R. R., *Phys. Rev. Lett.* **1994**, *72*, 1036-1039;  
 (c) Rogero, C.; Pascual, J. I.; Gómez-Herrero, J.; Baró, A. M., *J. Chem. Phys.* **2002**, *116*, 832-836.
101. Janda, P.; Krieg, T.; Dunsch, L., *Adv. Mater.* **1998**, *10*, 1434-1438.
102. (a) Pai, W. W.; Jeng, H. T.; Cheng, C. M.; Lin, C. H.; Xiao, X.; Zhao, A.; Zhang, X.; Xu, G.; Shi, X. Q.; Van Hove, M. A.; Hsue, C. S.; Tsuei, K. D., *Phys. Rev. Lett.* **2010**, *104*, 036103;  
 (b) Gardener, J. A.; Briggs, G. A. D.; Castell, M. R., *Phys. Rev. B* **2009**, *80*, 235434;

- (c) Zhang, X.; He, W.; Zhao, A.; Li, H.; Chen, L.; Pai, W. W.; Hou, J.; Loy, M. M. T.; Yang, J.; Xiao, X., *Phys. Rev. B* **2007**, *75*, 235444;  
 (d) Silien, C.; Pradhan, N. A.; Ho, W.; Thiry, P. A., *Phys. Rev. B* **2004**, *69*, 115434.
103. (a) Chen, T.; Howells, S.; Gallagher, M.; Sarid, D.; Lamb, L. D.; Huffman, D. R.; Workman, R. K., *Phys. Rev. B* **1992**, *45*, 14411-14414;  
 (b) Wragg, J. L.; Chamberlain, J. E.; White, H. W.; Kratschmer, W.; Huffman, D. R., *Nature* **1990**, *348*, 623-624.
104. Gimzewski, J. K.; Modesti, S.; David, T.; Schlittler, R. R., *J. Vac. Sci. Technol. B* **1994**, *12*, 1942-1946.
105. Wang, X. D.; Yurov, V. Y.; Hashizume, T.; Shinohara, H.; Sakurai, T., *Phys. Rev. B* **1994**, *49*, 14746-14749.
106. Hashizume, T.; Motai, K.; Wang, X. D.; Shinohara, H.; Saito, Y.; Maruyama, Y.; Ohno, K.; Kawazoe, Y.; Nishina, Y.; Pickering, H. W.; Kuk, Y.; Sakurai, T., *Phys. Rev. Lett.* **1993**, *71*, 2959-2962.
107. Altman, E. I.; Colton, R. J., *Surf. Sci.* **1993**, *295*, 13-33.
108. Fleming, R. M.; Siegrist, T.; Marsh, P. M.; Hessen, B.; Kortan, A. R.; Murphy, D. W.; Haddon, R. C.; Tycko, R.; Dabbagh, G.; Muijsce, A. M.; Kaplan, M. L.; Zahurak, S. M., *MRS Online Proceedings Library* **1990**, *206*, null-null.
109. (a) Pai, W. W.; Hsu, C.-L.; Lin, M. C.; Lin, K. C.; Tang, T. B., *Phys. Rev. B* **2004**, *69*, 125405;  
 (b) Tang, L.; Xie, Y.; Guo, Q., *J. Chem. Phys.* **2011**, *135*;  
 (c) Schull, G.; Berndt, R., *Phys. Rev. Lett.* **2007**, *99*, 226105.
110. Verheijen, M. A.; Meekes, H.; Meijer, G.; Bennema, P.; de Boer, J. L.; van Smaalen, S.; van Tendeloo, G.; Amelinckx, S.; Muto, S.; van Landuyt, J., *Chem. Phys.* **1992**, *166*, 287-297.
111. Wang, P.; Zhang, H.-J.; Li, Y.-J.; Sheng, C.-Q.; Shen, Y.; Li, H.-Y.; Bao, S.-N.; Li, H.-N., *Phys. Rev. B* **2012**, *85*, 205445.
112. Goldoni, A.; Cepek, C.; Larciprete, R.; Sangaletti, L.; Pagliara, S.; Floreano, L.; Gotter, R.; Verdini, A.; Morgante, A.; Luo, Y.; Nyberg, M., *J. Chem. Phys.* **2002**, *116*, 7685-7690.
113. Maruyama, Y.; Ohno, K.; Kawazoe, Y., *Phys. Rev. B* **1995**, *52*, 2070-2075.
114. Wang, X.-B.; Woo, H.-K.; Huang, X.; Kappes, M. M.; Wang, L.-S., *Phys. Rev. Lett.* **2006**, *96*, 143002.
115. Cheung, D. L.; Troisi, A., *J. Phys. Chem. C* **2010**, *114*, 20479-20488.

116. Zhou, X. L.; Solymosi, F.; Blass, P. M.; Cannon, K. C.; White, J. M., *Surf. Sci.* **1989**, *219*, 294-316.
117. Zhou, X. L.; Blass, P. M.; Koel, B. E.; White, J. M., *Surf. Sci.* **1992**, *271*, 427-451.
118. Alessio, E. A.; Dodero, E.; Pomposiello, C., *J. Chem. Phys.* **1972**, *57*, 4136-4142.
119. Andrews, B.; Anderson, A.; Torrie, B., *Chem. Phys. Lett.* **1984**, *104*, 65-70.
120. G. Jones, R.; A. Clifford, C., *Phys. Chem. Chem. Phys.* **1999**, *1*, 5223-5228.
121. (a) Attard, G. A.; Chibane, K.; Ebert, H. D.; Parsons, R., *Surf. Sci.* **1989**, *224*, 311-326;  
(b) Sparks, S. C.; Szabo, A.; Szulczewski, G. J.; Junker, K.; White, J. M., *J. Phys. Chem. B* **1997**, *101*, 8315-8323.
122. Hill, D. G., *J. Am. Chem. Soc.* **1932**, *54*, 32-40.
123. Zhirong, S.; Ming, G.; Hui, G.; Yongzhen, P. In *Chloroform Dechlorination in Aqueous Solution on Palladium-Nickel/Polymeric Pyrrole Film Modified Titanium Electrode*, Bioinformatics and Biomedical Engineering, 2009. ICBBE 2009. 3rd International Conference on, 11-13 June 2009; 2009; pp 1-4.
124. Danjo, H.; Hirata, K.; Yoshigai, S.; Azumaya, I.; Yamaguchi, K., *J. Am. Chem. Soc.* **2009**, *131*, 1638-1639.
125. Lee, S.; Cho, K.-H.; Lee, C. J.; Kim, G. E.; Na, C. H.; In, Y.; No, K. T., *J. Chem. Inf. Mod.* **2010**, *51*, 105-114.
126. Eisenberg, D.; McLachlan, A. D., *Nature* **1986**, *319*, 199-203.
127. Henderson, M. A.; Mitchell, G. E.; White, J. M., *Surf. Sci. Lett.* **1987**, *184*, L325-L331.
128. Danjo, H.; Hirata, K.; Noda, M.; Uchiyama, S.; Fukui, K.; Kawahata, M.; Azumaya, I.; Yamaguchi, K.; Miyazawa, T., *J. Am. Chem. Soc.* **2010**, *132*, 15556-15558.
129. Tannor, D. J.; Marten, B.; Murphy, R.; Friesner, R. A.; Sitkoff, D.; Nicholls, A.; Honig, B.; Ringnalda, M.; Goddard, W. A., *J. Am. Chem. Soc.* **1994**, *116*, 11875-11882.